The Development and Stability of some Non-Planar Boundary-Layer Flows

Nathaniel David Jewell

Thesis submitted for the degree
of
Doctor of Philosophy
in
Mechanical Engineering
at
The University of Adelaide
(School of Mathematical Sciences)

November 2009

Chapter 1

Introduction

1.1 Introduction to corner flows

The first half of this thesis, comprising Chapters 2–5, examines the laminar and transitional flow parallel to a streamwise corner. Corner flows find numerous engineering applications in the form of wind tunnels, ships, aeroplanes (especially fighter aircraft), tunnels, sluices, and turbomachines. Corner flows are also of considerable theoretical interest, inasmuch as they feature interacting boundary layers. Given the ubiquity of corner flows, it is not surprising that they have been studied for several decades. However, few experimental studies have focussed on laminar and transitional corner-flows. These flows have been the subject of a number of analytical and computational studies; however, this literature is by no means comprehensive or readily accessible to engineers. In particular, only limited data is available for external, oblique or pressure-driven corner flows.

The most important characteristic of a corner flow is its nature. For a prescribed geometry and Reynolds number, will the corresponding corner flow be laminar, transitional or turbulent? Is it possible to exhibit a critical Reynolds number Re_c (or range of Reynolds numbers) below which the laminar flow is stable, and above which the flow is liable to be turbulent or transitional in nature? On this key issue, theoretical analysis is likely to yield valuable data at a fraction of the cost of wind-tunnel experiments. Several such analyses have already been attempted, but much remains to be done. To date, progress on this front has been limited by the high computational cost of solving the eigenvalue equations governing the stability of non-planar laminar flows.

The present work on corner flows will be primarily of a theoretical and computational nature, although we will refer to experimental data wherever appropriate. Our literature review in §1.3 necessarily introduces a significant degree of technical

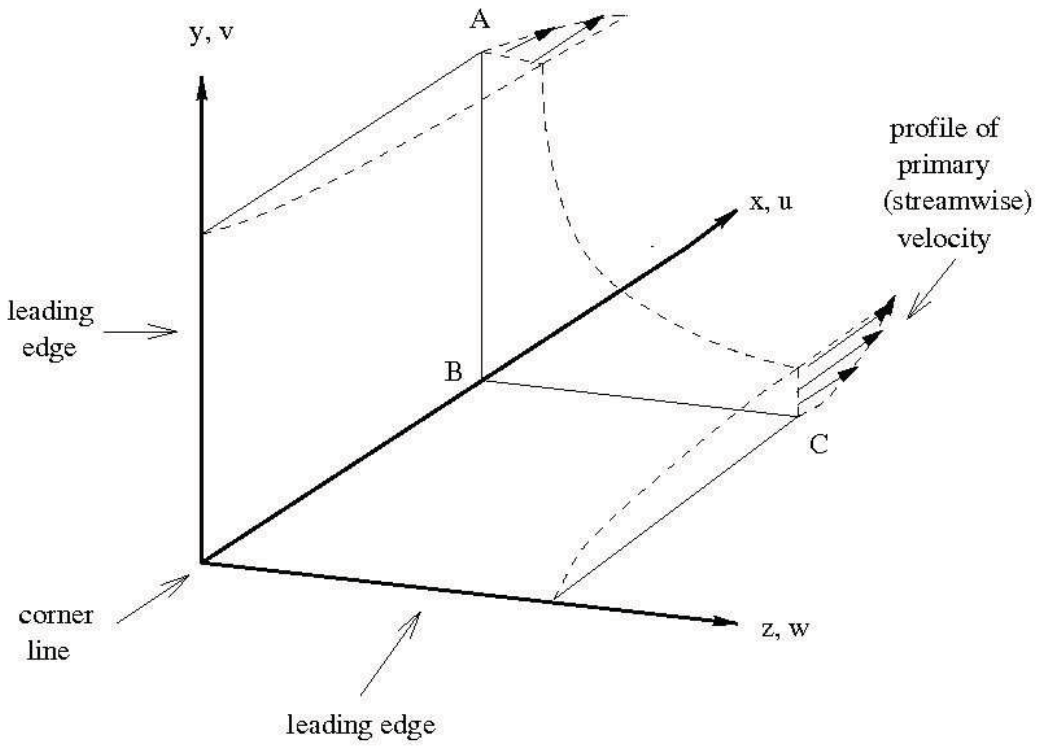

Figure 1.1: Schematic representation of the laminar flow internal to a square corner.

detail and mathematical notation. It is expedient to commence in §1.3.1 with a review of the well-known analytic solution of Blasius (1908) for a flat-plate laminar boundary layer (essentially a trivial corner flow with corner angle $\Phi = \pi$). This leads naturally in §1.3.2 to discussion of the simplest laminar corner flow, illustrated schematically in Figure 1.1; it corresponds to a square corner ($\Phi = \pi/2$) oriented parallel to a incident streamwise flow with zero streamwise pressure gradient (ZPG). Extensions to oblique corners ($0 < \Phi < \pi$) and external corners ($\pi < \Phi < 2\pi$) are briefly outlined in §1.3.4 and §1.3.5 respectively. In §1.3.3 we revisit ZPG square-corner flow with a view to determining its hydrodynamic stability. In §1.3.6 and §1.3.7 we consider the challenging case of laminar corner flows subject to a non-zero streamwise pressure gradient (NZPG). The literature in this field is inconclusive, and provides little numerical data for the important case of a favourable pressure gradient (FPG), believed to be the most stable laminar-flow configuration. Our review of NZPG corner flow begins in §1.3.6 with the (tractable but flawed) power-law model, essentially the three-dimensional analogue of the Falkner–Skan flat-plate boundary layer. We then proceed in §1.3.7 to consider corner-flow models of a more general (and realistic) nature. Finally, we outline our research plan in §1.3.8.

Briefly, the first part of this thesis is structured as follows. Chapter 2 reviews the published data for the simple case of ZPG laminar corner flow, before presenting and discussing our own data set. Chapter 3 analyses the hydrodynamic stability of the corner flow of Chapter 2. Chapter 4 analyses the laminar flow external to a square corner ($\Phi = 3\pi/2$). Finally, Chapter 5 summarizes our findings and offers some recommendations for further research on laminar and transitional corner flows.

1.2 Introduction to unsteady pipe flow

The second part of this thesis, comprising Chapters 6–10, examines the response of laminar pipe flow to a rapid blockage at a downstream location. The key concept is that the fluid comes to rest via a non-trivial process, which may or may not involve a partial transition to a turbulent state.

This study is motivated principally by the well-known water-hammer phenomenon encountered in civil engineering. Traditionally, engineers have been interested primarily in predicting the maximum transient pressures likely to be generated during pipe closure. In most instances this quantity is not difficult to estimate. More recently, engineers have realised the possibility of generating water-hammer events artificially in order to probe pipeline networks (for example, for the presence of leaks). This technique of *Inverse Transient Analysis (ITA)* relies on the standard water-hammer equations but emphasizes the *envelope* and *phase* of the transient pressure wave rather than its maximum amplitude. Unfortunately, these characteristics are not well predicted by standard water-hammer models, owing mainly to reliance on quasi-steady models to estimate the unsteady viscous shear stresses (ie damping friction) induced on the walls of the pipe. This *ad hoc* approach neglects unsteady phenomena and falsely equates zero flow with zero *mean* flow (ie no net flow across a given cross-section of the pipe). The net effect is to underestimate both the damping effect and the phase response in the pressure wave.

Additionally, the study of pipe blockage is motivated by physiology and medicine; more precisely, by unsteady flows in blood vessels and catheters. At first glance, a blocked pipe may appear to represent a poor model of oscillatory blood flow. Yet such a model does provide a valuable first approximation to unsteady flow effects in a blood vessel. The assumption of rapid blockage or impulsive acceleration is a good approximation to the systole (ie acceleration phase of the blood flow), which is at least an order of magnitude shorter than the period of the heartbeat cycle. Furthermore, blood flow is known to encompass laminar, turbulent and transitional regimes (in contrast to engineering applications, where turbulent flows predominate).

The unsteady shear stresses generated within each flow regime, and the onset of turbulence, are both matters of considerable interest to researchers in the field of medicine and physiology, and are discussed further in §1.4.2.

Finally, we are motivated by theoretical considerations. In particular, the study of pipe blockages may advance our collective understanding of unsteady phenomena in fluid flow. As discussed in §1.4.3, we are particularly interested in elucidating the structure and hydrodynamic stability of unsteady boundary layers and corner flows. In this respect, we are well placed to exploit recent advances in fluid mechanics regarding transient behavior of instabilities and efficient computational techniques and algorithms.

At first glance, unsteady pipe flow may appear to have very little in common with the steady streamwise corner flows discussed in the first part of this thesis. The former represents an enclosed flow with cylindrical geometry; the latter occupies a semi-infinite domain bounded on two sides by a planar geometry. Yet these two classes of flows share several commonalities. Each may be variously laminar, transitional, or turbulent. Each occupies a well-defined geometry which is semi-infinite in at least one direction. Each is characterised by two wall boundary layers which intersect to form a corner boundary layer. In the case of corner flow (Figure 1.1), these boundary layers are associated with the horizontal wall ($y = 0$, $z \geq 0$), the vertical wall ($z = 0$, $z \geq 0$), and the corner line ($y = z = 0$, $x \geq 0$). The corresponding pipe-flow boundary layers, illustrated schematically in Figure 9.1, are associated with the pipe wall ($r = 1$), the blockage point within the pipe ($x = 0$, $0 \leq r \leq 1$), and the intersection line $(r, x) = (1, 0)$. This circular intersection region appears quasi-square at small spatial scales ($|x| \ll 1$ and $1 - r \ll 1$) and accordingly induces a corner-like boundary layer throughout the early phase of the laminar-decay process.

Our research plan is detailed in §1.4.4. Briefly, the second part of this thesis is structured as follows. Chapter 6 considers (a) the post-blockage initial conditions and (b) the laminar-decay process well upstream of the blockage ($|x| \gg 1$). Chapter 7 analyses the hydrodynamic stability of the upstream laminar flow using linear eigenmode theory. Chapter 8 broadens the stability analysis of Chapter 7 to encompass linear pseudomodes, while paying especial attention to the transient nature of the laminar flow itself. Chapter 9 analyses the three boundary layers simultaneously and presents a 2D numerical simulation of the decay process, encompassing both the laminar and early-transitional regimes. Chapter 10 summarizes our findings and recommendations regarding unsteady pipe flows.

1.3 Literature survey: Corner flows

1.3.1 Review of 2D Blasius flow

We begin our discussion of corner flows with the trivial case of uniform flow across a straight-edged corner. This is the well-known Blasius boundary layer discussed in numerous texts; see, for example, Schlichting (1968, pp. 125–133) and Munson *et al.* (2002, pp. 548–559). A detailed review of this flow is nevertheless worthwhile, since it will streamline the ensuing discussion of non-trivial corner flows.

The flat plate is semi-infinite, with a well-defined leading edge located at $x = 0$. Incident to the leading edge is a uniform stream of the form

$$\mathbf{u}_\infty \equiv (u, v, w)_\infty = (U^*, 0, 0) \tag{1.1}$$

where U^* is a constant with the dimension of velocity. In 1908, Blasius deduced that the width of this boundary layer is of $O(x/\sqrt{Re_x})$ where Re_x is the local Reynolds number defined by

$$Re_x = \frac{U^* x^*}{\nu}, \tag{1.2}$$

where ν denotes the kinematic viscosity of the fluid and x^* denotes the (dimensional) distance from the leading edge. It is customary to non-dimensionalize the velocity with respect to U^* and the coordinate system with respect to an arbitrary length scale L^* such that $x^*/L^* = O(1)$. We will adopt this convention throughout our study of corner flows; hereafter, we will let $\mathbf{u} = (u, v, w)$ denote non-dimensional velocity and (x, y, z) denote non-dimensional spatial variables. We also define a global Reynolds number Re by

$$Re = \frac{U^* L^*}{\nu} \tag{1.3}$$

such that

$$Re_x = xRe \qquad \text{where} \qquad x = O(1). \tag{1.4}$$

Thus, the flat-plate boundary layer is of non-dimensional width $O(Re^{-\frac{1}{2}})$, and expands in width downstream as $O(\sqrt{x})$. In the above notation, Blasius derived the following expression for the flow:

$$(u, v) = \left(U(\eta), \frac{V(\eta)}{\sqrt{Re_x}}\right) \tag{1.5}$$

where η is a similarity variable defined by

$$\eta = \sqrt{Re_x}\left(\frac{y}{x}\right) \equiv \frac{Re^{\frac{1}{2}} y}{\sqrt{x}} \qquad [\textit{original definition}]. \tag{1.6}$$

The shape functions U and V are related to each other by

$$U \,=\, f', \qquad V \,=\, \tfrac{1}{2}(\eta f' - f), \tag{1.7}$$

where f is the solution to the third-order nonlinear ordinary differential equation

$$f''' \,+\, \tfrac{1}{2} f f'' \,=\, 0, \tag{1.8}$$

subject to the boundary conditions

$$f(0) = 0, \quad f'(0) = 0, \quad \text{and} \quad \lim_{\eta\to\infty} f'(\eta) = 1, \tag{1.9}$$

corresponding respectively to

$$V(0) = 0, \quad U(0) = 0 \quad \text{and} \quad \lim_{\eta\to\infty} U(\eta) = 1. \tag{1.10}$$

Nowadays, in the interests of analytic convenience, it is customary to rescale η by a factor of $\sqrt{2}$, ie

$$\eta \,=\, \frac{Re^{\frac{1}{2}} y}{\sqrt{2x}} \,\equiv\, \left(\tfrac{1}{2} Re_x\right)^{\frac{1}{2}} \left(\frac{y}{x}\right) \qquad\qquad [\textit{standard definition}], \tag{1.11}$$

and to rescale the Blasius solution accordingly:

$$(u, v) \,=\, \left(U(\eta),\, Re^{-\frac{1}{2}} \frac{V(\eta)}{\sqrt{2x}}\right), \tag{1.12a}$$

$$(U, V) \,=\, (f',\, \eta f' - f)\,, \tag{1.12b}$$

$$f''' + f f'' \,=\, 0. \tag{1.12c}$$

The Blasius boundary layer possesses a well-defined structure and width. Its non-dimensional *displacement width* $\delta_1 \equiv \delta_1(x)$ is given by

$$\delta_1(x) \,=\, \lim_{y\to\infty} \int_0^y (1 - U(x, y'))\, \mathrm{d}y' \tag{1.13a}$$

$$\,=\, \sqrt{2x/Re} \int_0^\infty (1 - U(\eta))\, \mathrm{d}\eta \tag{1.13b}$$

$$\,=\, (1.72\sqrt{x})\, Re^{-\frac{1}{2}}. \tag{1.13c}$$

The *full width* δ_2 of the boundary layer, defined by

$$u(x,\, \delta_2(x)) \,=\, 0.99\, U^*, \tag{1.14}$$

is given by

$$\delta_2(x) \,=\, \left(5.0\,\sqrt{x}\right) Re^{-\frac{1}{2}} \,\equiv\, \frac{5.0\, x}{\sqrt{Re_x}} \tag{1.15a}$$

$$\,=\, 2.9\; \delta_1(x). \tag{1.15b}$$

The integral in (1.13b) defines the *Blasius constant*:

$$\beta \equiv \int_0^\infty [1 - (\eta f'(y) - f(\eta))]\,\mathrm{d}\eta = 1.21678. \tag{1.16}$$

The (dimensional) wall shear stress τ scales as

$$\tau = O\left(x^{-\frac{1}{2}}\,(U^*)^{\frac{3}{2}}\right) \equiv O\left(Re^{\frac{3}{2}}\right). \tag{1.17}$$

In engineering parlance, the *friction factor* for steady laminar pipe flow scales as

$$C_f = O(Re^{-\frac{1}{2}}). \tag{1.18}$$

1.3.2 The simplest corner flow

The simplest non-trivial corner flow is illustrated schematically in Figure 1.1. The fluid flow is steady, laminar and Newtonian in character. The corner itself comprises two quarter-infinite planes oriented at right angles to each other. In accordance with convention, we identify these planes as a *horizontal wall* and *vertical wall* located respectively at $y = 0$ and $z = 0$. Similarly, we identify the *leading edge* with $x = 0$ and the *corner line* with $(y, z) = (0, 0)$, so that the *corner region* consists precisely of the positive octant of the (x, y, z) coordinate system. Incident to the leading edge is a unidirectional steady laminar flow of the form $\mathbf{u} = (U^*, 0, 0)$ for $x \leq 0$. To first order, this flow extends unchanged into the corner region ($x > 0$), except for a boundary layer in the immediate vicinity of the walls.

This ZPG corner-flow configuration is well documented in the literature. Yet it is highly non-trivial, owing to the nonlinear interaction between the boundary layers associated with the two walls. This flow is also quite difficult to reproduce accurately in a laboratory.

The first theoretical model of laminar corner flow was that of Carrier (1947). Inspired by the work of Blasius (1908) for 2D flat-plate flow, Carrier modelled the flow as a superposition of two Blasius boundary layers characterized by the similarity variables η and ζ respectively. His solution thus assumed the analytic form

$$(\eta, \zeta) = \left(\frac{Re}{2x}\right)^{\frac{1}{2}} (y, z), \tag{1.19a}$$

$$F = f(\eta)f(\zeta) + \widetilde{F}(\eta, \zeta), \tag{1.19b}$$

$$u = U(\eta, \zeta), \tag{1.19c}$$

$$(v, w) = \left(\frac{1}{2Re_x}\right)^{\frac{1}{2}} (V(\eta, \zeta),\, W(\eta, \zeta))\,, \tag{1.19d}$$

$$(U, V, W) = (F_{\eta\zeta},\, \eta U - F_\zeta,\, \zeta U - F_\eta)\,, \tag{1.19e}$$

where $\widetilde{F}$ is a localised function representing the interaction between the boundary layers associated with the two walls. After substituting (1.19) into the Navier–Stokes equations, Carrier solved $\widetilde{F}$ numerically over a coarse grid (without the aid of a computer!). He believed that his numerical values for U were accurate to three figures. At best, Carrier's solution is only an approximation, since it attempts to represent a three-dimensional flow via a single streamfunction. This weakness was noted by other researchers, but no serious alternative was proposed during the 1950s (a period which coincided with the infancy of electronic computing).

Stewartson (1961) presented a rigorous analysis of the steady laminar flow over a *quarter*-infinite plate. His analysis highlighted the phenomenon of boundary-layer interaction, and permitted the numerical evaluation of some of the leading-order terms in the asymptotic expansion.

Rubin (1966) attempted a rigorous analysis of corner flow using the method of matched asymptotic expansions. Although Rubin did not attempt a full numerical solution, he was able to identify a non-trivial crossflow within the wall boundary layer adjacent to the corner region proper. He showed that this crossflow does not decay to zero with increasing distance from the corner line (as assumed by Carrier); rather, the corner-flow profile asymptotes to the 2D Blasius profile of §1.3.1 plus a superimposed crossflow. The latter takes the following algebraic form within the horizontal boundary layer:

$$w \;=\; \frac{Re^{-\frac{1}{2}}}{\sqrt{2x}}\left(W_0(\eta) \;+\; \widetilde{W}(\eta,\zeta)\right) \qquad \text{for} \qquad \eta = O(1), \quad \zeta \gg 1, \tag{1.20}$$

where, by definition,

$$\widetilde{W}(\eta,\zeta) \to 0 \qquad \text{as} \qquad \zeta \to \infty.$$

This crossflow is induced by the secondary outflow velocity emanating from the vertical boundary layer ($\eta \gg 1$, $\zeta = O(1)$).

A few years later, Rubin attempted a full numerical solution to the corner-flow problem. When his first attempt failed (numerical convergence proving elusive), he reworked the theoretical analysis and discovered another major flaw in Carrier's analysis. It turns out that the flow varies algebraically (rather than exponentially) as a function of distance from the corner line. In particular, the streamwise flow within the horizontal boundary layer takes the asymptotic form

$$u \;\equiv\; U(\eta,\zeta) \;=\; U_0(\eta) \;+\; U_2(\eta)\,\zeta^{-2} \qquad \text{for} \qquad \eta = O(1), \quad \zeta \gg 1, \tag{1.21}$$

where U_0 is precisely the Blasius profile $f'(\eta)$. On substitution of this result into the continuity equation, one finds that the crossflow component $\widetilde{W}$ in (1.20) decays at the very slow rate of $O(\zeta^{-1})$. A rigorous treatment of asymptotic properties

appears in Pal and Rubin (1971); the leading-order results of this analysis, and a full numerical solution resulting therefrom, are detailed in Rubin and Grossman (1971). The authors demonstrate that the laminar corner boundary layer is highly non-trivial; it comprises an inner corner layer characterised by strongly nonlinear boundary-layer interaction, coupled with an outer layer described by the asymptotic properties (1.20) and (1.21). Thus, the full corner boundary layer is several-fold wider than the corresponding 2D Blasius boundary layer. The inner corner layer, meanwhile, is approximately 25% broader than that predicted by Carrier (see, for example, Figures 4 and 5 of the Rubin and Grossman (1971) paper), and is notable for the strongly inflectional profile of the streamwise velocity as viewed along the corner bisector. This latter feature has led numerous authors to speculate that the laminar corner boundary layer is less stable than its 2D Blasius counterpart. We will revisit the stability issue shortly.

Despite the seminal nature of Rubin and Grossman (1971), it does suffer from several drawbacks. Firstly, the spatial resolution of their numerical scheme is quite low, owing to the dual restrictions of numerical stability and available computing power; consequently, it is unclear from their results whether the inner corner region contains a vortex. Secondly, numerical implementation of the authors' asymptotic analysis is somewhat cumbersome. Finally, the asymptotic analysis throws up a crucial numerical constant for which there is no known closed-form formula or governing equation; instead, it must be estimated by an *ad hoc* iterative procedure.

Since 1971, the laminar corner flow has been re-computed using various numerical methods by Ghia (1975), Balachandar and Malik (1995), Dhanak and Duck (1997), Parker and Balachandar (1999), and Galionis and Hall (2005). To varying degrees, each of the above authors attempted to simplify the analysis of Rubin and Grossman (1971). In Chapter 2 we will conduct a detailed review of their respective numerical schemes, prior to generating our own data set for this laminar corner flow.

The seminal work of Rubin and Grossman (1971) stimulated several attempts to generate a laminar corner flow within a wind tunnel. A review of these experiments appears in Zamir (1981), together with some previously unpublished experimental data from Zamir and Young (1979). Zamir (1981) concluded that agreement between theory and experiment was poor in general. However, he argued that this failure was not attributable to experimental imperfection (e.g. misalignment of the incident flow with the leading edge), nor to poor instrumental resolution of the boundary layer (whose thickness was typically of the order of one centimetre). Rather, Zamir argued that the laminar corner flow is stable only at low Reynolds numbers and/or under favourable pressure gradients. Indeed, he noted that stable laminar flows had been observed only in instances where experimental error induced a weakly-

favourable streamwise pressure gradient; conversely, a negligible pressure gradient was invariably associated with transitional or turbulent flow. Furthermore, Zamir showed that the observed laminar boundary-layer profiles provided a better match with the predictions of Rubin and Grossman (1971) and Ghia (1975) than those of Carrier (1947). Finally, by extrapolating the experimental data on the basis of streamwise pressure gradient, Zamir hypothesized a critical Reynolds number of $Re_c = O(10^4)$ for a genuinely pressure-free (ZPG) laminar corner flow. This conclusion, however tentative, is quite striking; it is an order of magnitude lower than the theoretical stability limit $Re_c \approx 9 \times 10^4$ for 2D Blasius flow. Indeed, the latter figure is itself a very conservative estimate[1]. The experimental onset of instability in Blasius flow usually occurs at a streamwise location x corresponding to a Reynolds number in the range $2 \times 10^5 \lesssim Re_x \lesssim 3 \times 10^6$; a critical value of $Re_c = 5 \times 10^5$ is typically used as a rule of thumb in the engineering community (Munson *et al.* 2002, p. 559).

1.3.3 The stability of laminar ZPG corner flows

The review of experimental data by Zamir (1981) suggests that ZPG laminar corner flow is substantially less stable than its 2D counterpart. It also suggests that corner flows are sensitive to environmental conditions, and in particular, that the laminar flow is rapidly stabilized by a favourable pressure gradient. Zamir's work has inspired several attempts to cross-check the above empirical findings against theoretical and computational data. This section, therefore, reviews the theoretical literature regarding the stability of ZPG laminar corner flow. Some of this literature also considers the case of a pressure-driven corner flow; however, we defer discussion of this case to §§1.3.6 and 1.3.7.

Lakin and Hussaini (1984) presented the first rigorous theoretical analysis of the stability of laminar corner flow. Their analysis is based on the classical stability theory of linear eigenmode analysis. The essential idea is to 'seed' the laminar flow with an infinitesimal wavelike perturbation of the form

$$\epsilon\widetilde{\mathbf{u}} \equiv \epsilon\mathbf{U}\,\mathrm{e}^{\mathrm{i}\alpha R(x-ct)} \tag{1.22}$$

where $R = O(Re^{\frac{1}{2}})$ is a boundary-layer scaling, $0 < \epsilon \ll 1$ is an infinitesimally small constant, α is a real-valued streamwise wavenumber, and $c \equiv c_\mathrm{r} + \mathrm{i}c_\mathrm{i}$ is a complex-

[1] Good qualitative agreement with experiment is observed if the instability is induced artificially within the frequency range predicted by eigenmode stability theory; see, for example, Schlichting (1968) and Smith (1979). Smith (1979) achieved a further reduction in the discrepancy by accounting for non-parallel effects, ie the slow streamwise development of the Blasius boundary layer.

valued wave-speed. The complex amplitude $\widetilde{\mathbf{U}}$ is approximated by the streamwise-similar form $\widetilde{\mathbf{U}}(\eta,\zeta)$ under the *parallel-flow approximation* that the local boundary-layer scaling Re_x is essentially constant over the streamwise scale $\Delta x = 2\pi/(\alpha R)$ of the instability (compare with the Blasius-layer formulae (1.13) and (1.15)). On substituting into the governing equations and retaining only the $O(\epsilon)$ terms, one obtains a set of linear partial differential equations in $\mathbf{U}$. For each parameter value (Re,α), these governing equations yield a spectrum of eigenmodes $\{\,(\mathbf{U}_j, c_j)\,\}$. The leading eigenmode thus defines the critical Reynolds number Re_c and critical wavenumber α_c of the laminar flow:

$$\Im[c_1] \le 0 \quad \text{for all} \quad Re \le Re_c \quad \text{with equality iff} \quad (Re,\alpha) = (Re_c,\alpha_c). \tag{1.23}$$

Despite the rigour of their analysis, Lakin and Hussaini (1984) make no attempt at numerical solution of the eigenmode equations, and thus are unable to present any useful conclusions. Some numerical progress was subsequently made by Dhanak (1993) and Dhanak and Duck (1997), who parametrized the spanwise coordinate $\zeta = O(10)$ and proceeded to derive a system of parabolised stability equations (PSE) in the vertical coordinate η. This *ad hoc* analysis is inherently biased towards viscous-type instabilities (analogous to those encountered in 2D Blasius flow at $Re \gtrsim 10^5$), and is ill-suited to probing the inner corner region. Dhanak and Duck (1997) reported a stability limit of $Re_c = 31K$ or $Re_c = 56K$, depending on whether ζ was set to 10 or 20 respectively.

Balachandar and Malik (1995) presented a two-part stability analysis. In the first part of their paper, the stability equations are discretized exclusively along the corner bisector $\eta = \zeta$ to produce a quasi-1D system of equations (in effect, the inverse of the Dhanak and Duck (1997) analysis). This *ad hoc* analysis yielded $Re_c = 435$, ie two orders of magnitude (!) lower than for 2D Blasius flow. The second half of their paper presents a genuinely 2D model of corner stability, albeit restricted to instabilities of inviscid type in the asymptotic limit $Re \to \infty$. Under the *inviscid approximation* the governing equations reduce to a single eigenvalue equation, the 2D Rayleigh equation. The authors reported two modes of instability (one much more vigorous than the other), both centred on the corner bisector and most active in the inner corner region. These findings lend qualitative support to the conjecture that ZPG laminar flow is inviscidly unstable, even though they do not provide any estimate of Re_c.

Parker and Balachandar (1999) relaxed the inviscid approximation of Balachandar and Malik (1995), thereby presenting the first fully-2D stability analysis of laminar corner flow. They found a wide spectrum of viscous-type eigenmodes active within the outer corner region at $Re \gtrsim 10^5$, and showed that the least-stable modes

are those which propagate obliquely towards the corner line (rather than parallel to it, as suggested by (1.22)). The authors also reported that the inviscid mode is unique up to wavenumber α, finding no evidence of the secondary inviscid mode reported by Balachandar and Malik (1995). Even more surprisingly, they find the inviscid mode to be active only from $Re_c \approx 500K$, ie nearly one order of magnitude above that of the viscous modes.

Recently, Galionis and Hall (2005) questioned the results of Parker and Balachandar (1999) on the grounds that their numerical method (a) relies on a questionable vectorized eigensolver and (b) does not impose any wall-boundary conditions on the perturbation pressure. Instead, Galionis and Hall (2005) attempt the first quasi-3D stability analysis of laminar corner flow. They relax the parallel-flow approximation by combining pseudospectral discretization in the transverse (η, ζ) domain with a finite-difference marching scheme in the streamwise x coordinate. Somewhat strangely, however, the authors follow Parker and Balachandar (1999) in omitting wall-boundary conditions on the pressure, instead relying on a staggered collocation grid for accurate representation of the perturbation pressure. They concur with Parker and Balachandar (1999) in reporting that the leading instabilities are viscous in nature ($Re_c = 73K$). They also report that the (unique) inviscid mode becomes active at an unspecified Reynolds number in the range $100K < Re_c < 150K$.

1.3.4 Oblique corner flows

The published literature contains only a limited body of results for non-square corner configurations. Wilkinson and Zamir (1984) derive a convenient set of governing equations valid for an arbitrary internal corner ($0 < \Phi < \pi$); however, their treatment of the crucial asymptotic boundary conditions is non-rigorous. They present schematic results for the cases of corner angles of 30, 60, 90, 120 and 150 degrees, but do not present any systematic numerical data.

Duck, Stow and Dhanak (1999) improved upon the boundary conditions of Wilkinson and Zamir (1984) and presented some accurate numerical results for the case of a 45-degree corner ($\Phi = \frac{\pi}{4}$). Their analysis is applicable in principle to any internal corner ($0 < \Phi < \pi$); however, the authors do not attempt a systematic numerical survey of oblique corners, preferring instead to focus on questions of a more fundamental nature. We will revisit their work in §1.3.7.

Ridha (2003) analysed the laminar flow within a streamwise corner with wedge-shaped walls. This complex and fascinating flow is of considerable relevance to engineering. We will not discuss it in any depth, however, since it differs qualitatively from the streamwise corner flows considered in the present work.

1.3.5 External corner flows

External corners, characterised by an opening angle Φ in the range $\pi < \Phi < 2\pi$, occur as *chines* in the hulls of water craft and in the bodies of military aircraft. The viscous drag associated with chine flow contributes significantly to the overall drag on the craft, especially in the case of turbulent flows. On the other hand, chines can improve the seagoing characteristics of small ships (see, for example, Shi–Min and Yun–Cai (1981), Zborowski and Chu (1992) and Breslin (2001)). The performance of aircraft is enhanced by transition to turbulence in mid-wing: the resultant delay in flow separation from the wing increases the stall angle. Recently, chine flow has been suggested as a stabilizer for fighter aircraft at high angles of attack. Although this remains speculative, several small-scale experiments have been performed in wind tunnels, e.g. Arena *et al.* (1995), Gangulee and Ng (1995), and Ravi and Mason (1994).

Perhaps surprisingly, there is only a limited body of literature on external corner flows. We are not aware of any theoretical studies of laminar flow external to a corner, except that of Ridha (2003) for the case of a streamwise corner with wedge-shaped walls. Our own interest in external corner flows was originally stimulated by the wind-tunnel experiments of Moinuddin *et al.* (2001), who obtained accurate measurements of steady turbulent ZPG flow parallel to an external square corner. They reported a pronounced 'bulging' of the boundary layer in the immediate vicinity of the corner line. The flow also exhibited a noticeable degree of asymmetry; it was unclear whether this feature was genuine or merely the result of experimental misalignment.

Recently, this conundrum was partially resolved by Moinuddin, Joubert and Chong (2004), who reported a higher degree of spatial symmetry in the flow. They also confirmed earlier results on the qualitative structure of the boundary layer and revealed the existence of a pair of counter-rotating vortices near the corner line. In this study, the authors were able to measure all components of the mean flow $(\bar{u}, \bar{v}, \bar{w})$ and most components of the time-averaged Reynolds stresses, such as $\overline{(u')^2}$ and $\overline{u'v'}$. This data strongly suggested that the observed boundary-layer 'bulge' results from the Reynolds stresses, and thus represents a strictly turbulent phenomenon. This hypothesis is consistent with the observation that the corner-line vortices are large enough to dominate the corner region, whereas the viscosity-dominated 'friction' boundary layer on the wall itself is of sub-millimetre thickness.

1.3.6 Falkner–Skan corner flows

We now consider the case of laminar flow in a square corner under the influence of a non-zero streamwise pressure gradient (NZPG). Our *modus operandi* is to prescribe the external streamwise velocity profile $U_\infty(x)$ and the corresponding leading-order pressure term $P_\infty(x)$, non-dimensionalised with respect to a characteristic velocity U^* and characteristic pressure $P^* = \rho(U^*)^2$. Note that U_∞ and P_∞ are not independent, being related via

$$P'_\infty = -U_\infty U'_\infty \tag{1.24}$$

where the primes denote differentiation with respect to x. It follows that a favourable or adverse pressure gradient corresponds to $P_x < 0$ or $P_x > 0$ respectively. The introduction of a streamwise pressure gradient also produces a qualitative change in the secondary flow (v, w). Recall that in the ZPG case, v and w are of order $O(Re^{-\frac{1}{2}})$, which typically equates to two orders of magnitude smaller than the primary flow. In the NZPG case, however, the secondary flow must grow in magnitude with increasing distance from the corner line. This is an immediate consequence of the continuity equation in the external region:

$$U'_\infty + v_y + w_z = 0. \tag{1.25}$$

It will nevertheless prove convenient to retain (with minor modifications) the original definitions of the similarity variables (η, ζ) and scaled shape functions (V, W), on the understanding that V and W are no longer restricted to $O(1)$ values.

Ridha (1992) and Dhanak and Duck (1997) independently considered a Falkner–Skan type corner-flow model of the form

$$U_\infty = x^n, \qquad P_\infty = -\tfrac{1}{2}x^{2n}, \qquad n \text{ constant}. \tag{1.26}$$

In this model, favourable, adverse and neutral pressure gradients correspond respectively to positive, negative and zero values of the parameter n. The authors conjecture that the boundary layer develops in a streamwise similar fashion, its local width being of order $O(\sqrt{x^{1-n}})$. The advantages of the Falkner–Skan model are its tractability and its inclusion of ZPG flow as a special case. Its obvious disadvantage is its failure to be smooth and continuous across the leading edge $x = 0$. Indeed, in the case $n < 0$ the streamwise flow becomes unbounded in the limit $x \to 0^+$; conversely, for $n > 1$ the conjectured boundary-layer width approaches infinity in the vicinity of the leading edge. Ridha (1992) is rigorous but narrow in scope, being largely confined to the leading-order streamwise flow $U_0(x, \eta)$ in the asymptotic far-field limit ($\zeta \to \infty$). Dhanak and Duck (1997) presents an explicit model for

the full NZPG corner boundary layer, re-defining the boundary-layer variables (η, ζ) and shape functions (U, V, W) as follows:

$$(\eta, \zeta) \;=\; \left(\frac{x^n Re}{2x}\right)^{\frac{1}{2}} (y, z), \tag{1.27a}$$

$$u \;=\; x^n U(\eta, \zeta), \tag{1.27b}$$

$$(v, w) \;=\; \left(\frac{x^n}{2Re_x}\right)^{\frac{1}{2}} \left(V(\eta, \zeta),\, W(\eta, \zeta)\right). \tag{1.27c}$$

Within the horizontal boundary layer (ie for $\eta = O(1)$, $\zeta \gg 1$), the flow takes the asymptotic far-field form

$$U \;=\; U_0(\eta) \;+\; O(\zeta^{-2}), \tag{1.28a}$$

$$V \;=\; V_0(\eta) \;+\; O(\zeta^{-2}), \tag{1.28b}$$

$$W \;=\; \zeta W_{-1}(\eta) \;+\; W_0(\eta) \;+\; O(\zeta^{-1}). \tag{1.28c}$$

Dhanak and Duck (1997) plotted the flow pattern in the transverse (η, ζ) plane for the cases $n = 0$ and $n = 0.5$ (Figures 6 and 9 of their paper respectively). Figure 2 of their paper plots the asymptotic shear stresses

$$\tau_0(n) \;=\; U_0'(0; n) \qquad \text{and} \qquad \sigma_0(n) \;=\; W_{-1}'(0; n)$$

(where the primes denote differentiation with respect to η), while Figure 3 plots the crossflow function $W_{-1}(\eta)$ for the cases of $n = 0.5$ and $n = 1$.

Both Ridha (1992) and Dhanak and Duck (1997) discovered that the leading-order boundary layer equations describing the flow far from the corner line admit two qualitatively different solutions[2] for all n satisfying $-0.018 \lesssim n \lesssim 1.276$. The differences are most evident in the ZPG case ($n = 0$), for which one solution corresponds to the Blasius-type corner flow of §1.3.2 with W_{-1} identically zero; the alternative solution corresponds to an unbounded jet-like crossflow $W_{-1} \neq 0$ within the boundary layer (see Figures 3 and 7 of Dhanak and Duck (1997)). Significant qualitative differences are also evident for $n \neq 0$ (Figures 2, 3 and 8 of their paper). It would be tempting to dismiss the non-Blasius alternative solution[3] as physically unrealistic,

[2] In addition, Dhanak and Duck (1997) reported some minor solution branches, some of them corresponding to strongly negative values of n. Whether these are of practical significance remains unclear.

[3] Unfortunately, the literature is inconsistent in its terminology regarding the Blasius and non-Blasius solutions. Ridha (1992) refers to them as *lower-branch* and *upper-branch* solutions respectively, on the basis that the non-Blasius solution exhibits uniformly higher values of asymptotic wall shear stress τ_0. In contrast, Dhanak and Duck (1997) examine the properties of a vorticity function θ (Figure 2c of their paper), and accordingly describe the non-Blasius flows as lower-branch solutions.

a numerical artefact of the boundary-layer approximations. On the other hand, the non-Blasius laminar boundary layer is somewhat thinner, and may therefore be the more stable one (since it has a lower boundary-layer Reynolds number Re_δ than the corresponding Blasius-type layer with the same streamwise Reynolds number Re). Indeed, Ridha (1992) argues that the non-Blasius configuration is more likely to be observed experimentally:

> We recall that in experimental works 'venturing' to obtain a stable laminar [ZPG corner flow], the wall shear stress in [the blending boundary layer] overshoots markedly the Blasius value (before tending asymptotically to it further away from the corner line).

This key question is at present still unresolved, although further evidence on this issue will be presented in §1.3.7.

Dhanak and Duck (1997) also present a stability analysis of the Falkner–Skan corner flow, using the parabolised stability equations (PSE) discussed in §1.3.3. Since this analysis is approximate at best, its results must be treated with caution. These results do, however, support the conjectures that (a) the laminar flow is stabilized by a favourable pressure gradient, and conversely, destabilized by an unfavourable gradient; and (b) the non-Blasius configuration is the more stable one. The critical Reynolds number $Re_c(n)$ is found to vary only marginally between $n = 0$ and $n = 0.15$, yet it differs by up to three orders of magnitude between $n = 0.15$ and $n = 0.25$.

Parker and Balachandar (1999) studied the power-law model of Ridha (1992) and Dhanak and Duck (1997) for a neutral or unfavourable pressure gradient ($-0.018 \lesssim n \leq 0$). The authors considered both Blasius and non-Blasius configurations, but chose to limit their stability analysis to Blasius-type flows. Their stability results for the case of ZPG Blasius-type flow ($n = 0$) were discussed at some length in §1.3.3. For the NZPG case ($n < 0$), the authors found the inviscid mode to be dominant; the corresponding critical Reynolds number attained a minimum of $Re_c = 6.0 \times 10^4$ at the minimum value $n \approx -0.018$ for which the power-law model yields reliable solutions.

The work of Galionis and Hall (2005) was discussed in §1.3.3 for the ZPG case. Their NZPG results, like those of Parker and Balachandar (1999), are limited to the case of a power-law flow with unfavourable pressure gradient ($-0.018 \lesssim n < 0$). They confirmed the finding of Parker and Balachandar (1999) that, relative to the viscous modes, the inviscid mode is much more sensitive to the streamwise pressure gradient. They also confirmed the conjecture that the non-Blasius laminar-flow configuration is more stable than its Blasius-type counterpart. The authors present a

suite of numerical data on instability growth rates, but do not offer explicit estimates of Re_c for $n \neq 0$.

1.3.7 General pressure-driven corner flows

Most flows encountered in practice are turbulent rather than laminar. The most stable laminar corner flows are those driven by a favourable pressure gradient (FPG), in contrast to the $n < 0$ Falkner–Skan flows considered in §1.3.6. Unfortunately, only limited amount of data is available on FPG corner flows. Most of this data is based on the Falkner–Skan model ($n > 0$), which is problematic in the sense that the external flow $U_\infty(x)$ fails to be uniformly smooth and continuous. To the best of our knowledge, the only globally-smooth FPG model is that of Duck *et al.* (1999):

$$U_\infty(x) \;=\; 2 - \mathrm{e}^{-\sqrt{x}}, \qquad x \geq 0. \tag{1.29}$$

The authors treat this as a special case of the following more general (non-smooth) model:

$$U_\infty(x) \;=\; x^n(2 - \mathrm{e}^{-\xi}) \qquad \text{where} \qquad \xi = x^{(1-n)/2}, \qquad n \,\text{constant}. \tag{1.30}$$

The introduction of an arbitrary pressure gradient weakens the property of streamwise similarity. The governing equations are fully three-dimensional (even when expressed in terms of the similarity variables (1.27)) and exceptionally difficult to solve, but would appear to be amenable to a streamwise marching algorithm. To this end, Duck *et al.* (1999) began by formulating the governing equations for the asymptotic far-field solution; these equations were discretized using a second-order finite-difference scheme in (ξ, η) space and solved using a marching algorithm commencing from the leading edge $\xi = 0$. The resulting numerical data then furnishes boundary conditions for a full numerical solution in (ξ, η, ζ) space. This algorithm was repeated twice for each value of n, corresponding respectively to Blasius-type and non-Blasius solutions. Satisfactory results were obtained for a non-Blasius pressure-driven flow with $n = 0.35$. However, the marching algorithm was less successful for $n = 0$, and failed altogether for a Blasius-type flow with $n = 0.35$ (see Figures 3a and 6 of their paper respectively). This disappointing experience alerted Duck *et al.* (1999) to the existence of an 'algebraic' streamwise eigenstate of the form

$$\widetilde{\mathbf{U}} \;=\; \xi^\lambda \hat{\mathbf{U}}(\eta, \zeta) \qquad \text{where } \lambda \text{ is a complex constant.} \tag{1.31}$$

Although this eigenstate is unstable only Blasius-type flows, it actually occurs in both Blasius and non-Blasius flows for all $n \gtrsim -0.018$ (see Figure 4 of their paper, which shows both λ_r branches approaching zero as $n \to -0.018$; the labels *Upper*

branch and *Lower branch* herein denote Blasius and non-Blasius flows respectively). In consequence, the marching algorithm is infeasible for weakly FPG flows ($0 < n \lesssim 0.1$) in both the Blasius and non-Blasius regimes.

The question then arises of whether it is possible to compute realistic FPG corner flows. It may be possible in principle to stabilize the marching algorithm, albeit at a high computational price. In the case of the asymptotic far-field component $\mathbf{U}(\xi, \eta; \zeta)$ (which furnishes the vital boundary conditions), the authors found it necessary to discard the marching algorithm and treat the problem as fully elliptic in (ξ, η) space, discretizing and solving for all flow variables simultaneously; the numerical results are plotted for $n = 0.35$ in Figure 7 of their paper. A key question then arises regarding the full 3D flow: Must it be treated as fully elliptic in (ξ, η, ζ) space, or will the accurate asymptotic solution suffice to suppress the instability at a global level? If the former holds, it follows that the full problem is extremely challenging even for a supercomputer; if the latter, then the original 3D marching algorithm should be viable. Duck *et al.* (1999) believed the former was true.

Duck and Owen (2004) shed further light on these streamwise eigenstates. Instead of attempting to suppress these instabilities, the authors derived governing equations for them. Their analysis encompassed several classes of laminar corner flows; in the interests of brevity, however, we will consider only the power-law model of Dhanak and Duck (1997). (Since this flow is by definition streamwise-similar, it is a relatively simple matter to isolate the instabilities.) The authors consider three categories of streamwise instabilities: infinitesimal (ie linear), finite (weakly nonlinear), and unsteady infinitesimal (linear time-periodic). We now discuss each of these in turn.

Unsteady instabilities were found to exhibit some growth over a streamwise scale of $\Delta x = O(1)$. Further downstream, however, they invariably decayed in magnitude. We will not discuss these results in greater depth.

Infinitesimal instabilities, of the form (1.31) with $\lambda_r > 0$, were found to occur in all power-law basic flows of Blasius type ($n > -0.018$). Crucially, they were absent from the corresponding non-Blasius basic flows. These instabilities were invariably of a strongly-3D character, such that $\widetilde{U}_0 \neq 0$ and $\widetilde{W}_{-1} \neq 0$ even in the ZPG case $n = 0$. Figures 2 and 3 of Duck and Owen (2004) show the wall-stress pattern $(\widetilde{\tau}_0, \widetilde{\sigma}_0)$ induced by the instability in Blasius ZPG flow ($n = 0$). Though novel, these findings are in full qualitative agreement with those of Duck *et al.* (1999) for non-similar basic flows.

Finally, we consider a weakly nonlinear model of streamwise instabilities (once again, for the case of a Blasius-type power-law flow). To model these, Duck and Owen introduced perturbations of arbitrary finite amplitude ϵ at the leading edge

$\xi = 0$. To facilitate the streamwise development of these instabilities, the authors relaxed the assumption of a fixed $O(\xi^{\lambda})$ growth-rate and reformulated the governing equations to second-order accuracy (retaining nonlinear terms up to order $O(\epsilon^2)$). The numerical results were somewhat startling: Depending on the sign of ϵ, the instabilities either attained a well-defined maximum amplitude or produced a total breakdown in the flow. The plateau phenomenon occurred whenever ϵ was chosen to yield a positive perturbation shear stress, ie $\widetilde{\tau}_0 > 0$ and $\widetilde{\sigma}_0 > 0$; this is illustrated in Figure 7 of their paper for the case of ZPG Blasius-type flow. Conversely, negative shear stress resulted in a finite-time breakdown (see their Figure 8). According to the authors, this is not a numerical artefact; rather, it is physically meaningful and describes a collision process between an incoming wave-like disturbance and the vertical wall $\zeta = 0$. The authors round off their analysis with a physical interpretation of the plateau phenomenon: it corresponds precisely to a transition from a Blasius-type configuration to the corresponding non-Blasius state. This in turn lends support to the conjecture of Ridha (1992) that non-Blasius flows are more likely to be observed in practice.

We sound a word of caution, however, on interpreting the findings of Duck and Owen (2004). Certainly, their paper suggests that Blasius-type flows are unstable to streamwise instabilities, and consequently, liable to undergo a transition towards a stable, non-Blasius state. Given the large length scales involved, however, a complete transition of this type is unlikely to be observed in the laboratory. This is best appreciated by re-examining Figure 7 of their paper, illustrating the nonlinear development of streamwise instability for Blasius-type flow at $n = 0$ (ie in the absence of a pressure gradient). Arising at the leading edge $\xi = 0$, the transition is still only approximately 80% complete at the downstream location $\xi = 10$ (ie $x = 100$). Such a large value of x would be somewhat peculiar in an engineering context: Since x is defined relative to an (admittedly arbitrary) characteristic length L, it follows that $x = O(1)$ in general. Be that as it may, we may safely state that the laminar boundary layer would be at least ten times thicker[4] at $x = 100$ than at $x = 1$, and hence, much more susceptible to classical eigenmode instabilities. Suppose, for example, that the reference Reynolds numbers are of order $Re = O(10^4)$ and $Re_\delta = O(10^2)$; then the equivalent downstream values at $x = 100$ would be $Re_x = O(10^6)$ and $Re_\delta = O(10^3)$ respectively. The latter values lie well within the domain of exponential eigenmode instability, and lead us to hypothesize that the

[4]Actually, the growth-factor would be slightly less than ten under the assumption of fully laminar flow (since a Blasius-type boundary-layer is somewhat thicker than its non-Blasius equivalent). The magnification factor would exceed ten, however, in the event that an eigenmode instability arises at $1 < x < 100$ and overwhelms the transition to a laminar non-Blasius state.

transition from Blasius to non-Blasius form would in practice be overwhelmed by viscous instabilities.

We close our literature review by revisiting the Duck *et al.* (1999) paper, which examines several classes of similar and non-similar laminar corner flows. An interesting section of their paper models the effect of blowing or suction, ie of non-zero normal velocity at the walls. Although somewhat speculative, this work may have practical applications. By controlling the boundary-layer thickness, it has been suggested, one may influence the stability characteristics of the flow, including the streamwise location of transition from laminar to turbulent flow. Although this technique is not exploited in current commercial aircraft, it has been trialled experimentally by means of aircraft wings with laser-drilled perforations.

1.3.8 Research plan

The published literature on laminar corner flows evinces a wide degree of variation in both methods and findings. This is true even for the simplest corner-flow configuration, namely ZPG laminar flow internal to a square corner (§1.3.2 and §1.3.3). Crucially, the theoretical literature is inconclusive regarding the well-founded conjecture of Zamir (1981) that ZPG laminar flow is significantly less stable its 2D counterpart, the well-known Blasius boundary layer.

Our first objective, therefore, is to conduct a thorough study of ZPG laminar square-corner flow. We begin in Chapter 2 with an in-depth literature review of the laminar flow itself, noting the various numerical methods and asymptotic formulae which have been used to compute it. We conclude in §2.4 by presenting our own data set and discussing its salient features. An eigenmode stability analysis of this flow follows in Chapter 3.

Our second objective is to pioneer the study of laminar flows external to a corner. We anticipate that the analytical and numerical tools developed for internal-corner flows can be readily adapted to the case of an external square corner (opening angle $\Phi = 3\pi/2$). Chapter 4 analyses this laminar flow and attempts an eigenmode stability analysis. We compare our results with those of Moinuddin *et al.* (2001, 2004) for a turbulent corner boundary layer.

Our third objective is to conduct a systematic analysis of oblique corner flows (§1.3.4) and/or pressure-driven corner flows (§§1.3.6 and 1.3.7). To the best of our knowledge, no 2D eigenmode stability analysis has yet been conducted for an oblique corner, or for a square corner with favourable pressure gradient (FPG). This deficiency is slightly puzzling, given the evidence of Zamir (1981) laminar corner flow is readily stabilized by even a mildly favourable pressure gradient.

Our fourth and final objective is of a slightly more general nature. We wish to review and compare the accuracy and efficiency of a variety of numerical methods applicable to 3D laminar flows and eigenmode instabilities. Candidates for this review include: spectral and pseudospectral methods for spatial domains; the GMRES algorithm for solution of nonlinear equations; the Arnoldi eigensolver for large asymmetric matrices; and the eigensolver of Otto and Denier (1999) for large sparse matrices. More recently, Theofilis (2003) has presented a comprehensive review of computational techniques for instability problems in fluid mechanics. This final objective is partially realized in our study of ZPG square-corner flows (Chapters 2–4). A detailed survey of more general corner flows has been precluded by technical and time constraints.

1.4 Literature survey: Unsteady pipe flow

1.4.1 Blocked pipes

Our study of unsteady fluid flow is motivated primarily by the transient behaviour in suddenly-blocked pipe flows. We begin with a simple model of a pipe-closure event. Consider a straight, horizontal pipe of length L, diameter D and radius $R = D/2$ located on the domain $0 \leq x \leq L$. Assume that the pipe is initially ($t < 0$) filled with water (or some other Newtonian fluid) flowing steadily downstream with cross-sectional mean velocity $U^* > 0$ and Reynolds number

$$Re = \frac{U^* D}{\nu} \qquad \text{(laminar or turbulent flow)} \tag{1.32}$$

where ν is the kinematic viscosity of the fluid. In the event that the flow is laminar, the cross-sectional flow profile is parabolic, namely

$$u(r) = U_c \left(1 - \left(\frac{r}{R}\right)^2\right) \qquad \text{(laminar flow only)} \tag{1.33}$$

where the centreline velocity U_c is given by the simple formula

$$U_c = 2U^* \qquad \text{(laminar)} \tag{1.34}$$

and yields the equivalent definition

$$Re = \frac{U_c R}{\nu} \qquad \text{(laminar).} \tag{1.35}$$

At time $t = 0$, a blockage is induced at the downstream end $x = L$. However, owing to the slight compressibility of water, a finite time elapses before the blockage is 'felt' at any given upstream location $x = x^*$. This time lag is given by $\Delta t = (L - x^*)/c$

where c is the acoustic wavespeed[5]. Thus, the pressure wave reaches the upstream end $x = 0$ after a finite time $t = t_w = L/c$, and the blockage is not complete until $t = t_c + t_w$, where t_c is the duration of the closure event at the upstream end (which may vary from as little as few milliseconds for a high-speed solenoid valve, to seconds or even minutes in the case of a graduated closure of a major pipeline). However, this does not generally correspond to the conclusion of the transient event. While the exact nature of the event depends on the upstream and downstream conditions (see §3.3 of Wylie and Streeter, 1982), the flow will in general oscillate in the following fashion. On reaching the downstream end $x = 0$ the pressure wave is immediately reflected upstream, thereby changing the mean flow $U(t, x)$ from $U = 0$ to $U \approx -U^*$ throughout the pipe. On returning to the downstream end $x = L$ at $t = 2t_w$, the pressure wave is again reflected downstream and returns the net flow to zero ($U = 0$). The pressure wave is then reflected at $x = 0$ and restores the original pre-blockage flow ($U \approx +U^*$). Due to viscous shear stress on the pipe walls, however, the magnitude $|U|$ of the flow is now somewhat less than its original value of U^*. This cycle repeats indefinitely with a time period of $4t_w$ until halted by the cumulative effects of viscous damping. This process is illustrated schematically in Fig. 1.4 of Wylie and Streeter (1982).

In the case of a rapid and complete blockage ($t_c < t_w$), the induced pressure wave has a maximum amplitude of

$$\Delta P \approx \rho c U^* \tag{1.36}$$

where ρ denotes the fluid density. For water at room temperature with $U^* = 1\,\mathrm{m\,s^{-1}}$, this would equate to a pressure of 1.3 MPa, or equivalently, to a head of approximately 130 metres. Such large transient pressures can prove extremely costly in terms of ruptured pipelines and capital requirements (high-pressure pipelines and surge towers). Furthermore, the water-hammer phenomenon produces transiently low and/or negative pressures, which in turn may result in cavitation and temporary water-column separation. (Further destructive pressures may be caused by the subsequent reconnection of the water column.) To avoid such destructive effects, it is common practice to operate a pipeline at much higher steady-state pressures than would otherwise be necessary.

Oscillatory behaviour is not the sole reason for the lengthy duration of the water-hammer event. Even when the mean flow $U(t, x)$ is zero at some given streamwise location x, the local fluid velocity $u(t, x, r)$ at any given point is in general non-

[5]The velocity of sound c in fresh water at $20^O C$ is $1482\,\mathrm{ms^{-1}}$. In laboratory and field work, however, it is advisable to determine c experimentally, since the empirical and standard values may differ by as much as 10%.

zero. It is shown in §2 of Weinbaum and Parker (1975) that the immediate effect of the initial pressure wave is to reduce u everywhere by an amount equivalent to the original mean velocity U^*. This momentarily violates the no-slip condition at the pipe wall and results in a locally reversed flow, such that $u(t,x,r) < 0$ near the wall and $u(t,x,r) > 0$ in the core of the pipe. An unsteady boundary layer thus develops on the wall as the flow adjusts to the new conditions. As this boundary layer diffuses toward the centre of the pipe under the constraint that $U = 0$, it generates a secondary pressure wave.

For more complex closure regimes, or when more accurate data is required, it is necessary to solve the one-dimensional water-hammer equations. In dimensional form, these are given by

$$g\left(\frac{\partial H}{\partial t} + U\frac{\partial H}{\partial x}\right) + c^2\frac{\partial U}{\partial x} = 0 \qquad \text{(continuity)}, \tag{1.37a}$$

$$\rho\left(\frac{\partial U}{\partial t} + U\frac{\partial U}{\partial x}\right) + \rho g\frac{\partial H}{\partial x} + \frac{(2\pi R)\sigma}{\pi R^2} = 0 \qquad \text{(momentum)}, \tag{1.37b}$$

where

$$g = \text{acceleration due to gravity}, \tag{1.38a}$$

$$R = \text{pipe radius}, \tag{1.38b}$$

$$\mu = \text{fluid viscosity}, \tag{1.38c}$$

$$c = \text{acoustic wavespeed}, \tag{1.38d}$$

$$U(t,x) = \text{cross-sectional mean velocity}, \tag{1.38e}$$

$$P(t,x) = \text{dynamic pressure}, \tag{1.38f}$$

$$H(t,x) = \text{dynamic head defined by } \rho g H = P + \tfrac{1}{2}\rho U^2, \tag{1.38g}$$

$$\sigma(t,x) = \text{viscous shear stress on the pipe wall, given by } \mu[\partial u/\partial r]_{r=R}. \tag{1.38h}$$

The nonlinear terms in (1.37) are negligible whenever $U \ll c$ (as is usually the case). The water-hammer equations thus reduce to

$$\frac{\partial H}{\partial t} + \frac{c^2}{g}\frac{\partial U}{\partial x} = 0 \qquad \text{(continuity)}, \tag{1.39a}$$

$$\frac{\partial H}{\partial x} + \frac{1}{g}\frac{\partial U}{\partial t} + J = 0 \qquad \text{(momentum)}, \tag{1.39b}$$

where the dimensionless quantity

$$J(t,x) = \frac{2\sigma}{\rho g R} \tag{1.40}$$

expresses frictional losses in terms of head-loss per unit length. These equations are usually solved using the Method of Characteristics by first transforming them into

the frames of reference of the upstream and downstream pressure waves as follows:

$$\pm\frac{1}{c}\frac{\mathrm{d}H}{\mathrm{d}t} + \frac{1}{g}\frac{\mathrm{d}U}{\mathrm{d}t} + J = 0 \qquad \text{along} \qquad \frac{\mathrm{d}x}{\mathrm{d}t} = \pm c. \tag{1.41}$$

In the case of a single pipe of length L, this pair of simultaneous equations may be conveniently solved using a finite-difference scheme with uniform step-sizes of $\Delta x = L/N$ and $\Delta t = \Delta x/c \equiv t_w/N$. The discretization is performed in a staggered fashion in accordance with the characteristic equations. Since we will not use the Method of Characteristics in our work, we omit its details, instead referring the reader to Chapter 3 of Wylie and Streeter (1982).

The principal difficulty with the Method of Characteristics is the need for a reliable model of the unsteady shear stress σ, which, in conjunction with the boundary conditions at the ends of the pipe, determines the damping rate of the pressure transients. The traditional approach is to invoke the following standard formulae for shear stress in steady pipe flows, replacing the notional steady mean velocity $U = U^*$ with an unsteady mean velocity of the form $U(t, x)$:

$$\sigma = \frac{4\mu U}{R} \qquad \text{(laminar)}, \tag{1.42a}$$

$$\sigma = \tfrac{1}{8}\,\epsilon\rho U^2\,\mathrm{sgn}(U) \qquad \text{(turbulent)}, \tag{1.42b}$$

$$J = \frac{\epsilon U|U|}{4gR} \qquad \text{(turbulent)}, \tag{1.42c}$$

where $\epsilon \ll 1$ is the Darcy–Weisbach friction factor (usually denoted by f); it varies weakly as a function of Reynolds number and strongly as a function of the roughness of the pipe wall (see, for example, §8.4 of Munson *et al.*, 2002). The friction formulae (1.42) are indeed accurate for steady pipe flows, but significantly underestimate the frictional damping effects in unsteady flows. That this quasi-steady model is inaccurate is hardly surprising, given that it assigns a value of $\sigma = 0$ or $J = 0$ whenever $U = 0$. In particular, the quasi-steady model completely neglects the phenomenon of reverse flow, which is capable of producing a non-zero shear stress even when $U = 0$.

So long as engineers were principally interested in the maximum amplitude of the water-hammer pressure wave, they were not unduly concerned with inaccuracies in their friction models. In recent years, however, interest in this issue has been revived by the development of Inverse Transient Analysis (ITA) as a cost-effective tool for routine monitoring of pipeline systems. This technique employs artificial pressure transients as a remote-sensing tool to detect or locate leaks and ruptures in pipe networks. Crucially, its implementation requires accurate data on the full transient event (especially regarding the damping rate of the pressure envelope) rather than

just the first cycle of the pressure wave, in order to distinguish between normal and abnormal responses to a water-hammer event of arbitrary magnitude. This in turn requires accurate theoretical models of unsteady shear stress in pipe flows. Thus, ITA is the principal motivation for our own work on unsteady pipe flows. Since, however, we will not need to implement this technique, we merely refer the reader to two recent papers for a detailed discussion of inverse transients. Wang *et al.* (2002) provides an algorithm for identifying the magnitude and location of a leak in a single pipeline. Their technique entails a Fourier analysis of the observed pressure transients, and is amenable to friction models of a fully-unsteady nature. Liggett and Chen (1994) implement ITA for the case of a complex multi-node pipe network, using the Method of Characteristics in conjunction with a block-matrix optimisation algorithm. Unfortunately the accuracy of this method is somewhat compromised by the authors' reliance on the traditional quasi-steady friction model (1.42). In addition, equation (4) of their paper specifies an incorrect sign for the friction term.

We close this section by reviewing the literature on the topic of unsteady friction models, beginning with that of Zielke (1968) for the case of laminar flow. Zielke's model expresses the shear stress as a sum of quasi-steady and unsteady components:

$$\sigma(t,x) \;=\; \frac{4\mu}{R}\left[U(t,x) \;+\; \tfrac{1}{2}\int_0^t \frac{\partial U}{\partial t}(t',x)\,W(t-t')\,\mathrm{d}t'\right] \qquad \text{(laminar)}. \tag{1.43}$$

The fully-unsteady component in (1.43) takes the form of a convolution of the recent flow history, with weighting function W given by

$$W(t) \;=\; \begin{cases} 0.282\,\tau^{-1/2} \;-\; \frac{5}{4} \;+\; O(\tau^{1/2}) & \text{for} \quad \tau \lesssim 0.02, \\ \mathrm{e}^{-26.4\tau} \;+\; \mathrm{e}^{-70.8\tau} \;+\; \text{h.o.t.} & \text{for} \quad \tau \gtrsim 0.02, \end{cases} \tag{1.44}$$

where

$$t^* \;=\; R/U_c \tag{1.45}$$

is the advective time-scale;

$$t_d \;=\; R^2/\nu \;\equiv\; Re\,t^* \tag{1.46}$$

is the (slow) diffusion-based time-scale; and

$$\tau \;=\; t/t_d \;\equiv\; Re^{-1}(t/t^*) \tag{1.47}$$

is the corresponding dimensionless time variable. The diffusion time-scale is typically quite large; for example, a water-filled pipe of diameter 1 cm yields $t_d = 25\,\mathrm{s}$. Zielke's formula (1.43) reveals a pronounced time-lag effect between the local acceleration $\partial U/\partial t$ and the local friction σ, vividly explaining why the quasi-steady model significantly underestimates the damping effect of wall shear stress. In particular, a rapid and complete blockage produces reversed flow with $U(t,x) = 0$ but

$u(t, x, r) \neq 0$. Under these circumstances, the first portion of (1.44) arises from a diffusion-type wall boundary layer of width $\delta(t)$ where

$$\delta/R = O(\tau^{1/2}) \qquad \text{for} \qquad 0 < \tau \lesssim 0.05, \tag{1.48}$$

while the second portion of the formula indicates exponential decay $u \to 0$ of the fluid motion as a function of time. Zielke's analysis is rigorous, and could in principle predict the instantaneous laminar flow profiles for any prescribed transient event. Zielke, however, chooses to devote the remainder of his paper to validation of his unsteady friction model using the Method of Characteristics.

Since most engineering flows are turbulent rather than laminar, there is a clear need for a good model of shear stress in unsteady turbulent flows. A fairly crude model was presented by Wood and Funk (1970). A quarter-century later, Vardy and Brown (1995) proposed a semi-theoretical model of unsteady turbulent friction. Their model is qualitatively similar to Zielke's laminar-flow model, while simultaneously incorporating some standard empirical data on the properties of steady turbulent pipe flows; consequently, it purports to be accurate over a wide range of Reynolds numbers and unsteady flow regimes. Though somewhat complex in its most general form, it is computationally tractable (when used in conjunction with the Method of Characteristics) and even yields some semi-analytic results for the special cases of instantaneous blockage or uniformly accelerated mean flow. In particular, laminar and turbulent flows are found to be qualitatively similar regarding their initial response to a rapid blockage (even though the effective viscosity is much higher in the turbulent case). The fully-2D unsteady model of Pezzinga (1999) is likewise valid over a wide range of Reynolds numbers; unlike the Vardy and Brown model, however, it is applicable to both smooth- and rough-walled pipes.

The fully-unsteady friction models of Vardy and Brown (1995) and Pezzinga (1999) are accurate but computationally intensive. Much time and effort has therefore been expended on a quest for a satisfactory *quasi-steady* 1D model of unsteady friction. For example, Ghidaoui and Mansour (2002) approximate the Zielke and Vardy and Brown models without retaining the complete history of the flow at all computational nodes; their model is validated against a combination of published experimental data on low-speed unsteady turbulent flows and theoretical data drawn from the Pezzinga and Vardy and Brown papers. The literature review of Bergant *et al.* (2001) lists and classifies no fewer than thirty extant friction models and five distinct *categories* of quasi-steady models. The authors then report on their own water-hammer experiments in laminar and low-speed turbulent flows (generated in hydraulically smooth copper pipes for Reynolds numbers in the range $10^3 < Re < 10^4$). Not surprisingly, they find that the fully-unsteady models provide

a much better match with measured pressure data than the traditional quasi-steady model (which entirely neglects unsteady effects). They also report good performance from the Zielke laminar-flow model (1.43) for (low-speed) turbulent flows, suggesting that the flow is not in a fully developed turbulent state throughout the transient event. Finally, the authors recommend a quasi-steady friction model of the form

$$J(t,x) \;=\; \frac{\epsilon U|U|}{4gR} \;+\; \frac{\kappa}{g}\left(\frac{\partial U}{\partial t} \;+\; s\,c\,\frac{\partial U}{\partial x}\right) \tag{1.49}$$

where κ is a dimensionless constant and s is a sign function indicating whether the flow is accelerating or decelerating:

$$s \;=\; \mathrm{sgn}\left(U\,\frac{\partial U}{\partial x}\right). \tag{1.50}$$

It was the work of Lambert *et al.* (2001) which stimulated our own interest in the subject of unsteady pipe flows. In this paper, the authors propose a novel quasi-steady friction model which reproduces the crucial time-lag effect without requiring computer storage of the complete history of the flow at all computational nodes. As a *boundary-layer growth model*, it estimates the instantaneous local boundary-layer width $\delta(t,x)$ and corresponding shear stress $\sigma(t,x)$ on the basis of elapsed time since the (most recent) passage of the primary pressure wave. In this model, the fundamental formulae for δ and σ are drawn from those describing the spatial development of a (steady) boundary layer in the entrance region of a pipe. In the case of laminar flow, these formulae are qualitatively equivalent to equation (1.17) for steady laminar flow over a flat plate. The authors implemented their model using the Method of Characteristics and validated it using the same experimental apparatus employed by Bergant *et al.* (2001); it clearly outperformed the traditional quasi-steady model, especially in predicting the phase pattern of the pressure wave. The authors believed their model showed good potential for refinement (including extension to high-speed turbulent flows), but expressed some unease on the grounds that their model ultimately relies on steady-flow data. Thus, the authors' work highlights the continuing need for an improved understanding of the structure and evolution of unsteady boundary layers in the laminar, transitional and turbulent regimes.

Recently, Vitkovský *et al.* (2006) gave another review of unsteady friction models. Whereas Bergant *et al.* (2001) classified the extant unsteady-friction models, Vitkovský *et al.* (2006) commence by classifying the transient events themselves. The authors then adduce theoretical and experimental evidence to the effect that the Zielke and Vardy and Brown models perform satisfactorily for all flow types, whereas the modified quasi-steady model (1.49) is qualitatively incorrect for some

types of transient events (typically those involving a valve opening). Furthermore, this model is shown to perform poorly in predicting the phase response of the pressure waveform, even in those instances where it (accurately and usefully) predicts the damping rate of the pressure envelope. The authors conclude by suggesting that "some previous [apparent] good fits with experimental data are due to numerical error rather than [the intrinsic accuracy of] the unsteady friction model." Once again, therefore, it seems that there is no substitute for theoretical modelling. Certainly, empirical models can be useful, efficient and reliable; but they should always be tested rigorously against both theoretical and experimental evidence.

1.4.2 Physiological applications

In the field of physiology and medicine, one encounters unsteady laminar, transitional and turbulent flows in blood vessels and catheters. In fact, it was blood flow which motivated Poiseuille in 1840 to study the laminar flows which bear his name. A century later, Womersley (1955) was motivated to present an analytical model of periodic laminar flow in a pipe. His solution highlights the competing role of the viscosity- and frequency-based time scales, and provides a quantitative explanation of the phase-lag effect between velocity and pressure. Prior to the 1970s, however, little was known (either experimentally or theoretically) about the structure of unsteady flows in the transitional and turbulent regimes.

The development of hot-film and hot-wire anemometry enabled Seed and Wood (1971) and Nerem and Seed (1972) to measure instantaneous blood velocities in the aortas of dogs. These experiments were prompted partly by fundamental scientific enquiry into human physiology, and partly by the quest to develop reliable, non-invasive methods of cardiac diagnosis:

> [It has been] postulated that low wall shear rates are important in dictating sites of atherogenesis. Similarly, flow regimes are of interest in terms of their influence on pressure-flow relations, mixing and mass-transfer processes, and the generation of audible sounds.

The authors found that aortic blood flow is generally transitional in nature, but varies in character from laminar through to fully turbulent. The measured range of Reynolds number was $1200 \leq Re_{\max} \leq 5500$ (based on aortic diameter and maximum centre-line velocity), suggesting that aortic flows are slightly less stable than steady Newtonian flows[6]. A spectral analysis of the observed turbulence revealed

[6]The typical range of instability for Hagen–Poiseuille flow is $2000 \lesssim Re_c \lesssim 4000$ (based on diameter and mean/bulk velocity). Blood behaves as a Newtonian fluid in all but the smallest

that velocity fluctuations lay predominantly in the frequency range of 50–500 Hz, corresponding to low-frequency audible sounds (and potentially providing opportunities for non-invasive cardiac diagnosis).

Two further features of the observed aortic flow are noteworthy. Firstly, the authors were unable to detect a boundary layer *in vivo*, even in cases where the flow was apparently laminar. While this negative observation is partially attributable to the low resolution of their instrumentation (the probe being restricted to distances of at least 2 mm from the aortic walls), it does suggest that Poiseuille flow is a poor approximation to aortic blood flow in dogs and humans. We hypothesize that the heart-beat time-scale is simply too short to produce well-developed laminar boundary layers[7]. Secondly, the authors found the turbulent fluctuations to be significantly more prominent under diastole (ie deceleration) than systole (positive acceleration). According to the authors, this indicates that decelerating flows are inherently more unstable than accelerating flows. This hypothesis is distinctly plausible, since it is well known that eddy viscosity is much higher under deceleration than equivalent acceleration (see, for example, §8.4.2 of Munson *et al.*, 2002). Nevertheless, after closely examining the authors' published data, we suggest the following alternative hypothesis. Noting that the duration of the systole phase may be as short as $O(10^{-2})$ seconds, we suggest that the instability actually arises under systole but generally does not become visible until the onset of diastole. In any event, the flow subsequently relaminarizes during either mid- or late-diastole, depending on the end-systole Reynolds number $Re_{\max}$ of the flow.

The findings of Seed and Wood (1971) and Nerem and Seed (1972) prompted Weinbaum and Parker (1975) to model the sudden blockage of steady laminar flow in a pipe or channel. Discussion of the experimental portion of their study is limited

capillaries, where the capillary radius is comparable to that of blood cells. The kinematic viscosity ν of warm blood is $4 \times 10^{-6}\,\mathrm{m^2\,s^{-1}}$, which is approximately four times that of water at room temperature. Seed and Wood (1971) and Nerem and Seed (1972) conducted their experiments *in vivo* on large- and medium-sized dogs respectively in both resting and drug-stimulated states. The apparatus was pre-validated against artificial flows generated within a life-sized model of a canine aorta. The aortic diameters of the canine subjects ranged from 7.5 mm to 16 mm, depending principally on where the measurements were taken (ie at an ascending, descending or arched location). Streamwise velocity measurements were made at multiple radial locations; the authors do not report bulk velocities.

[7]Steady pipe-Poiseuille flow develops over a time scale of κt_d, where t_d is defined by (1.45) and $\kappa = O(10^{-1})$ is a fundamental constant. Consequently, the *entrance length* L_e for laminar flow (ie the development length of the laminar boundary layer) is very large: $L_e \approx (Re/15)D$ (Munson *et al.*, 2002). For the given aortic data, these values would translate to $\Delta t = O(1)$ seconds and $L_e = O(10^2)$ cm respectively. The latter figure represents a conservative estimate, and is consistent with the *in vitro* data presented in Figure 2 of Seed and Wood (1971).

to a single paragraph in the introduction of the paper; it was found that Poiseuille pipe flow decays in laminar fashion if and only if the pre-blockage Reynolds number is below 2000. The remainder of the paper presents a detailed theoretical analysis of the laminar decay process following the sudden blockage of Poiseuille and pipe-Poiseuille flows. Unfortunately their analysis is marred by one or two errors. The authors were apparently unaware of Zielke (1968), whose rigorous analysis could readily have been extended to yield the required data. Instead, Weinbaum and Parker (1975) relied on a less accurate technique, namely the Pohlhausen method of boundary-layer matching.

Hall and Parker (1976) built on the work of Weinbaum and Parker (1975) by analysing the hydrodynamic stability of the decaying laminar flow in a channel. They employed a traditional eigenmode analysis, based on the quasi-steady assumption that the eigenmode instabilities develop on a time scale much faster than that of the underlying laminar flow. The authors find inviscid-type instabilities above $Re \approx 150$, which they attribute to the inflectional nature of the instantaneous flow profiles. This critical Reynolds number is surprisingly low, being approximately one order of magnitude lower than that observed experimentally for either *steady* channel flow or blocked *pipe* flow (Weinbaum and Parker, 1975).

A quarter-century later, Ghidaoui and Kolyshkin (2001) performed an analogous eigenmode stability analysis for unsteady pipe flow. This engineering-oriented study assumes instantaneous blockage (as in Hall and Parker, 1976) but encompasses a variety of flow configurations: partial blockage; finite-length pipes (with reflection of the pressure wave from the upstream end of the pipe); and even low-speed turbulent flows, with pre-blockage Reynolds number $10^4 < Re < 10^5$. For the simplest case, ie rapid and complete blockage of Poiseuille flow, the authors report a critical Reynolds number of $Re_c \approx 550$. This result must be treated with caution, however, for the following reasons. Firstly, as with Hall and Parker (1976), the authors' findings hinge on the validity of the quasi-steady approximation. Secondly, as will be discussed in §6.5, the accuracy of the authors' laminar-flow data is poor. Thirdly, the stability minimum $Re_c \approx 550$ is attained only after the elapse of an appreciable time τ from the blockage event. In general, Re_c is found to be an exceptionally sensitive function of τ; indeed, it apparently approaches infinity in the limit $\tau \to 0$. This asymptotic property appears to mirror the well-known failure of linear eigenmode theory for Poiseuille and Hagen–Poiseuille flows.

1.4.3 Theoretical considerations

Aside from any immediate practical considerations, pipe blockage constitutes a useful field of study on theoretical grounds alone. The response of a moving fluid to a downstream blockage provides a relatively tractable case study in the field of unsteady fluid flows. Depending on whether the blockage is total or partial, and whether the pressure wave is multiply reflected, the flow may be variously treated as transient, transiently unsteady, or quasi-periodic.

Unsteady fluid flows, though ubiquitous in real life, remain poorly understood and difficult to analyse via standard theoretical or computational tools. The limitations of our understanding of unsteady flows are concisely documented in §1 of Das and Arakeri (1998):

> Unsteady boundary layer separation is not yet fully understood, and there is no specific criterion for its occurrence. ... There is no satisfactory linear stability analysis for velocity profiles whose mean value is changing with time. ... For example, in oscillating pipe flow, theory predicts a critical Reynolds number (based on Stokes layer thickness) of 82, whereas the experimentally observed value is in the range 300 to 500; and turbulent bursts are observed during the deceleration phase, whereas stability theory predicts the most unstable velocity profile to occur during the start of the acceleration phase.

Thus, the theoretical predictions regarding the stability of unsteady laminar pipe flow fail in both quantitative and qualitative senses.

In fact, classical stability theory throws up qualitatively incorrect predictions even for some steady laminar flows in simple geometries. There is now considerable evidence to support the conjecture of Trefethen *et al.* (1993) that classical stability theory is reliable only for flows subject to specific destabilizing forces, as in the case of thermal gradients (Rayleigh–Bénard convection) and centrifugal forces (Taylor and Görtler vortices). Conversely, agreement between theory and experiment is often poor when the instability mechanism is essentially viscous. Well-known examples of the latter class include Couette flow, plane-Poiseuille flow and pipe-Poiseuille flow. Experimentally, all of these become unstable at $Re_c = O(10^3)$. Yet classical linear theory predicts that Couette and pipe-Poiseuille flows are unconditionally stable, and that plane-Poiseuille flow is stable for $Re < 5772$. Furthermore, the predicted instability in plane-Poiseuille flow for $Re > 5772$ disagrees qualitatively with experiment (see, for example, Figure 3 of Trefethen *et al.*, 1993): in keeping with Squire's theorem, it represents a slowly-growing two-dimensional perturbation, quite unlike the vigorous three-dimensional streamwise vortices actually observed.

A possible explanation for these discrepancies is the well-known fact that eigenmodes predict only the long-term behaviour of a given linear system. Whether this is a reliable guide to short-term behaviour depends on whether the eigenmodes are near-orthogonal and non-degenerate: where this is not the case, transient growth may be possible even if all individual eigenmodes decay. What has not been realised until relatively recently is that the eigenmodes of some flows are far from orthogonal. This is indeed the case for Couette and plane-Poiseuille flows. For each of these flows, Butler and Farrell (1992), Trefethen *et al.* (1993) and Reddy and Henningson (1993) were able to exhibit linear combinations of eigenmodes which interfere destructively in the early stages, before separating out to produce significant transient growth in the intermediate stage. Describing these transient instabilities as *pseudomodes*, the authors proceeded to develop a theory of Transient Stability Analysis (TSA). In a purely linear TSA model, the pseudomode eventually decays in the exponential manner predicted by classical eigenmode theory. In practice, however, it is hypothesized that the pseudomode may attain a critical amplitude beyond which nonlinear effects destabilize the flow. This conjecture has some support in the small-scale numerical experiments reported in Trefethen *et al.* (1993), Gehbart and Grossmann (1994), Baggett *et al.* (1995) and Meseguer and Trefethen (2003). Nonlinear studies, such as those in Boberg and Brosa (1988), provide theoretical confirmation of the nonlinear and three-dimensional nature of transition in steady pipe flows. Shan *et al.* (1999) presented a more ambitious study, based on 3D direct numerical simulation from an initial state of steady pipe-Poiseuille flow; they succeeded in simulating a puff and a slug at Reynolds numbers of 2200 and 5000 respectively.

Pseudomode theory furnishes two convenient computational tools for the analysis of linear transient growth within a steady underlying laminar flow. The first technique treats the classical eigenmodes as basis functions and yields an infinitesimal 'optimal' pseudomode which typically attains a maximum amplification factor of $g_{\max} = Re/Re_0$ for some constant $Re_0 \ll Re_c$ (where Re_c is the stability limit from classical theory). Its transient characteristics are readily computed under the assumption of linear growth within a steady underlying laminar flow. The second technique returns the *pseudo-spectrum* of the governing equations (essentially a classification of the parameter space on the basis of 'closeness' to a classical eigenmode), and has the physical interpretation of measuring the transient response of the flow to an arbitrary continuous-time perturbation. A linear transient of this type typically accumulates energy over an $O(Re)$ time period, eventually reaching a quasi-steady state with amplification factor $g_{\max} = O(Re^2)$.

Since pseudomode stability theory was originally developed for steady flows, its

relevance to unsteady flows is not entirely clear. Recently, however, Scandura (2003) attempted a transient analysis of the (highly unsteady) laminar flow in a suddenly blocked channel. In particular, he relaxed the quasi-steady approximation inherent in the stability analysis of Hall and Parker (1976) and widened the class of instabilities to include transient pseudomodes. His transient analysis was limited to randomly generated pseudomodes, together with the leading eigenmode of instability; no attempt was made to optimize transient growth in a rigorous or systematic manner. Nevertheless, Scandura's results are valuable and suggest that the laminar flow is stable well above the critical Reynolds number $Re_c = 199.6$ predicted by quasi-steady eigenmode theory. Incidentally, the Hall and Parker paper yields an even lower stability estimate $Re_c = 148$ for this flow. The cause of this discrepancy is not entirely clear, although it may be due to inaccuracies in the laminar-flow data of Weinbaum and Parker (1975).

On the experimental side, Das and Arakeri (1998) and Allen and Chong (2000) studied unsteady pipe flows in the laminar and transitional regimes. Das and Arakeri used a stepper motor to produce a variety of flows (impulsive, oscillatory, or linearly accelerated) with maximum flow velocities of the order of $Re = O(10^3)$. With the aid of flow visualisation techniques, they vividly demonstrated the processes of unsteady boundary-layer development and transition to turbulence. The leading instability, described by the authors as asymmetric, appears to correspond to the period-one azimuthal instability predicted by Ghidaoui and Kolyshkin (2001) for the case of a rapidly blocked pipe. Das and Arakeri (1998) also attempted a theoretical analysis, estimating the instantaneous laminar flow profiles and their respective stability characteristics. Their stability data must be treated with some caution, since it relies on the quasi-steady approximation; nevertheless, it is valuable in identifying transitional phenomena in unsteady flows and quantifying the temporal and spatial scales of induced vortices. Furthermore, it highlights the significance of flow reversal, a phenomenon also encountered in water-hammer events.

Allen and Chong (2000) used a piston and stepper motor to produce unsteady pipe flows of the power-law form $u \propto t^m$ for m constant. (For practical reasons the piston was kept fixed within a moving pipe.) Whereas Das and Arakeri studied the behaviour of the flow at an arbitrary streamwise location, Allen & Chong (2000) focussed on the vortex formed directly in front of the piston. This represents a useful model of unsteady flow within a locally-square corner, notwithstanding the cylindrical geometry. The authors were able to confirm that the vortex is produced by the phenomenon of boundary-layer roll-up and fluid entrainment. Sensitive measurements showed that the vortex is stable at quite large Reynolds numbers, and that it contains both viscous and inviscid zones (ie dominated by viscous and iner-

tial forces respectively). The vortex structure was found to be considerably weaker in intensity than predicted by theory. At the same time, however, its spatial scale δ expanded over time at a considerably faster rate than expected ($\delta \propto t^{0.85+0.7m}$). Finally, the authors were able to identify a secondary vortex wrapped around the outside of the primary vortex, and having the same growth rate.

1.4.4 Research plan

The goal of our research program is to elucidate the process whereby fluid comes to rest following the rapid blockage of a steady laminar pipe flow. The core component of our program builds directly on the work of Zielke (1968), Weinbaum and Parker (1975), Hall and Parker (1976), and Ghidaoui and Kolyshkin (2001). Comprising Chapters 6–8, this section examines the laminar decay process from an arbitrary distance upstream of the blockage, so that the streamwise flow is effectively of the one-dimensional form $u(t, r)$. We may assume without loss of generality that $t = 0$ corresponds to the arrival of the primary pressure wave which establishes the blockage. To simplify the analysis, we assume that the closure time t_c is negligible; that the blockage is total; and that the pipe is arbitrarily long (implying the absence of any reflected pressure wave). It is clear from §1.4.1 that any of these assumptions may be relaxed without great difficulty. These constraints allow us to focus on fundamental questions regarding the behaviour of unsteady fluid flows.

Our core research is structured as follows. In Chapter 6 we compute this unsteady laminar flow to a high degree of precision, together with its associated secondary pressure wave. In Chapter 7 we perform an eigenmode stability analysis of this flow; the resulting critical Reynolds number Re_c is in general a function of the elapsed time τ since the blockage event, where τ is defined by (1.46). This stability analysis is only approximate at best: like that of Ghidaoui and Kolyshkin (2001), it relies on the quasi-steady approximation that any eigenmode instabilities must develop on a time scale much faster than that of the underlying laminar flow. Relaxing this assumption is the primary goal of Chapter 8, which quantifies the competing effects of growing eigenmodes within a decaying laminar flow. Chapter 8 also generalises the results of Chapter 7 by adapting the transient stability analysis (TSA) outlined in §1.4.3 to the present case of an unsteady laminar flow. In this manner we are able to identify transient pseudomodes of the flow, and to quantify their cumulative growth factors. Since the underlying laminar flow is itself a transient phenomenon, the analysis is 'smooth' in the sense that we drop the usual rigid distinction between eigenmodes and pseudomodes. In particular, there is no reason to restrict the transient analysis to nominally sub-critical Reynolds numbers (as is usually the case in TSA).

Our core research is summarized by Jewell and Denier (2006). It was during the course of this work that Zhao, Ghidaoui and Kolyshkin (2004) published their own pseudomode analysis for the laminar flow in a blocked pipe. Their analysis, however, is somewhat limited in scope, and in any case is signficantly compromised by reliance on the quasi-steady approximation. More recently, the quasi-steady approximation was relaxed by Zhao, Ghidaoui and Kolyshkin (2007). This latter study is, however, very narrow in scope; and even this limited data set appears to be inconsistent. We defer a more thorough discussion of these two papers to §8.3.2.

Chapter 9 comprises the final component of our research. Whereas Chapters 6–8 focus on an arbitrary upstream location of the pipe, Chapter 9 focusses on the immediate physical vicinity of the blockage. The corresponding flow is fully two-dimensional, being of the form $u(t, x, r)$ where $x = 0$ corresponds to the blockage location, and exhibits a prominent corner-like boundary layer at the intersection between the side- and end-walls of the pipe. We undertake a direct numerical simulation of this flow, from the formation of a corner boundary layer through to mid-phase vortex development and ultimate exponential decay to a rest state.

Chapter 2

The laminar flow in an internal corner

2.1 Introduction

In this chapter we compute the laminar non-pressure-driven (ZPG) flow in an internal square corner. As discussed in §§1.1 and 1.3, this problem has been tackled by a number of authors. Nevertheless, there are several compelling reasons for us to contribute our own study. Firstly, we consider it worthwhile to conduct a systematic literature review of the analytic and computational tools applied to this problem, and of the respective numerical results. Secondly, we will require accurate laminar-flow data for this flow prior to assessing its hydrodynamic stability in Chapter 3. Thirdly, we view this ZPG laminar flow as a valuable benchmark problem for external, oblique and pressure-driven corner flows.

We begin in §2.2 by deriving the canonical form of the quasi-steady Navier–Stokes equations which govern this flow; these comprise four coupled nonlinear partial differential equations in the similarity variables (η, ζ). The corresponding boundary conditions comprise *physical* conditions at the walls, *symmetry* conditions across the corner bisector, and *asymptotic* conditions at the far-field computational boundary. Since the asymptotic conditions are highly non-trivial, it is expedient to discuss them in §2.3 in conjunction with numerical solution schemes. Our own numerical method is presented in §2.3.6 following discussion in §§2.3.1 to 2.3.5 of the methods used by Rubin and Grossman (1971), Ghia (1975), Balachandar and Malik (1995), Dhanak and Duck (1997), and Parker and Balachandar (1999). Finally, in §2.4 we present our numerical results and compare our findings with those of previous researchers.

2.2 Governing equations

We formulate the governing equations in the conventional manner. As outlined in §1.3, we non-dimensionalise the flow with respect to the constant free-stream velocity $\mathbf{u}_\infty = (U^*, 0, 0)$ and an arbitrary reference length L^*, thereby defining non-dimensional coordinates (x, y, z) and velocities (u, v, w). We align the streamwise flow with the positive x-axis, and place the quarter-infinite corner walls at $y = 0$ and $z = 0$. Next, to facilitate resolution of the corner and wall boundary layers, we define similarity-type field variables η and ζ by

$$\eta \;=\; \frac{Re^{\frac{1}{2}}y}{\sqrt{2x}} \qquad \text{and} \qquad \zeta \;=\; \frac{Re^{\frac{1}{2}}z}{\sqrt{2x}}, \tag{2.1}$$

and seek solutions of the form

$$u \;=\; U(\eta,\zeta) \;+\; O(Re^{-\frac{1}{2}}), \tag{2.2a}$$

$$v \;=\; \frac{Re^{-\frac{1}{2}}}{\sqrt{2x}}\,V(\eta,\zeta) \;+\; O(Re^{-1}), \tag{2.2b}$$

$$w \;=\; \frac{Re^{-\frac{1}{2}}}{\sqrt{2x}}\,W(\eta,\zeta) \;+\; O(Re^{-1}), \tag{2.2c}$$

$$p \;=\; Re^{-\frac{1}{2}}P_1(x) \;+\; Re^{-1}P_2(x,\eta,\zeta) \;+\; O(Re^{-\frac{3}{2}}). \tag{2.2d}$$

The first pressure term corresponds to a weak streamwise pressure gradient arising from viscous wall shear, while the second term corresponds to an $O(Re^{-\frac{1}{2}})$ pressure gradient arising within the boundary layers.

The steady Navier–Stokes equations are

$$uu_x + vu_y + wu_z \;=\; -p_x + Re^{-1}\nabla^2 u, \tag{2.3a}$$

$$uv_x + vv_y + wv_z \;=\; -p_y + Re^{-1}\nabla^2 v, \tag{2.3b}$$

$$uw_x + vw_y + ww_z \;=\; -p_z + Re^{-1}\nabla^2 w, \tag{2.3c}$$

$$u_x + v_y + w_z \;=\; 0, \tag{2.3d}$$

$$\text{where} \qquad \nabla^2 \;\equiv\; \frac{\partial^2}{\partial x^2} + \frac{\partial^2}{\partial y^2} + \frac{\partial^2}{\partial z^2}\,. \tag{2.3e}$$

Substituting (2.2) into (2.3), and noting that

$$\frac{\mathrm{d}}{\mathrm{d}x} \;\equiv\; \frac{\partial}{\partial x} - \frac{1}{2x}\left(\eta\frac{\partial}{\partial\eta} + \zeta\frac{\partial}{\partial\zeta}\right),$$

we obtain

$$\nabla^2 U + (\eta U - V)U_\eta + (\zeta U - W)U_\zeta = 0, \tag{2.4a}$$

$$\nabla^2 V + (V + \eta V_\eta + \zeta V_\zeta)U - (VV_\eta + WV_\zeta) = 2x(P_2)_\eta, \tag{2.4b}$$

$$\nabla^2 W + (W + \eta W_\eta + \zeta W_\zeta)U - (VW_\eta + WW_\zeta) = 2x(P_2)_\zeta, \tag{2.4c}$$

$$V_\eta + W_\zeta = \eta U_\eta + \zeta U_\zeta \tag{2.4d}$$

$$\text{where} \qquad \nabla^2 \equiv \frac{\partial^2}{\partial \eta^2} + \frac{\partial^2}{\partial \zeta^2}\,. \tag{2.4e}$$

The canonical forms of the secondary or transverse velocities are

$$V = \eta U - \phi, \tag{2.5a}$$

$$W = \zeta U - \psi, \tag{2.5b}$$

and the corresponding governing equations are

$$\nabla^2 U + \phi U_\eta + \psi U_\zeta = 0, \tag{2.6a}$$

$$\nabla^2 \phi + \phi\phi_\eta + \psi\phi_\zeta = \eta U^2 - 2xRe P_{2\eta}, \tag{2.6b}$$

$$\nabla^2 \psi + \phi\psi_\eta + \psi\psi_\zeta = \zeta U^2 - 2xRe P_{2\zeta}, \tag{2.6c}$$

$$\phi_\eta + \psi_\zeta = 2U. \tag{2.6d}$$

To eliminate the unknown pressure P_2, we differentiate (2.6b) and (2.6c) by ζ and η respectively and subtract the resulting equations to yield the vorticity equation:

$$\nabla^2 \theta + (\phi\theta)_\eta + (\psi\theta)_\zeta = 2U(\zeta U_\eta - \eta U_\zeta), \tag{2.7}$$

where

$$\theta = \psi_\eta - \phi_\zeta. \tag{2.8}$$

An equivalent system of governing equations is

$$\nabla^2 U + \phi U_\eta + \psi U_\zeta = 0, \tag{2.9a}$$

$$\nabla^2 \theta + \phi\theta_\eta + \psi\theta_\zeta = 2\Omega U, \tag{2.9b}$$

$$\phi_\eta + \psi_\zeta = 2U, \tag{2.9c}$$

$$\theta = \psi_\eta - \phi_\zeta \tag{2.9d}$$

where

$$\Omega = W_\eta - V_\zeta = \zeta U_\eta - \eta U_\zeta - \theta. \tag{2.10}$$

Next, as recommended by Rubin and Grossman (1971), we replace the continuity equation (2.6d) by two equivalent elliptic equations, yielding a four-equation system

suited to iterative solution techniques:

$$\nabla^2 U + \phi U_\eta + \psi U_\zeta = 0, \tag{2.11a}$$
$$\nabla^2 \theta + \phi \theta_\eta + \psi \theta_\zeta = 2\Omega U, \tag{2.11b}$$
$$\nabla^2 \phi - 2U_\eta + \theta_\zeta = 0, \tag{2.11c}$$
$$\nabla^2 \psi - 2U_\zeta - \theta_\eta = 0. \tag{2.11d}$$

Finally, we ensure that all working flow variables are everywhere bounded. This property clearly does not hold for the variables ϕ and ψ defined by (2.5). Noting that the streamwise flow must satisfy the asymptotic properties

$$U(\eta, \zeta) \to f'(\zeta) \quad \text{as} \quad \eta \to \infty, \tag{2.12a}$$
$$U(\eta, \zeta) \to f'(\eta) \quad \text{as} \quad \zeta \to \infty, \tag{2.12b}$$

where f is the Blasius function of §1.3.1, we define bounded flow variables $\widetilde{\phi}$, $\widetilde{\psi}$ and $\widetilde{\theta}$ as follows:

$$\phi \equiv \eta f'(\zeta) + \widetilde{\phi}, \tag{2.13a}$$
$$\psi \equiv \zeta f'(\eta) + \widetilde{\psi}, \tag{2.13b}$$
$$\theta \equiv \zeta f''(\eta) - \eta f''(\zeta) + \widetilde{\theta}. \tag{2.13c}$$

The corresponding governing equations are

$$\nabla^2 U + (\widetilde{\phi} + \eta f'(\zeta)) U_\eta + (\widetilde{\psi} + \zeta f'(\eta)) U_\zeta = 0, \tag{2.14a}$$
$$\nabla^2 \widetilde{\phi} - 2U_\eta + \widetilde{\theta}_\zeta + f''(\eta) = 0, \tag{2.14b}$$
$$\nabla^2 \widetilde{\psi} - 2U_\zeta - \widetilde{\theta}_\eta + f''(\zeta) = 0, \tag{2.14c}$$
$$\nabla^2 \widetilde{\theta} + (\widetilde{\phi} + \eta f'(\zeta)) \widetilde{\theta}_\eta + (\widetilde{\psi} + \zeta f'(\eta)) \widetilde{\theta}_\zeta + 2U\widetilde{\theta} = \Theta \tag{2.14d}$$

where

$$\begin{aligned} \Theta \equiv\ & 2U[\zeta(U_\eta - f''(\eta)) - \eta(U_\zeta - f''(\zeta))] \\ & + (f''(\zeta) - \zeta f'''(\eta))\widetilde{\phi} - (f''(\eta) - \eta f'''(\zeta))\widetilde{\psi} \\ & + (\zeta f(\eta) f'''(\eta) - \eta f(\zeta) f'''(\zeta)) + \eta\zeta(f'(\eta) f'''(\zeta) - f'(\zeta) f'''(\eta)). \end{aligned} \tag{2.15}$$

We note that the vorticity equation equation has been slightly simplified using the Blasius identity $f^{(4)} + f f''' + f' f'' = 0$.

These governing equations are to be solved subject to no-slip conditions on the walls:

$$U = V = W = 0 \qquad \text{if} \qquad \eta = 0 \quad \text{or} \quad \zeta = 0. \tag{2.16}$$

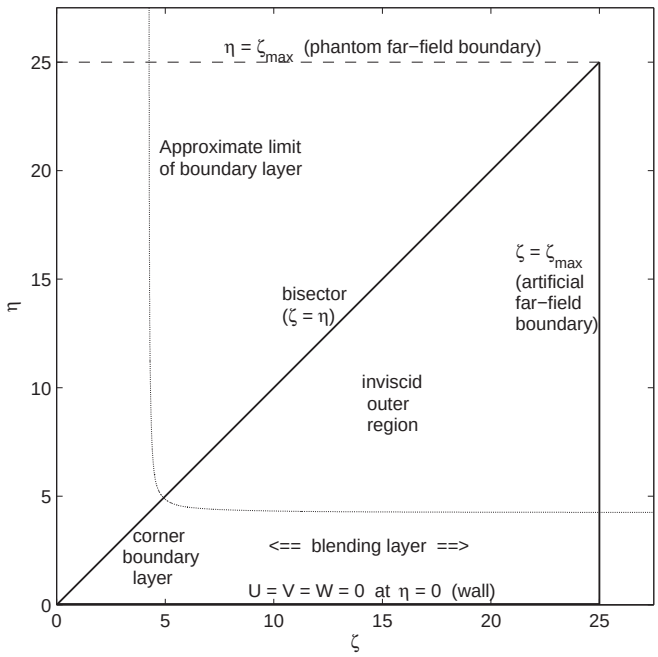

Figure 2.1: Schematic representation of the computational domain in the (η, ζ) plane, truncated to a finite size $\zeta_{\max} = 25$. If the laminar flow is assumed symmetric with respect to the corner bisector, the working computational domain reduces to the triangle bounded by $\eta = 0$, $\eta = \zeta$ and $\zeta = \zeta_{\max}$.

We assume that the flow is fully symmetric with respect to the corner bisector, ie

$$U(\zeta, \eta) = U(\eta, \zeta) \qquad \text{for all} \quad \eta, \zeta \geq 0, \tag{2.17a}$$

$$V(\zeta, \eta) = W(\eta, \zeta), \tag{2.17b}$$

$$\phi(\zeta, \eta) = \psi(\eta, \zeta), \tag{2.17c}$$

$$\Omega(\zeta, \eta) = -\Omega(\eta, \zeta), \tag{2.17d}$$

$$\theta(\zeta, \eta) = -\theta(\eta, \zeta), \tag{2.17e}$$

implying that

$$V = W, \quad \phi = \psi, \quad \Omega = \theta = 0 \qquad \text{on the bisector } \zeta = \eta. \tag{2.18}$$

Henceforth, we follow convention in focusing on the sub-diagonal half-domain defined by $0 \leq \eta \leq \zeta$. Thus, the full wall-boundary conditions are as follows:

$$U = V = W = 0 \qquad \text{and} \qquad \theta = W_\eta \qquad \text{whenever} \quad \eta = 0. \tag{2.19}$$

For computational purposes, furthermore, we will truncate the domain to a spanwise distance of $\zeta_{\max}$ from the corner line $\eta = \zeta = 0$. Thus, as illustrated by Figure 2.1,

the computational domain $\mathcal{D}$ is defined by

$$\mathcal{D} = \{(\eta, \zeta) : 0 \leq \eta \leq \zeta \leq \zeta_{\max}\} \tag{2.20}$$

where $\zeta_{\max} \gg 1$ is an arbitrary constant.

Unfortunately, it is not clear at this stage how large $\zeta_{\max}$ should be, or what boundary conditions should be applied at the artificial far-field boundary $\zeta = \zeta_{\max}$. These questions are the subject of the next section.

2.3 Numerical method

In this section we compare the numerical methods of five authors (Rubin and Grossman, 1971; Ghia, 1975; Balachandar and Malik, 1995; Dhanak and Duck, 1997; Parker and Balachandar, 1999), before presenting our own numerical method in §2.3.6. We pay especial attention to the asymptotic properties of the flow at a large distance $\rho \gg 1$ from the corner line, ie

$$\rho^2 = \eta^2 + \zeta^2, \tag{2.21}$$

and proceed to translate these properties into a set of workable boundary conditions to be applied at the artificial far-field boundary $\zeta = \zeta_{\max}$ of the computational domain $\mathcal{D}$ defined by (2.20). We commence in §2.3.1 with an in-depth review of the formal asymptotic solution of Pal and Rubin (1971) and its numerical implementation by Rubin and Grossman (1971).

2.3.1 Rubin and Grossman (1971)

2.3.1.1 Asymptotic analysis: Outline

Rubin and Grossman (1971) are credited with producing the first reliable numerical results for the laminar corner boundary layer. In reviewing their solution, we commence with the blending boundary layer adjacent to the inner corner boundary layer. In the case of the horizontal boundary layer, this region may be defined loosely in mathematical terms by

$$\eta = O(1), \qquad \zeta = O(10). \tag{2.22}$$

Three asymptotic limits will be of especial interest: $\zeta \to O(1)$ (ie transition to the inner corner region), $\zeta \to \infty$ (ie transition to a 2D boundary layer at large distances from the corner line), and $\zeta \to \eta$ (ie transition to the inviscid outer region). The blending-layer flow comprises a Blasius-style boundary layer with a superimposed

crossflow $W(\eta,\zeta)$. This is easily verified by substituting the following leading-order solution into the system (2.11) of governing equations:

$$U = f'(\eta) + o(1), \tag{2.23a}$$
$$V = \eta f'(\eta) - f(\eta) + o(1), \tag{2.23b}$$
$$W = O(1), \tag{2.23c}$$
$$\phi = f(\eta) + o(1), \tag{2.23d}$$
$$\psi = \zeta f'(\eta) + O(1), \tag{2.23e}$$
$$\theta = \zeta f''(\eta) + O(1), \tag{2.23f}$$

where f is the Blasius function. The structure of the crossflow is unknown at this stage.

Carrier (1947) hypothesized that the blending-layer flow varies rapidly (ie exponentially) as a function of spanwise distance ζ from the corner line. This was also assumed by Rubin and Grossman when they first attempted work on the corner-flow problem. Computational work, however, quickly convinced them that this hypothesis was incorrect. They demonstrated that the blending-layer flow varies algebraically in ζ, and may be represented by the following inverse power series in ζ for $\eta = O(1)$:

$$\mathbf{U}_{\rm BL} = \sum_{n=0}^{\infty} \mathbf{U}_n(\eta)\,\zeta^{-n}, \tag{2.24a}$$
$$\phi_{\rm BL} = \sum_{n=0}^{\infty} \phi_n(\eta)\,\zeta^{-n}, \tag{2.24b}$$
$$\psi_{\rm BL} = \zeta f'(\eta) + \sum_{n=0}^{\infty} \psi_n(\eta)\,\zeta^{-n}, \tag{2.24c}$$
$$\theta_{\rm BL} = \zeta f''(\eta) + \sum_{n=0}^{\infty} \theta_n(\eta)\,\zeta^{-n}. \tag{2.24d}$$

Comparison with (2.23) shows that the leading coefficients are given by

$$U_0(\eta) = f'(\eta), \tag{2.25a}$$
$$V_0(\eta) = \eta f'(\eta) - f(\eta), \tag{2.25b}$$
$$\phi_0(\eta) = f(\eta). \tag{2.25c}$$

Since the Blasius function $f(\eta)$ has the property of exponential decay out of the boundary layer[1], ie

$$f(\eta) = O\left(\exp\left[-\tfrac{1}{2}(\eta-\beta)^2\right]\right) \qquad \text{for} \qquad \eta \gg 1, \tag{2.27}$$

[1]This is derived by expressing $U_0(\eta) \equiv f'(\eta)$ in the form

$$U_0(\eta) = 1 - \epsilon(s) \qquad \text{where} \qquad s = \eta - \beta, \tag{2.26}$$

it follows that

$$(U_0, V_0, \phi_0) \;=\; (1, \beta, \eta{-}\beta) \;+\; (\text{exp. small terms}) \qquad \text{for} \qquad \eta \gg 1, \tag{2.28}$$

where the Blasius constant β is given by

$$\beta \;=\; \lim_{\eta\to\infty} (\eta f'(\eta) - f(\eta)) \;=\; 1.21678. \tag{2.29}$$

Pal and Rubin (1971) showed that the property of exponential decay holds in general for the streamwise velocity and vorticity, but does not hold for the secondary flow. Thus, on applying the symmetry condition (2.18), we obtain the following expansion for the outer-region flow:

$$(U, \Omega, \theta)_{\text{outer}} \;=\; (1, 0, 0) \;+\; \text{e.s.t.}, \qquad \eta \gg 1, \tag{2.30a}$$

$$(V, W, \phi, \psi)_{\text{outer}} \;=\; (\beta, \beta, \eta{-}\beta, \zeta{-}\beta) \;+\; \text{a.s.t.}, \qquad \eta \gg 1, \tag{2.30b}$$

where *a.s.t.* denotes algebraically small terms. Since the outer-region flow is irrotational, we may represent it by a velocity potential Φ satisfying Laplace's equation, ie

$$(V, W)_{\text{outer}} \;=\; (\Phi_\eta, \Phi_\zeta) \tag{2.31}$$

where

$$\nabla^2\Phi \;\equiv\; \Phi_{\eta\eta} + \Phi_{\zeta\zeta} \;=\; 0, \tag{2.32}$$

or equivalently, by the power series

$$(W - \mathrm{i}V)_{\text{outer}} \;=\; \sum_{n=0}^{\infty} c_n (\zeta + \mathrm{i}\eta)^{-n} \tag{2.33}$$

where the complex-valued coefficients $\{c_n\}$ are independent of the spatial coordinates[2]. The solution is therefore of the form

$$\Phi \;=\; \beta(\eta + \zeta) \;+\; \Theta_0 \log\rho \;+\; \sum_{n=1}^{\infty} \Theta_n(\alpha)\, \rho^{-n}\,, \tag{2.34a}$$

$$V_{\text{outer}} \;=\; \beta \;+\; \sum_{n=1}^{\infty} \frac{a_n \sin n\alpha \;-\; b_n \cos n\alpha}{\rho^n}\,, \tag{2.34b}$$

$$W_{\text{outer}} \;=\; \beta \;+\; \sum_{n=1}^{\infty} \frac{a_n \cos n\alpha \;+\; b_n \sin n\alpha}{\rho^n}\,, \tag{2.34c}$$

---

and substituting (2.26) into the Blasius differential equation (1.8) to obtain

$$\epsilon'' \approx -s\epsilon', \quad \epsilon \to 0 \quad \text{for} \quad s \gg 1.$$

Now integrate with respect to s to obtain the desired result.

[2]For the case $n \geq 5$, these coefficients are actually logarithmic functions of η and ζ. Consequently, the high-order blending-layer coefficients in (2.24) also become functions of ζ. We neglect this detail, however, as it is of no practical significance.

where

$$c_n \equiv a_n + \mathrm{i}b_n \qquad (a_n,\, b_n \,\text{real}), \tag{2.35}$$

and the polar coordinates (ρ, α) are defined by

$$\zeta = \rho\cos\alpha, \qquad \eta = \rho\sin\alpha, \qquad \rho^2 = \eta^2 + \zeta^2. \tag{2.36}$$

In these coordinates the symmetry condition (2.18) transforms to

$$W_{\text{outer}}\left(\rho,\, \frac{\pi}{4} + \alpha\right) = V_{\text{outer}}\left(\rho,\, \frac{\pi}{4} - \alpha\right), \tag{2.37}$$

implying that

$$c_n = |c_n|\, e^{\mathrm{i}\pi(n-1)/4} \qquad \text{for} \qquad n = 0, 1, 2, \ldots . \tag{2.38}$$

In particular,

$$b_1 = 0 \qquad \text{and} \qquad b_2 = a_2. \tag{2.39}$$

Thus, by applying the identities

$$\begin{aligned} \cos\alpha &= \zeta/\rho, \\ \sin\alpha &= \eta/\rho, \\ \cos 2\alpha &= (\eta^2 - \zeta^2)/\rho^2, \\ \sin 2\alpha &= (2\eta\zeta)/\rho^2, \end{aligned}$$

we obtain

$$V_{\text{outer}} = \beta + a_1\left[\frac{\eta}{\eta^2+\zeta^2}\right] + a_2\left[\frac{\zeta^2 + 2\eta\zeta - \eta^2}{(\eta^2+\zeta^2)^2}\right] + O\left(\rho^{-3}\right), \tag{2.40a}$$

$$W_{\text{outer}} = \beta + a_1\left[\frac{\zeta}{\eta^2+\zeta^2}\right] + a_2\left[\frac{\eta^2 + 2\eta\zeta - \zeta^2}{(\eta^2+\zeta^2)^2}\right] + O\left(\rho^{-3}\right). \tag{2.40b}$$

To determine the unknown coefficients a_1 and a_2, we first examine the behaviour of the outer-region expansion (2.40) on exiting the outer region and entering the blending layer. For the case $\eta \ll \zeta$, this expansion has the asymptotic form

$$V_{\text{outer}} = V^* \equiv \beta + (a_1\eta + a_2)\zeta^{-2} + O\left(\zeta^{-3}\right) \qquad \text{for} \quad \eta \ll \zeta, \tag{2.41a}$$

$$W_{\text{outer}} = W^* \equiv \beta + a_1\zeta^{-1} - a_2\zeta^{-2} + O\left(\zeta^{-3}\right) \qquad \text{for} \quad \eta \ll \zeta. \tag{2.41b}$$

We will see in §2.3.1.2 that this asymptotic form is consistent with the blending-layer expansion (2.24). Thus, the process of asymptotic matching permits easy identification of a_1 and a_2.

Finally, for computational purposes, Rubin and Grossman (1971) offered the following composite expansion for the secondary flow, valid for all $\eta \le \zeta$:

$$(V, W)_{\text{comp}} = (V, W)_{\text{BL}} + (V, W)_{\text{outer}} - (V^*, W^*). \tag{2.42}$$

This single expansion clearly reduces to $(V,W)_{\rm BL}$ in the blending layer, and to $(V,W)_{\rm outer}$ in the outer region. Indeed, Rubin and Grossman (1971) explicitly evaluated this formula at $\zeta = \zeta_{\max} = 15$, the far-field boundary of their computational domain.

2.3.1.2 Asymptotic analysis: Details

In this section we complete the asymptotic analysis of §2.3.1.1 for the laminar flow far from the corner line ($\zeta \gg 1$). First, we compute the leading coefficients $\{\mathbf{U}_n(\eta)\}$ in the asymptotic expansion (2.24) for the blending-layer flow. This completes the analysis of the streamwise velocity and vorticity. We then complete the analysis of the secondary flow by determining the (scalar) coefficients in the outer-region expansion (2.40) and the composite expansion (2.42).

On substituting (2.24) and (2.25) into the governing equations (2.11), we obtain

$$\begin{aligned}
\phi_1' &= 2U_1, && \text{(2.43a)}\\
U_1'' + f''\phi_1 + fU_1' - f'U_1 &= 0, && \text{(2.43b)}\\
\theta_0'' + f\theta_0' + f'''\phi_1 + f''\psi_0 + 2f'(\theta_0 - U_1') &= 0, && \text{(2.43c)}\\
\theta_0 &= \psi_0', && \text{(2.43d)}
\end{aligned}$$

where the primes denote differentiation with respect to η. Thus, the leading component W_0 of the crossflow is algebraically coupled with the second-order terms U_1 and V_1. More generally, we find that W_n is coupled with $(U,V)_{n+1}$ for all $n \geq 0$.

The first two equations in (2.43) decouple to yield

$$\begin{aligned}
\phi_1''' + f\phi_1'' - f'\phi_1' + 2f''\phi_1 &= 0,\\
U_1 &= \tfrac{1}{2}\phi_1',
\end{aligned}$$

which must be solved subject to the following three boundary conditions:

$$\begin{aligned}
\phi_1(0) &= 0 && \text{(no-slip condition on } V),\\
\phi_1'(0) &= 0 && \text{(no-slip condition on } U),\\
\phi_1' \to 0 \quad &\text{as} \quad \eta \to \infty && \text{(from (2.30a)).}
\end{aligned}$$

The solution is clearly given by

$$U_1 = 0, \qquad \phi_1 = 0. \tag{2.44}$$

Thus,

$$(U,V)_{\rm BL} = (U_0,\, V_0) + O(\zeta^{-2}) \qquad \text{for} \qquad \zeta \gg 1. \tag{2.45}$$

The remaining two equations in (2.43) now decouple to yield

$$(\psi_0' + f\psi_0)'' = 0 \qquad \text{and} \qquad \theta_0 = \psi_0', \tag{2.46}$$

which must be solved subject to

$$\begin{aligned} &\psi_0(0) = 0, && \text{(no-slip condition on } W\text{)}, \\ &\psi_0 \approx -\beta \quad \text{for} \quad \eta \gg 1 && \text{(from (2.30b))}. \end{aligned}$$

This yields the following first-order differential equation:

$$\psi_0' + f\psi_0 = -\beta(\eta - \beta), \qquad \text{subject to} \qquad \psi_0(0) = 0. \tag{2.47}$$

The solution is

$$\psi_0(\eta) = -\beta g(\eta), \tag{2.48a}$$
$$\theta_0(\eta) = -\beta g'(\eta), \tag{2.48b}$$
$$W_0(\eta) = \beta g(\eta), \tag{2.48c}$$

where g satisfies the differential equation

$$g' + fg = \eta - \beta, \qquad \text{subject to} \qquad g(0) = 0. \tag{2.49}$$

This auxiliary function has the analytic form

$$g(\eta) = \int_0^\eta \frac{(s-\beta)f''(\eta)}{f''(s)}\,\mathrm{d}s. \tag{2.50}$$

However, we prefer to solve (2.49) numerically.

The second-order correction terms $\{U_2, V_2, W_1\}$ are governed by the following equations:

$$U_2'' + fU_2' - 2f'U_2 = -f''\phi_2\,, \tag{2.51a}$$
$$\phi_2' = 2U_2 + \psi_1\,, \tag{2.51b}$$
$$\theta_1 = \psi_1'\,, \tag{2.51c}$$
$$\psi_1''' + f\psi_1'' + f'\psi_1' + f''\psi_1 = 2f'U_2' + \eta f''\phi_2. \tag{2.51d}$$

The solution is

$$U_2(\eta) = -\kappa(\eta f''), \tag{2.52a}$$
$$\phi_2(\eta) = -\kappa(3\eta f' + f), \tag{2.52b}$$
$$\psi_1(\eta) = -\kappa(4f' + \eta f''), \tag{2.52c}$$
$$\theta_1(\eta) = -\kappa(5 - \eta f)f'', \tag{2.52d}$$
$$V_2(\eta) = \kappa(f + 3\eta f' - \eta^2 f''), \tag{2.52e}$$
$$W_1(\eta) = \kappa(4f'), \tag{2.52f}$$

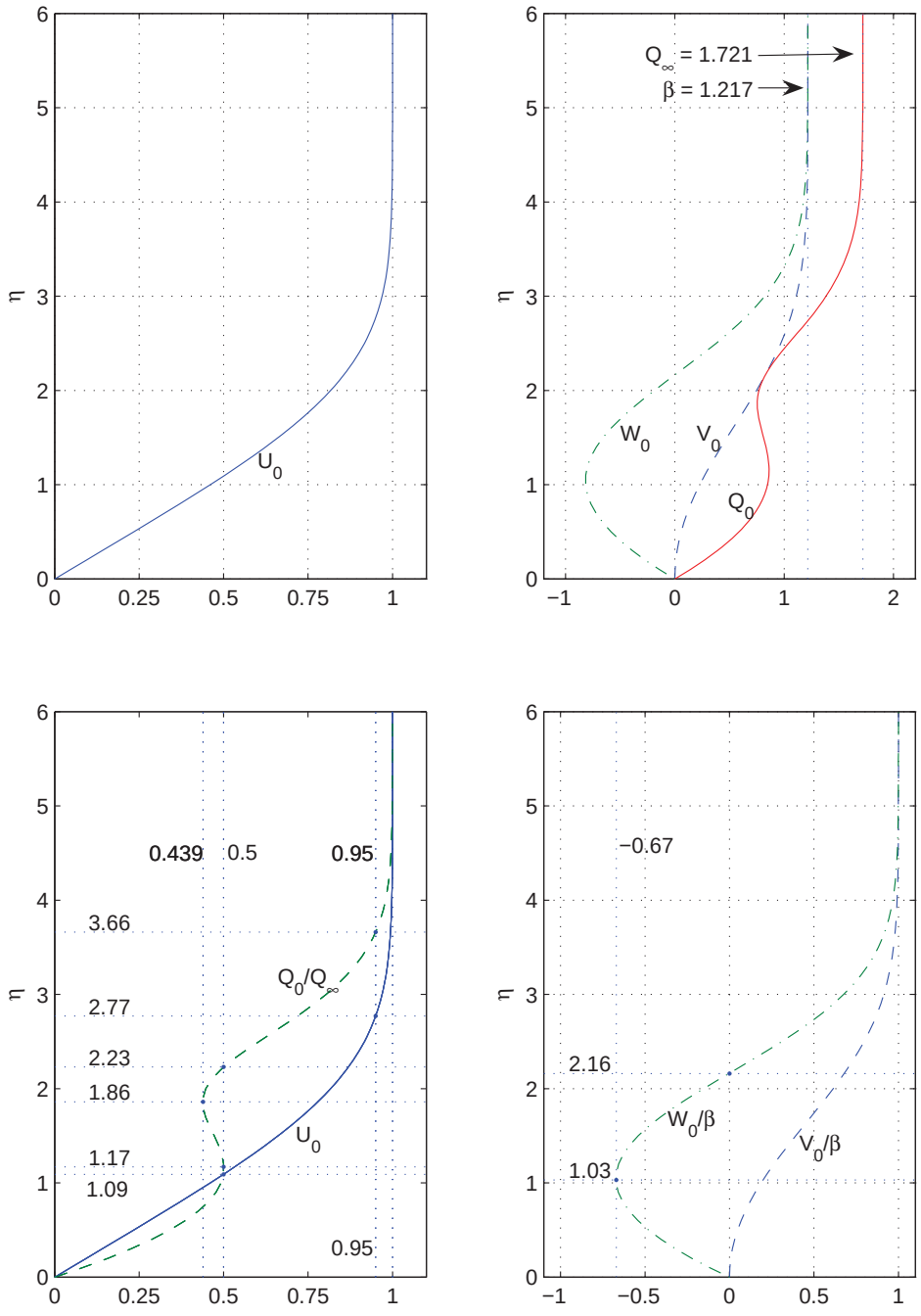

Figure 2.2: The leading-order structure (U_0, V_0, W_0) of the flow within the blending boundary layer for $\eta = O(1)$, $\zeta \gg 1$. *Upper left:* Streamwise velocity U_0 (equivalent to Blasius flow). *Upper right:* Secondary velocity (V_0, W_0, Q_0), where $Q^2 = V^2 + W^2$. *Lower left:* Streamwise velocity U_0 *(solid curve)* and secondary velocity Q_0 *(dashed curve)* rescaled by $Q_\infty = \sqrt{2}\beta = 1.721$. *Lower right:* Secondary velocity (V_0, W_0) rescaled by $\beta = 1.217$.

where κ is an unknown constant[3]. Likewise, the third-order correction terms are of the form

$$\psi_2(\eta) \;=\; -\beta\kappa\, h(\eta), \tag{2.53a}$$
$$\theta_2(\eta) \;=\; -\beta\kappa\, h'(\eta), \tag{2.53b}$$
$$W_2(\eta) \;=\; \beta\kappa\, g_2(\eta), \tag{2.53c}$$
$$U_3(\eta) \;=\; \beta\kappa(g_2(\eta) - h(\eta)), \tag{2.53d}$$

where

$$g_2(0) = h(0) = 0, \tag{2.54a}$$
$$g_2(\eta) \to 1, \quad h(\eta) \to 1 \qquad \text{as} \quad \eta \to \infty. \tag{2.54b}$$

For details, we the reader to Appendix I of Rubin and Grossman (1971)[4].

In accordance with (2.30a), the coefficients θ_1, U_2 and θ_2 all exhibit exponential decay out of the blending layer. For the secondary velocity, however, we find that

$$V_{\rm BL} \;=\; \beta \,+\, \kappa(4\eta - \beta)\zeta^{-2} \,+\, O(\zeta^{-3}) \qquad \text{for} \quad \zeta \gg \eta \gg 1, \tag{2.55a}$$
$$W_{\rm BL} \;=\; \beta \,+\, 4\kappa\zeta^{-1} \,+\, (\beta\kappa)\zeta^{-2} \,+\, O(\zeta^{-3}) \qquad \text{for} \quad \zeta \gg \eta \gg 1. \tag{2.55b}$$

By equating (2.55) with (2.41), we obtain the first two coefficients of the outer-region expansion (2.40):

$$a_1 \;=\; 4\kappa, \qquad a_2 \;=\; -\kappa. \tag{2.56}$$

The full composite asymptotic expression is therefore as follows. The far-field streamwise velocity is given by

$$U_{\rm comp} \;=\; f'(\eta) \;-\; \kappa(\eta f'')\,\zeta^{-2} \,+\, O\left(\zeta^{-3}\right), \tag{2.57}$$

the secondary (outflow) velocity $V = \eta U - \phi$ is given by

$$\begin{aligned} \phi_{\rm comp} \;=\; & f(\eta) \,+\, \kappa\left[4\eta - (f + 3\eta f' + \beta)\right]\zeta^{-2} \\ & -\, \frac{4\kappa\eta}{\eta^2 + \zeta^2} \,+\, \frac{\kappa\beta(\zeta^2 + 2\eta\zeta - \eta^2)}{(\eta^2 + \zeta^2)^2} \,+\, O\left(\zeta^{-3},\, \rho^{-3}\right), \end{aligned} \tag{2.58}$$

the secondary (crossflow) velocity $W = \zeta U - \psi$ is given by

$$\begin{aligned} \psi_{\rm comp} \;=\; & \zeta f'(\eta) - \beta g(\eta) \,+\, \kappa[\,4(1 - f') - \eta f'']\,\zeta^{-1} \,+\, \kappa\beta(1 - h)\,\zeta^{-2} \\ & -\, \frac{4\kappa\zeta}{\eta^2 + \zeta^2} \,+\, \frac{\kappa\beta(\eta^2 + 2\eta\zeta - \zeta^2)}{(\eta^2 + \zeta^2)^2} \,+\, O\left(\zeta^{-3},\, \rho^{-3}\right), \end{aligned} \tag{2.59}$$

[3]This constant corresponds to $-\chi$ in the notation of Rubin and Grossman (1971).

[4]The notation of Rubin and Grossman (1971) here is slightly different to ours. In particular, our function g_2 corresponds in their notation to $(2h - l')$, where the functions h, l and l' are tabulated in Table I.1 of their paper.

and the vorticity $\Omega = \zeta U_\eta - \eta U_\zeta - \theta$ is given by

$$\theta_{\text{comp}} \;=\; \zeta f''(\eta) - \beta g'(\eta) \;-\; \kappa(5f'' + \eta f''')\,\zeta^{-1} \;+\; \beta\kappa h'(\eta)\,\zeta^{-2} \;+\; O\left(\zeta^{-3}\right). \quad (2.60)$$

The unknown constant κ appears in all of the decaying terms, and thus can be interpreted physically as the degree of interaction between the boundary layers of the two walls. In particular, we can interpret the crossflow W in the vicinity of the horizontal wall at $\eta = 0$ as a Blasius-type outflow from the vertical wall at $\zeta = 0$. Unfortunately, to the best of our knowledge κ is not specified by any closed-form expression or any single differential equation. Instead, Rubin and Grossman (1971) estimated it using an iterative procedure (discussed in their paper at some length), obtaining

$$\kappa \;=\; 2.5 \quad \text{(to 2 s.f.)}. \quad (2.61)$$

This (surprisingly large) value implies a bisector flow profile of

$$V_{\text{bis}} \;\equiv\; W_{\text{bis}} \;=\; 1.217 \;+\; 5.0\,\zeta^{-1} - 1.52\,\zeta^{-2} \qquad \text{for} \qquad \zeta \gg 1. \quad (2.62)$$

2.3.1.3 Solution method

For a full numerical solution, Rubin and Grossman (1971) discretized the governing equations (2.11) using a standard second-order finite-difference (FD2) scheme with a uniform step-size of

$$\Delta\eta \;=\; \Delta\zeta \;\equiv\; h \;=\; 0.2 \quad (2.63)$$

over a computational domain of size $\zeta_{\max} = 15$. Far-field boundary conditions were furnished by explicit evaluation of (2.57) to (2.60) for the case $\zeta = \zeta_{\max}$. The discretised system has approximately $2N^2$ unknowns, where

$$\zeta_{\max} \;=\; Nh. \quad (2.64)$$

The working flow variables were initialized to the values specified in (3.4) of their paper, and the system solved using following iterative algorithm:

. For each estimate of κ,
. For each iteration m,
. For each $\eta_i \equiv ih$, $i = 1, ..., N-1$,
. For each $\zeta_j \equiv jh$, $j = i, ..., N-1$,
. – Update U_{ij}, and record the relative change $U_{ij}^{m-1} \to U_{ij}^{m}$.
. – Repeat for ϕ_{ij}, ψ_{ij} and θ_{ij}.

The authors employed the (somewhat generous) convergence criterion that no flow variable should change by more than 1% in the final round of iteration. This was generally attained after a few thousand iterations for each κ estimate.

2.3.2 Ghia (1975)

Ghia (1975) cross-checked the work of Rubin and Grossman (1971) by circumventing the asymptotic analysis of §2.3.1. To do this, he first mapped the entire quarter-infinite domain to the unit square as follows:

$$\{(\eta,\zeta):\ 0\le\eta,\zeta\le\infty\} \quad\Rightarrow\quad \{(\widetilde{\eta},\widetilde{\zeta}):\ 0\le\widetilde{\eta},\widetilde{\zeta}\le 1\} \tag{2.65a}$$

$$\text{or}\qquad \{(\eta,\zeta):\ 0\le\eta\le\zeta\le\infty\} \quad\Rightarrow\quad \{(\widetilde{\eta},\widetilde{\zeta}):\ 0\le\widetilde{\eta}\le\widetilde{\zeta}\le 1\}. \tag{2.65b}$$

In the transformed coordinates $(\widetilde{\eta},\widetilde{\zeta})$, the far-field boundary conditions reduce to

$$(U,\phi,\psi,\theta)\ =\ (U_0(\eta),\ \phi_0(\eta),\ \psi_0(\eta),\ \theta_0(\eta)) \qquad \text{at}\quad \widetilde{\zeta}=1. \tag{2.66}$$

In order to capture the slow algebraic development of the flow in the spanwise direction, Ghia selected the coordinate mapping

$$\widetilde{\eta}\ =\ \sigma(\eta)\ \equiv\ \eta/(\mu+\eta) \qquad \text{where} \qquad \mu=5.0, \tag{2.67a}$$

$$\widetilde{\zeta}\ =\ \sigma(\zeta)\ \equiv\ \zeta/(\mu+\zeta), \tag{2.67b}$$

which has the metric

$$\frac{\mathrm{d}\zeta}{\mathrm{d}\widetilde{\zeta}}\ =\ \mu\left(1+\frac{\zeta}{\kappa}\right)^2 \tag{2.68}$$

and the asymptotic property

$$\zeta\ =\ O\left(\epsilon^{-1}\right) \qquad \text{whenever} \qquad \epsilon\ \equiv\ 1-\widetilde{\zeta}\ \ll\ 1. \tag{2.69}$$

Ghia discretised the governing equations over the computational domain (2.65b) using a FD2 scheme with a uniform step-size of

$$\Delta\eta\ =\ \Delta\zeta\ \equiv\ \widetilde{h}\ =\ 0.02, \tag{2.70}$$

which corresponds to a variable physical step-size of $\Delta\eta\approx 0.1$ at the wall, $\Delta y\approx 0.2$ in mid-layer (ie $\eta\approx 2$), $\Delta\zeta\approx 0.4$ for $\zeta\approx 5$, and $\Delta\zeta\approx 0.9$ at $\zeta\approx 10$. Thus, the discretised system had approximately $2N^2$ unknowns where $N=50$.

The discretised equations were solved iteratively using the Alternating Direction Implicit (ADI) scheme. To accelerate numerical convergence, Ghia varied the size of the artificial time-step over the course of the iterative algorithm. His convergence criterion was similar to that of Rubin and Grossman (1971), namely that no flow variable should vary by more than 1% between successive sweeps of the ADI routine. This criterion was attained after a few hundred iterations, compared with a few thousand iterations for the solution algorithm of Rubin and Grossman (1971).

2.3.3 Balachandar and Malik (1995)

Balachandar and Malik (1995) discretised the governing equations using a Chebyshev pseudospectral scheme over the (η, ζ) plane with far-field domain boundary $\zeta_{\max} = 25$. The spectral scheme was of order $N \times N$ where $N = 84$. In other words, at each ζ station the η coordinate was discretised using N+1 = 85 Chebyshev-spaced collocation points (including the two boundary points $\eta = 0$ and $\eta = \zeta_{\max}$), and all derivatives with respect to η were computed using order-N polynomial interpolation of function values. (The ζ coordinate was discretised in similar fashion.) One consequence of the Chebyshev spectral scheme is that the collocation points are clustered near the domain boundaries. This feature is clearly welcome near the wall, ie within the blending layer and the corner region proper ($\eta = O(1)$ or $\zeta = O(1)$). The clustering near the far-field boundary $\zeta = \zeta_{\max}$ is less welcome, but is essential for numerical stability.

Like Rubin and Grossman (1971) and Ghia (1975), Balachandar and Malik (1995) assumed flow symmetry with respect to the corner bisector, thereby obtaining a discretised system with approximately $2N^2$ unknowns. However, they differed from earlier authors in their treatment of the far-field boundary $\zeta = \zeta_{\max}$. In particular, they dispensed with the outer-region expansion (2.40) and the composite expansion (2.57)–(2.60) of Rubin and Grossman (1971), but chose to retain the full blending-layer expansion derived by Rubin and Grossman (1971)[5], ie

$$U(\eta, \zeta_{\max}) = \sum_{n=0}^{3} U_n(\eta)\, \zeta_{\max}^{-n} \qquad (\text{where} \quad U_1 = 0), \tag{2.71a}$$

$$\phi(\eta, \zeta_{\max}) = \sum_{n=0}^{3} \phi_n(\eta)\, \zeta_{\max}^{-n} \qquad (\text{where} \quad \phi_1 = 0), \tag{2.71b}$$

$$\psi(\eta, \zeta_{\max}) = \zeta_{\max} f'(\eta) + \sum_{n=0}^{2} \psi_n(\eta)\, \zeta_{\max}^{-n}, \tag{2.71c}$$

$$\theta(\eta, \zeta_{\max}) = \zeta_{\max} f''(\eta) + \sum_{n=0}^{2} \theta_n(\eta)\, \zeta_{\max}^{-n}. \tag{2.71d}$$

These boundary conditions were implemented along the full length of the domain boundary, ie for all η satisfying $0 < \eta < \zeta_{\max}$.

The authors provide few details of their solution algorithm, merely reporting that

[5]Balachandar and Malik (1995) also retained the third-order correction terms U_3 and ϕ_3 (which Rubin and Grossman (1971) computed but did not use). Incidentally, their paper does not mention the unknown constant κ from §2.3.1.2 (which scales all of the decaying terms in the asymptotic expansions). It would appear, therefore, that the authors simply adopted the estimate $\kappa \approx 2.5$ originally derived by Rubin and Grossman (1971) using a trial-and-error process.

"[r]esults obtained from this technique compare favourably with those of Rubin and Grossman (1971) and Ghia (1975)."

2.3.4 Dhanak and Duck (1997)

Like Ghia (1975), Dhanak and Duck (1997) discarded the non-decaying terms in the asymptotic analysis of Rubin and Grossman (1971). Whereas Ghia placed his far-field boundary at 'true infinity' ($\zeta_{\max} = \infty$), Dhanak and Duck used a large but finite computational domain ($\zeta_{\max} = 60$) and applied the following far-field boundary conditions:

$$U = U_0(\eta) = f'(\eta) \qquad \text{at} \qquad \zeta = \zeta_{\max}, \tag{2.72a}$$

$$\phi = \phi_0(\eta) = f(\eta) \qquad \text{at} \qquad \zeta = \zeta_{\max}, \tag{2.72b}$$

$$\frac{\partial}{\partial \zeta}\left[\zeta\,\widetilde{\psi}\right] = \psi_0(\eta) \qquad \text{at} \qquad \zeta = \zeta_{\max}, \tag{2.72c}$$

$$\frac{\partial}{\partial \zeta}\left[\zeta\,\widetilde{\theta}\right] = \theta_0(\eta) \qquad \text{at} \qquad \zeta = \zeta_{\max}. \tag{2.72d}$$

As previously noted, the blending-layer flow takes the asymptotic form

$$U_{\mathrm{BL}} = U_0(\eta) + O\left(\zeta^{-2}\right), \tag{2.73a}$$

$$\phi_{\mathrm{BL}} = \phi_0(\eta) + O\left(\zeta^{-2}\right), \tag{2.73b}$$

$$\widetilde{\psi}_{\mathrm{BL}} = \psi_0(\eta) + O\left(\zeta^{-1}\right), \tag{2.73c}$$

$$\widetilde{\theta}_{\mathrm{BL}} = \theta_0(\eta) + O\left(\zeta^{-1}\right). \tag{2.73d}$$

Thus, the boundary conditions (2.72a) and (2.72b) for U and V respectively introduce truncation errors of magnitude $O(\zeta_{\max}^{-2})$. Dhanak and Duck hoped to achieve similar truncation errors for W and Ω by applying the derivative-based boundary conditions (2.72c) and (2.72d) rather than the leading-order conditions

$$\widetilde{\psi} = \psi_0(\eta), \qquad \theta = \theta_0(\eta).$$

The boundary conditions (2.72) were implemented along the full length of the domain boundary, ie for all η satisfying $0 < \eta < \zeta_{\max}$; no attempt was made to distinguish between the blending layer and the outer region. The governing equations were discretised using a FD2 scheme with step-size $h = 0.1$, yielding a system of order $N = 600$ (compared with $N = 75$ for Rubin and Grossman (1971) and $N = 50$ for Ghia (1975)). The discretized equations were solved iteratively using a 'line relaxation' scheme (not discussed in any detail, but most likely similar to the ADI method of Ghia). Dhanak and Duck (1997) used a much stricter convergence criterion than that of Rubin and Grossman (1971) or Ghia (1975):

> It is worth mentioning that the convergence of the iterative scheme was often very slow, and although the difference between computed quantities between successive iterations may have been small, the change in the differences was very small; consequently our computations routinely took tens of thousands of iterations with stringent convergence criteria imposed (typically when the maximum change of any of the computed values was less than 10^{-7}). It may well be that very slow convergence of iteration schemes was partly responsible for the diverse 'scatter' of previously published results. A second possible cause is that we found the treatment of boundary conditions as $\zeta \to \infty$ required some care; in particular the neglect of the $O(\zeta^{-1})$ terms in [the boundary conditions] led to significant numerical errors at reasonable values of $\zeta_{\max}$. However, the conditions (4.16), (4.17) [*(2.72) in our notation*] were found to give good domain convergence.

Interestingly, the authors describe the present ZPG corner flow as "more challenging" than any pressure-driven flow of Falkner–Skan type (§1.3.6).

2.3.5 Parker and Balachandar (1999)

Parker and Balachandar (1999) followed Balachandar and Malik (1995) in their use of pseudospectral discretization, but differed radically in their treatment of asymptotic boundary conditions. Their far-field domain boundary was accurate only to leading order, ie

$$(U, \phi, \psi, \theta) \;=\; (U_0(\eta),\, \phi_0(\eta),\, \psi_0(\eta),\, \theta_0(\eta)) \qquad \text{at} \qquad \zeta = \zeta_{\max}. \tag{2.74}$$

Following extensive testing for domain convergence (documented in §2.3 of their paper), they settled on parameter values of $\zeta_{\max} = 40$ and spectral order $N = 104$ for the case of non-pressure-driven laminar flow. For solution of the nonlinear governing equations, Parker and Balachandar devised a highly efficient iteration based on the Generalized Minimum Residual (GMRES) algorithm (see, for example, §1.4 of Deuflhard (2004)). For further efficiency gains, the solution algorithm is first applied using a low-order spectral discretization (ie $N = N_1 \ll 104$). The converged solution at N_1 is then interpolated to a finer grid of order $N_2 > N_1$, thereby furnishing 'initial conditions' to a second round of iteration. This process is repeated using successively larger values of N, and the authors report that "[a]t each grid resolution, five to ten iterations of Newton's method reduces the integrated residual to well below 10^{-7}." To avoid any loss of accuracy, all interpolation was conducted using the spectrally-accurate barycentric method.

2.3.6 Our method

Most, perhaps all, of the above-mentioned numerical schemes are either difficult to program or of questionable accuracy. Yet the results of the respective schemes are actually in good qualitative agreement. We therefore decided to adopt the method of Dhanak and Duck (1997) as outlined in §2.3.4. Relatively easy to implement, this method shifts some of the burden from the analyst to the computer. In particular, explicit calculation of high-order asymptotic terms is avoided with the aid of a large computational domain ($\zeta_{\max} \geq 50$) coupled with the far-field boundary conditions (2.72). The governing equations (2.14) are discretised using a second-order finite-difference scheme with step-size $h = 0.1$, following implementation of the symmetry conditions (2.18), the wall conditions (2.19), and the far-field boundary conditions (2.72). The resulting nonlinear system is to be solved iteratively using line relaxation in the η and ζ coordinates. We wrote our own Fortran 90 code to implement this scheme.

Unfortunately, the numerical scheme proved to be violently unstable. This instability arises from the large-valued coefficients ψ and ϕ of the nonlinear advective terms of the governing equations, and imposes an upper limit of

$$h\zeta_{\max} \lesssim 3. \tag{2.75}$$

This instability was found by Rubin and Grossman (1971); somewhat surprisingly, it was not reported by Dhanak and Duck (1997). Faced with this stability restriction, and reluctant to sacrifice accuracy by reducing $\zeta_{\max}$, we opted to reduce h to 0.05; this yielded $N \geq 1000$ in (2.64), implying a total of two to three million flow variables.

Unfortunately, numerical convergence for this scheme proved extremely slow. We needed at least half a million iterations, or about two weeks of computer time, to attain the convergence criterion of Dhanak and Duck (1997), namely that no flow variable should change by more than $\epsilon \approx 10^{-7}$ between successive iterations. Even then, it was difficult to ascertain whether true convergence had been attained (to three-figure accuracy, say), since the per-iteration changes in any given flow variable were found to be monotonic and cumulative. It was also difficult to assess the effectiveness of the indirect boundary conditions (2.72c,d).

We therefore set out to accelerate the iterative algorithm. A small efficiency gain (around 25%) was obtained by adopting the leading-order boundary conditions (2.74) of Parker and Balachandar (1999). We achieved a further threefold gain in efficiency by dropping the line-relaxation method in favour of a pointwise iterative algorithm similar to that of Rubin and Grossman (1971). (For our code,

the line-relaxation algorithm increased the computational overhead threefold over the pointwise algorithm, but did not affect the number of iterations required for convergence.) A further five- to ten-fold efficiency gain was obtained by adopting the two-part domain composition illustrated in Figure 2.3. In this decomposition, Domain I corresponds to the inner corner region plus the blending layer, ie

$$\{\,(\eta,\zeta):\,0\le\zeta\le\zeta_{\max}\,,\;0\le\eta\le\min\{\eta^*,\zeta\}\,\}, \tag{2.76}$$

where $\eta^*\ge 5$ represents a generous estimate of the width of the blending layer; the governing equations herein are discretised with step-size $h_1 = h = 0.05$. Domain II corresponds to the inviscid outer region, ie

$$\{(\eta,\zeta):\,\eta^*\le\eta\le\zeta\le\zeta_{\max}\}, \tag{2.77}$$

where the governing equations reduce to

$$U=1, \qquad \theta=0, \qquad \nabla^2\phi\,=\,0, \qquad \nabla^2\psi\,=\,0, \tag{2.78}$$

and are discretized with step-size $h_2 = nh$ for some constant integer $n \approx 5$. Using this numerical scheme we achieved the strict convergence criterion of Dhanak and Duck (1997) that no flow variable should change by more than $\epsilon \approx 10^{-7}$ between successive iterations. Even so, domain convergence with respect to h and $\zeta_{\max}$ was somewhat weak, and we estimate that our results are accurate to no more than three figures. We will revisit the issue of domain convergence in §2.4.

2.4 Results

Here we present and discuss our numerical results for the laminar flow internal to a square corner. Except where stated otherwise, these results were obtained using the method of §2.3.6, with leading-order boundary conditions imposed at the artificial domain boundary $\zeta = \zeta_{\max} = 60$.

Figure 2.4 plots the velocity magnitude (U, Q), where

$$Q^2\,=\,V^2+W^2, \tag{2.79}$$

out to a distance of $\eta = 20$ and $\zeta = 20$ from the corner line. Clearly visible in this figure are the four sub-domains of the full corner region, namely

Corner-line vicinity:	$0<\eta,\zeta\lesssim 1,$	(2.80a)
Inner region:	$0<\eta,\zeta\lesssim 5,$	(2.80b)
Inviscid outer region:	$\eta,\zeta\gtrsim 5,$	(2.80c)
Blending boundary layer:	$0<\eta\lesssim 5\lesssim\zeta\lesssim\zeta_{\max}.$	(2.80d)

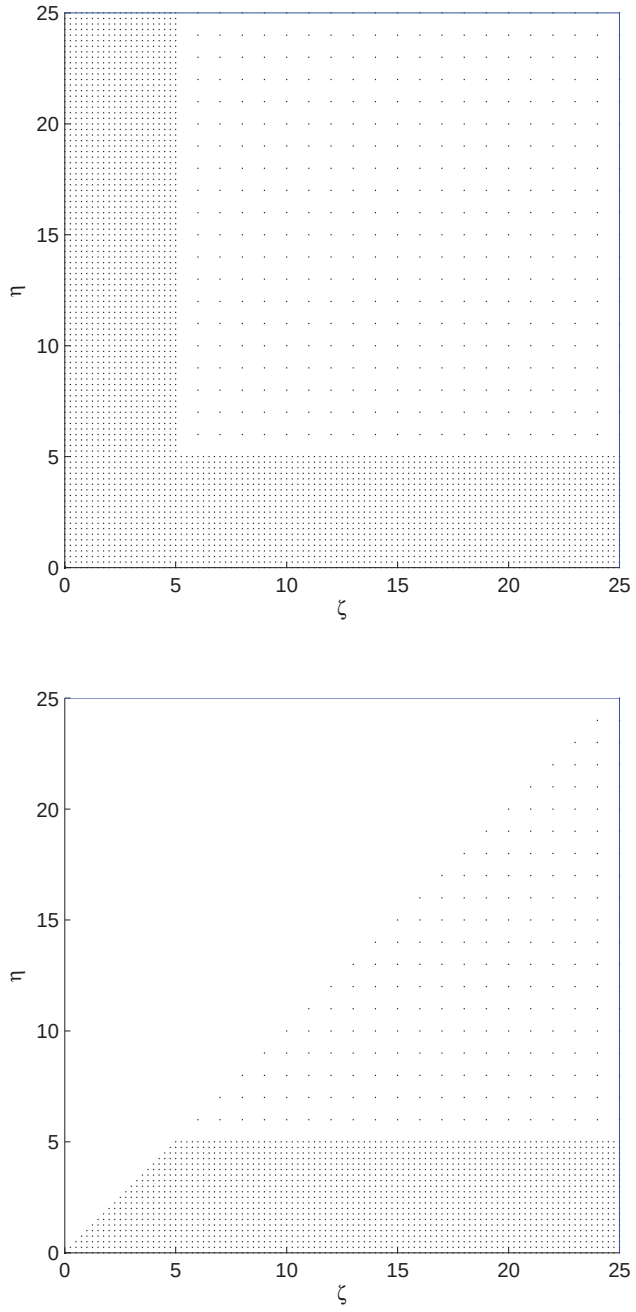

Figure 2.3: Schematic representation of our finite-difference grid before *(top)* and after *(bottom)* imposition of the bisector symmetry conditions (2.18). The inner region and blending boundary layer are discretised with step-size $h = 0.05$, while the inviscid outer region uses a coarse discretisation with $h \approx 0.25$.

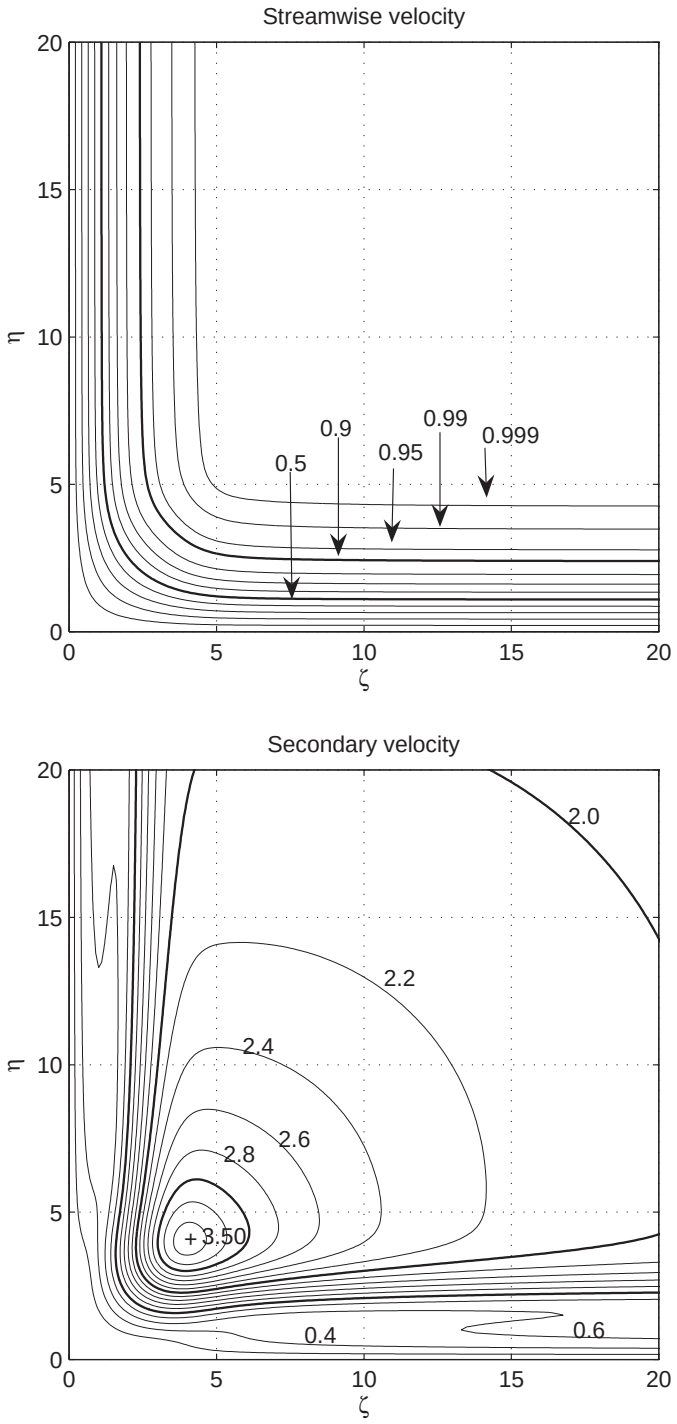

Figure 2.4: *Upper figure:* Contour plot of streamwise velocity $U(\eta, \zeta)$, with contour spacing $\Delta U = 0.1$; contours are also shown for $U = 0.95$, 0.99 and 0.999. *Lower figure:* Contour plot of the magnitude $Q = \sqrt{V^2 + W^2}$ of the secondary velocity, with contour spacing $\Delta Q = 0.2$; the contours for $Q = 1$, $Q = 2$ and $Q = 3$ are highlighted.

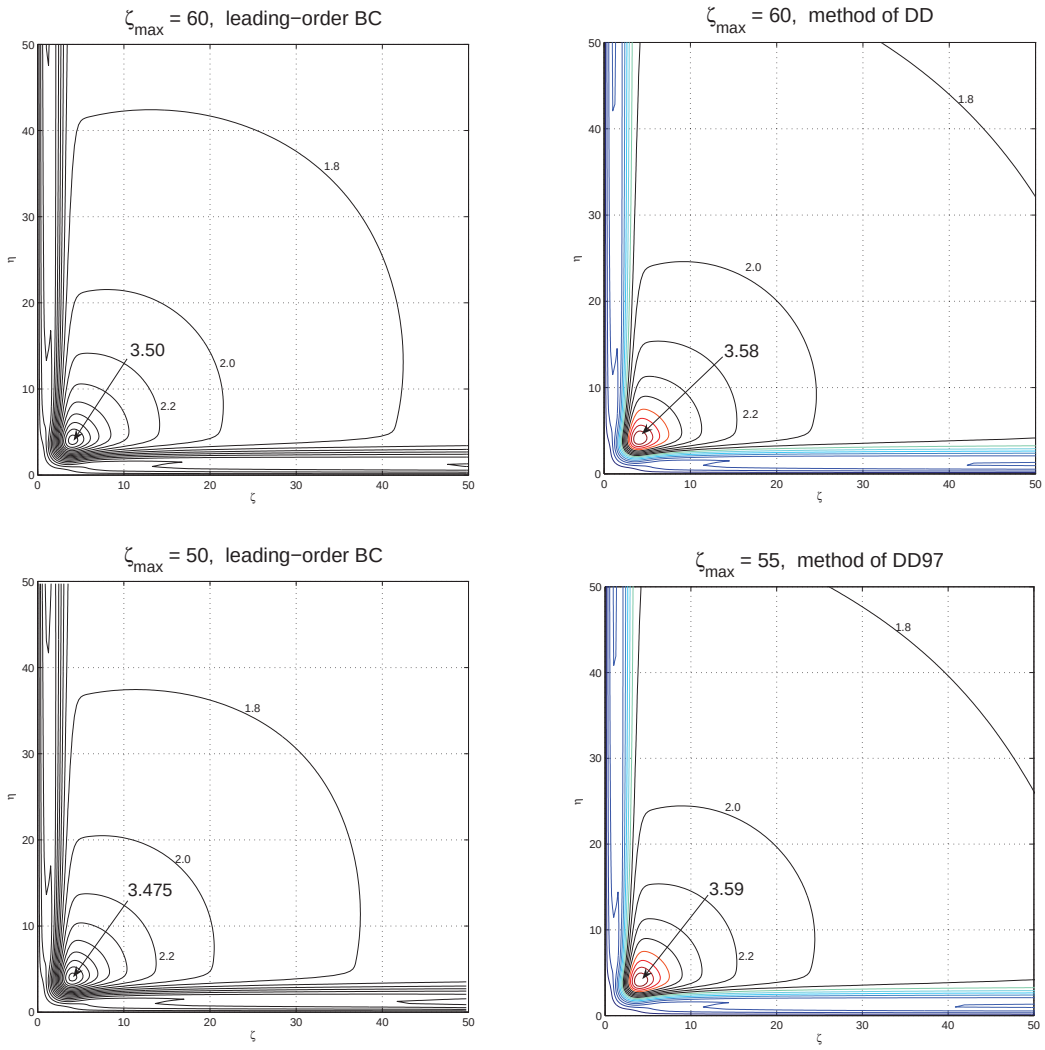

Figure 2.5: Magnitude $Q(\eta,\zeta) \equiv \sqrt{V^2+W^2}$ of the secondary velocity, computed using four different numerical schemes and plotted out to a distance of $\eta = 50$ and $\zeta = 50$. Throughout, the contour spacing is $\Delta Q = 0.2$, with maximum secondary velocity $Q_{\max}$ indicated by an arrow. *Upper left:* Computed using the leading-order far-field boundary conditions (2.74) applied at $\zeta_{\max} = 60$, as in Figure 2.4. *Lower left:* Computed using leading-order boundary conditions at $\zeta_{\max} = 50$. *Upper right:* Computed using the boundary conditions (2.72) of Dhanak and Duck (1997) applied at $\zeta_{\max} = 60$. *Lower right:* Computed using boundary conditions of DD at $\zeta_{\max} = 55$.

The *corner-line vicinity* may be described as a 'dead zone' wherein

$$U \lesssim 0.2 \qquad \text{and} \qquad Q/Q_\infty \lesssim 0.05 \qquad \text{for} \qquad \eta, \zeta \lesssim 1, \tag{2.81}$$

where

$$Q_\infty \equiv \lim_{\eta\to\infty} Q(\eta,\eta) = \sqrt{2}\beta \approx 1.721 \tag{2.82}$$

denotes the asymptotic magnitude of the secondary flow in the outer region. The *inner region* is characterised by strongly nonlinear interaction between the boundary layers adjacent to the walls at $\eta = 0$ and $\zeta = 0$. The *outer region* is a domain of constant streamwise velocity $U = 1$, zero streamwise vorticity Ω, and algebraically varying secondary velocity $Q > Q_\infty$. The *blending boundary layer* contains the most subtle features of the laminar flow. According to the asymptotic theory of Pal and Rubin (1971) and Rubin and Grossman (1971), the flow herein varies algebraically with spanwise distance ζ from the corner line:

$$(U,V) = (U_0(\eta),\, V_0(\eta)) + O\left(\zeta^{-2}\right) \qquad \text{for} \qquad \eta = O(1), \quad \zeta \gtrsim 5, \tag{2.83a}$$

$$(W,Q) = (W_0(\eta),\, Q_0(\eta)) + O\left(\zeta^{-1}\right) \qquad \text{for} \qquad \eta = O(1), \quad \zeta \gtrsim 5. \tag{2.83b}$$

This prediction is in qualitative agreement with Figure 2.4, which clearly shows U rapidly approaching its Blasius limit U_0 (it is virtually indistinguishable for $\zeta \gtrsim 10$), whereas Q approaches its limit Q_0 very slowly indeed.

Figure 2.5 plots the secondary velocity Q out to a distance of $\eta = 50$ and $\zeta = 50$. Here we assess domain convergence by plotting Q from *four separate data sets*. For the upper-left and lower-left plots in this figure, the flow was computed using leading-order boundary conditions (applied at $\zeta_{\max} = 60$ and $\zeta_{\max} = 50$ respectively), whereas the upper-right and lower-right plots were derived using the boundary conditions of Dhanak and Duck (1997) (applied at $\zeta_{\max} = 60$ and $\zeta_{\max} = 55$ respectively). It is clear that our numerical scheme achieved only a modest degree of domain convergence. For example, the four data sets yield values of 3.50, 3.475, 3.58 and 3.59 respectively for the global maximum $Q_{\max}$ of the secondary velocity. For comparison, $Q_{\max}$ values of 3.65, 3.2, 3.55 and 3.68 were obtained by Rubin and Grossman (1971), Ghia (1975)[6], Dhanak and Duck (1997)[7] and Balachandar and Malik (1995) respectively. This quantitative variation is highlighted by Figure 2.6, where we plot the bisector secondary velocity Q_{bis} defined by

$$Q_{\text{bis}}(\zeta) = Q(\eta,\zeta) \qquad \text{for} \qquad \eta = \zeta. \tag{2.84}$$

[6]Ghia's results appear to be inaccurate. This probably indicates that Ghia terminated his solution algorithm prematurely. Recall from §2.3.2 that Ghia mapped the entire quarter-infinite domain to a unit square, and solved the equations using < 300 iterations of the ADI algorithm.

[7]At first glance, Figure 6 of their paper suggests that $Q_{\max} \approx 2.5$; closer examination, however, reveals that their definitions of (V, W, Q, Ω) differ from ours by a factor of $\sqrt{2}$.

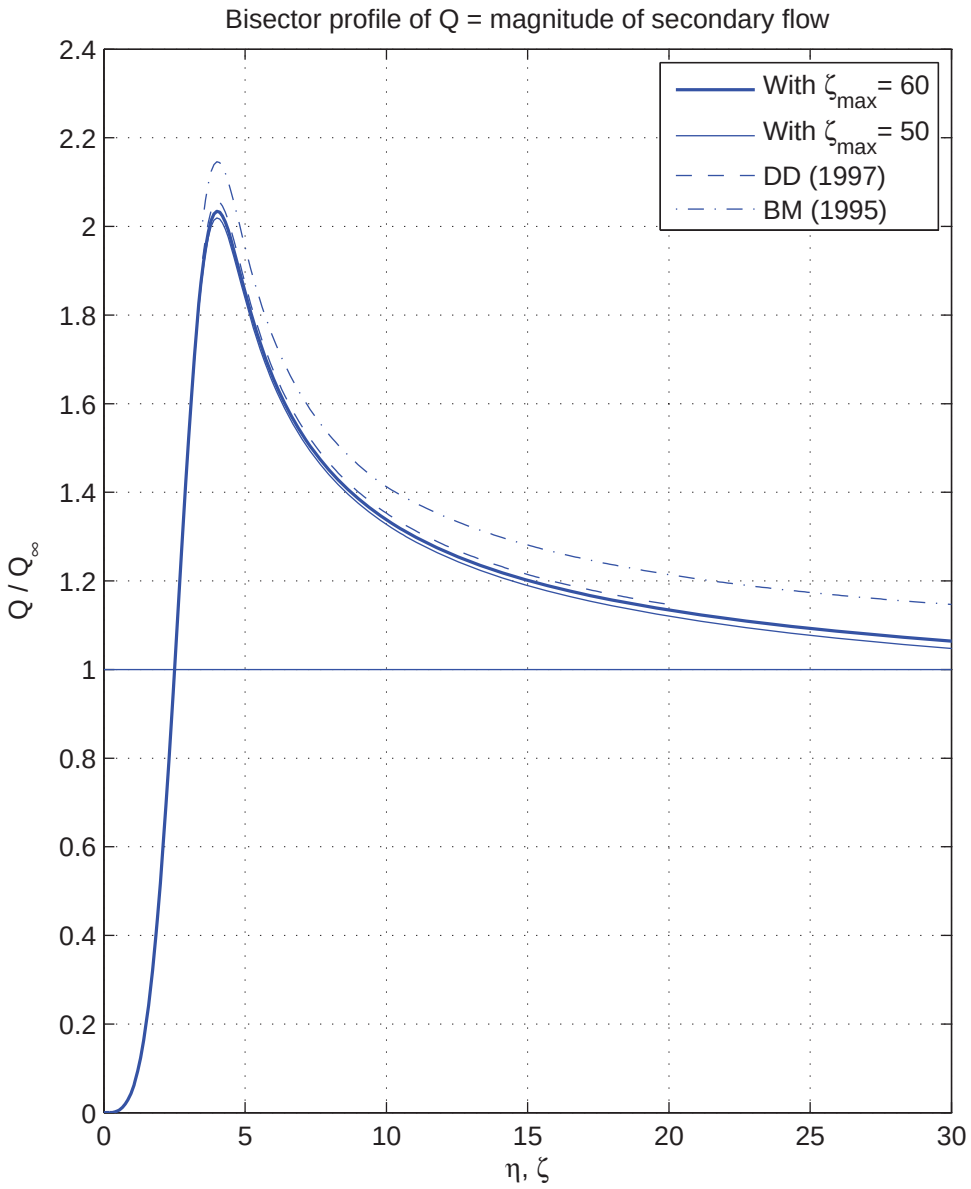

Figure 2.6: Magnitude $Q_{\rm bis}(\zeta)$ of the secondary velocity along the corner bisector, rescaled by the far-field limiting value $Q_\infty = 1.721$. The dark-solid and light-solid curves correspond to the upper-left and lower-left panels of Figure 2.5. The dashed and dot-dashed lines show the results of Dhanak and Duck (1997) and Balachandar and Malik (1995) respectively.

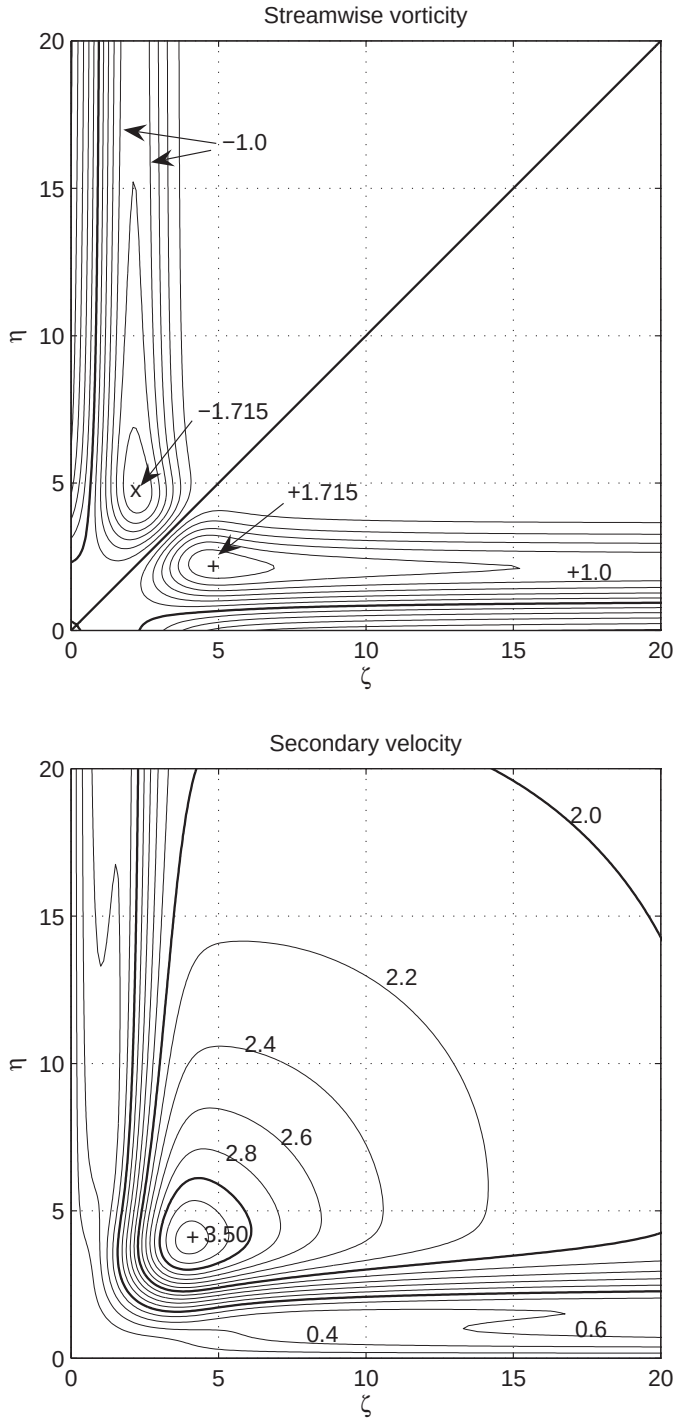

Figure 2.7: Contour plot *(upper figure)* of the streamwise vorticity $\Omega \equiv W_\eta - V_\zeta$, with contour spacing $\Delta\Omega = 0.25$ and zero contours highlighted. For comparison, the contour plot of Q from Figure 2.4 is reproduced underneath.

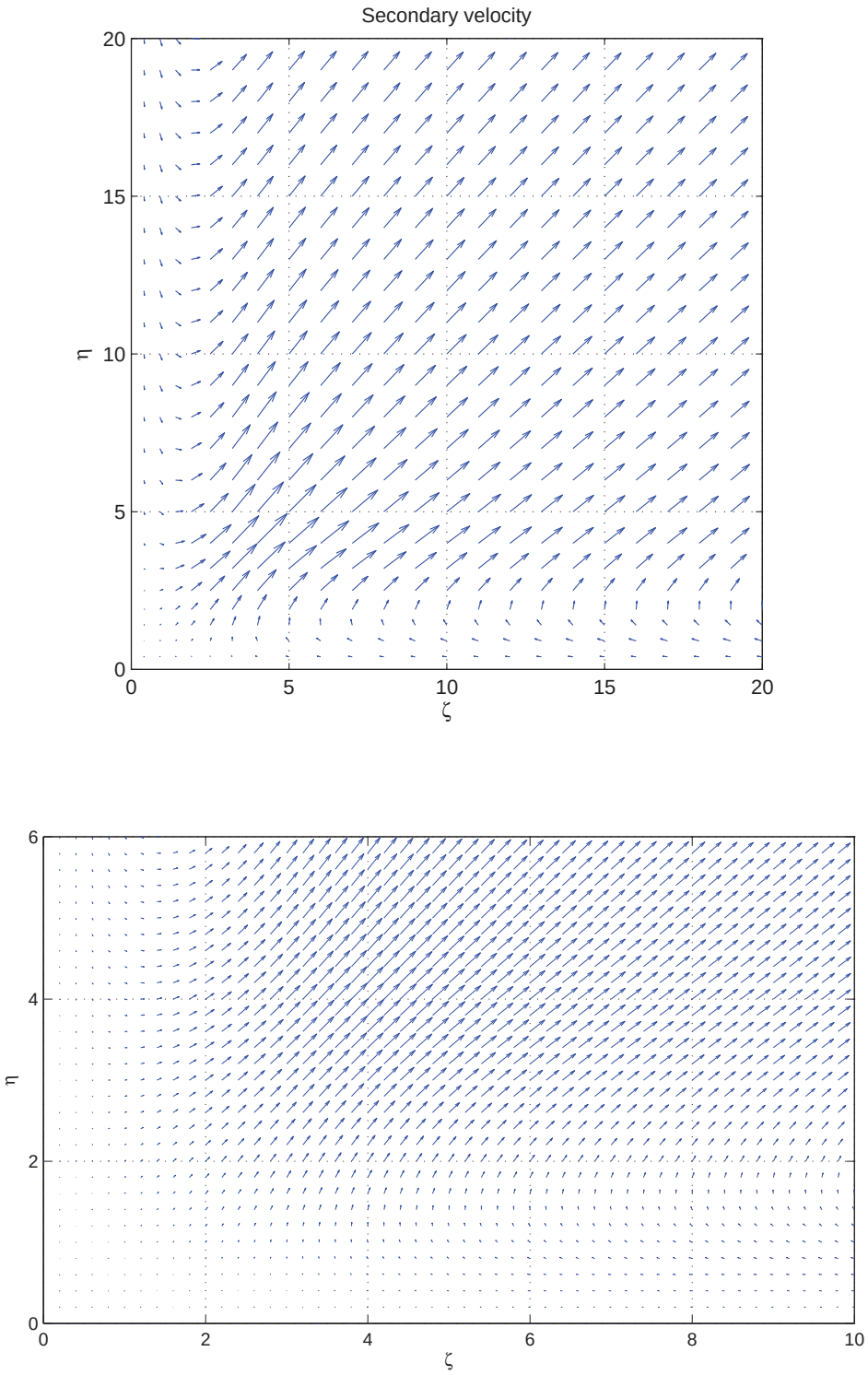

Figure 2.8: Vector plot of the secondary velocity (V, W). The lower figure is a detail of the inner corner region and the blending boundary layer out to a spanwise distance of $\zeta = 10$.

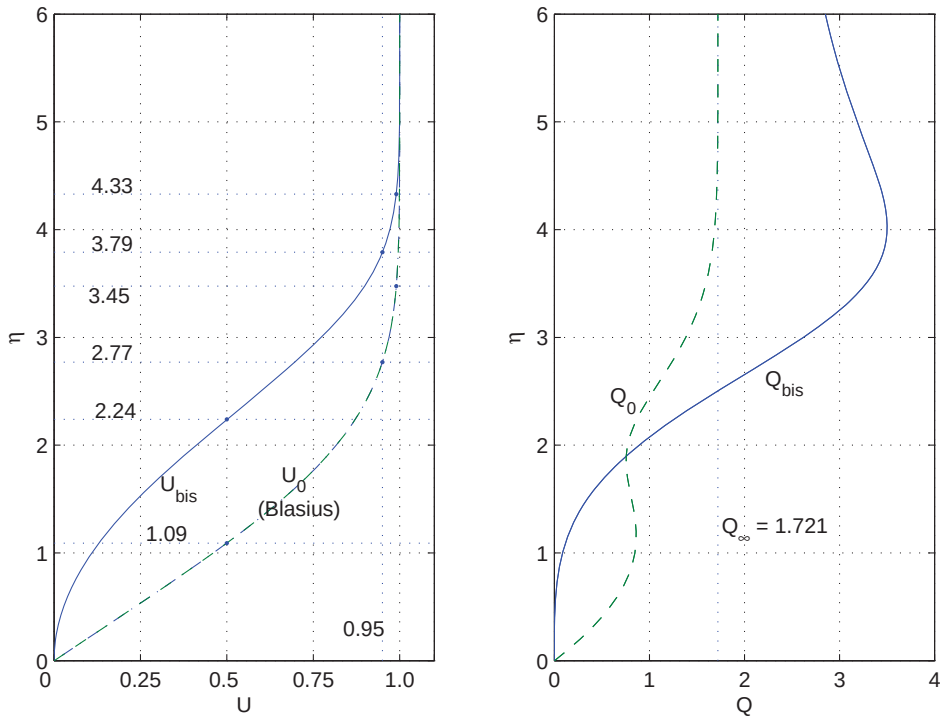

Figure 2.9: *Left:* The Blasius velocity profile $U_0(\eta)$ (imposed at the far-field boundary $\zeta = \zeta_{\max}$) and the streamwise bisector profile $U_{\rm bis}(\eta) = U(\eta, \eta)$. Dots along the velocity profiles correspond to values of $U = 0.5$, 0.95 and 0.99. *Right:* Secondary velocity profiles $Q_0(\eta)$ and $Q_{\rm bis}(\eta) = \sqrt{2}V(\eta, \eta) = \sqrt{2}W(\eta, \eta)$, corresponding respectively to $\zeta = \zeta_{\max}$ and the corner bisector.

For $10 \lesssim \zeta \lesssim 20$, all of the data sets are consistent with the theoretical prediction of Rubin and Grossman (1971) that

$$Q \;=\; Q_\infty \;+\; O\left(\rho^{-1}\right) \qquad \text{for} \qquad \rho^2 \equiv \eta^2 + \zeta^2 \gg 1. \tag{2.85}$$

For $\zeta \gtrsim 20$, however, our $Q_{\rm bis}(\zeta)$ profile decays faster than $O(\zeta^{-1})$. This accelerated decay appears to be artificial, induced by the far-field boundary condition $Q_{\rm bis} = Q_\infty$ at $\zeta = \zeta_{\max} = 60$. No such acceleration is evident in the data of Balachandar and Malik (1995), which was derived using the full blending-layer asymptotic expansion of Rubin and Grossman (1971) (albeit without the outer-region expansion of Rubin and Grossman). The Rubin and Grossman data set for $Q_{\rm bis}(\zeta \leq 15)$ is found to be almost indistinguishable from the Balachandar and Malik data; in the interests of clarity, therefore, it is not shown in Figure 2.6.

We now turn our attention to the inner region. Figure 2.9 plots the primary and secondary bisector profiles $U_{\rm bis}$ and $Q_{\rm bis}$ respectively out to $\zeta = \eta = 6$. It is clear that both velocity profiles are strongly inflectional in character. This, of course, is to

be expected on geometric grounds, especially given the very low velocities (2.81) of the inner-core region. However, the secondary profile $Q_{\rm bis}$ differs qualitatively from $U_{\rm bis}$ in the sense that it overshoots its far-field limit Q_∞. Its maximum coincides with the global maximum of Q, namely

$$Q_{\max} \approx (2.1)Q_\infty, \qquad \text{attained at} \qquad \zeta = \eta \approx 4.0, \tag{2.86}$$

ie within the transition zone between the inner and outer regions. The overshoot phenomenon is a continuity effect, effectively balancing out the low inner-core velocities; note that the bisector marks the *locus of collision* between the outflow velocities from the two Blasius-type boundary layers.

It was Rubin and Grossman (1971) who first demonstrated the strongly inflectional nature of the streamwise bisector profile $U_{\rm bis}$. Some degree of inflectional character is, of course, to be expected on purely geometric grounds. Nevertheless, Figures 4 and 5 of their paper demonstrate that this effect is substantially more prominent, and the inner corner region significantly larger, than that implied by Carrier's (1947) model of weakly-nonlinear boundary-layer interaction. Indeed, it is this vigorous interaction which is responsible for the well-rounded streamwise contours evident in our Figure 2.4.

We close this section with a closer examination of the blending boundary layer. Figure 2.7 compares the streamwise vorticity $\Omega \equiv W_\eta - V_\zeta$ with the magnitude Q of the secondary velocity. Both plots show substantial spanwise variation consistent with the theoretical result (2.83). The vorticity extrema, marked in Figure 2.7 by crosses, are located at $(\eta, \zeta) \approx (2.2, 4.8)$ and $(4.8, 2.2)$, ie in the transition region between the blending boundary layer and the inner corner region. A startling feature of the secondary velocity is the wide spacing between the contours corresponding to $Q = 0.4$, 0.6 and 0.8. Equally startling is that the $Q = 0.6$ contour actually doubles in on itself over the sub-domain $13 \lesssim \zeta \lesssim 17$. These local features coincide closely with the zero-vorticity contour, which indicates a reversal of the crossflow component W approximately midway through the blending layer. This is clearly evident in the transverse vector plot of Figure 2.8 and the boundary-layer velocity profiles of Figure 2.10. The precise location η^* of crossflow reversal depends strongly on the spanwise coordinate ζ; it increases monotonically from $\eta^* = 0$ at $\zeta = 2.4$ to $\eta^* = 1.36$ at $\zeta = 5$, $\eta^* = 1.90$ at $\zeta = 20$, and $\eta^* = 2.15$ at $\zeta = \zeta_{\max}$. Figure 2.11 plots the wall shear stress (σ, μ) defined by

$$\sigma(\zeta) = U_\eta(0, \zeta), \qquad \mu(\zeta) = W_\eta(0, \zeta) \equiv Q_\eta(0, \zeta). \tag{2.87}$$

The dashed curves in this figure compare our results with the following asymptotic

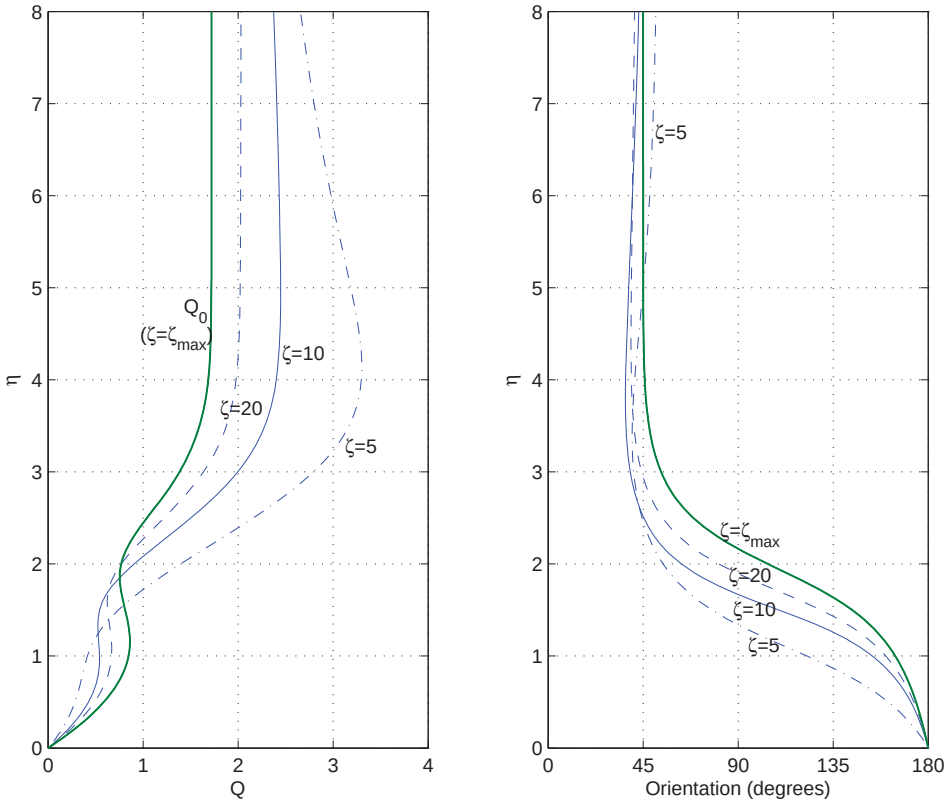

Figure 2.10: *Left:* Magnitude $Q(\eta;\zeta)$ of the secondary velocity in the blending layer, plotted as a function of η at spanwise stations of $\zeta = 5$, $\zeta = 10$ and $\zeta = 20$. The heavy curves indicate the far-field limit $Q_0(\eta)$ of the secondary velocity (enforced at $\zeta = \zeta_{\max} = 60$). *Right:* Orientation of the secondary velocity, plotted as a function of η for $\zeta = 5$, $\zeta = 10$ and $\zeta = 20$. An orientation value below 90 degrees indicates an outflow from the corner, while a value above 90 indicates an inflow.

shear values of Rubin and Grossman (1971):

$$\sigma = \sigma_0(1 - \kappa\zeta^{-2}) + O\left(\zeta^{-3}\right) \qquad \text{for} \quad \zeta \gg 1, \tag{2.88a}$$

$$\mu = \mu_0 + 4\kappa\zeta^{-1} + O\left(\zeta^{-2}\right) \qquad \text{for} \quad \zeta \gg 1, \tag{2.88b}$$

where $\kappa \approx 2.5$ is an empirical constant, and (σ_0, μ_0) are given by

$$\sigma_0 = f''(0) = 0.470, \tag{2.89a}$$

$$\mu_0 = -\beta^2 = -1.481. \tag{2.89b}$$

It is clear that our values for $|\sigma - \sigma_0|$ and $|\mu - \mu_0|$ are consistently smaller than those of Rubin and Grossman (1971); nevertheless, qualitative agreement is very good throughout.

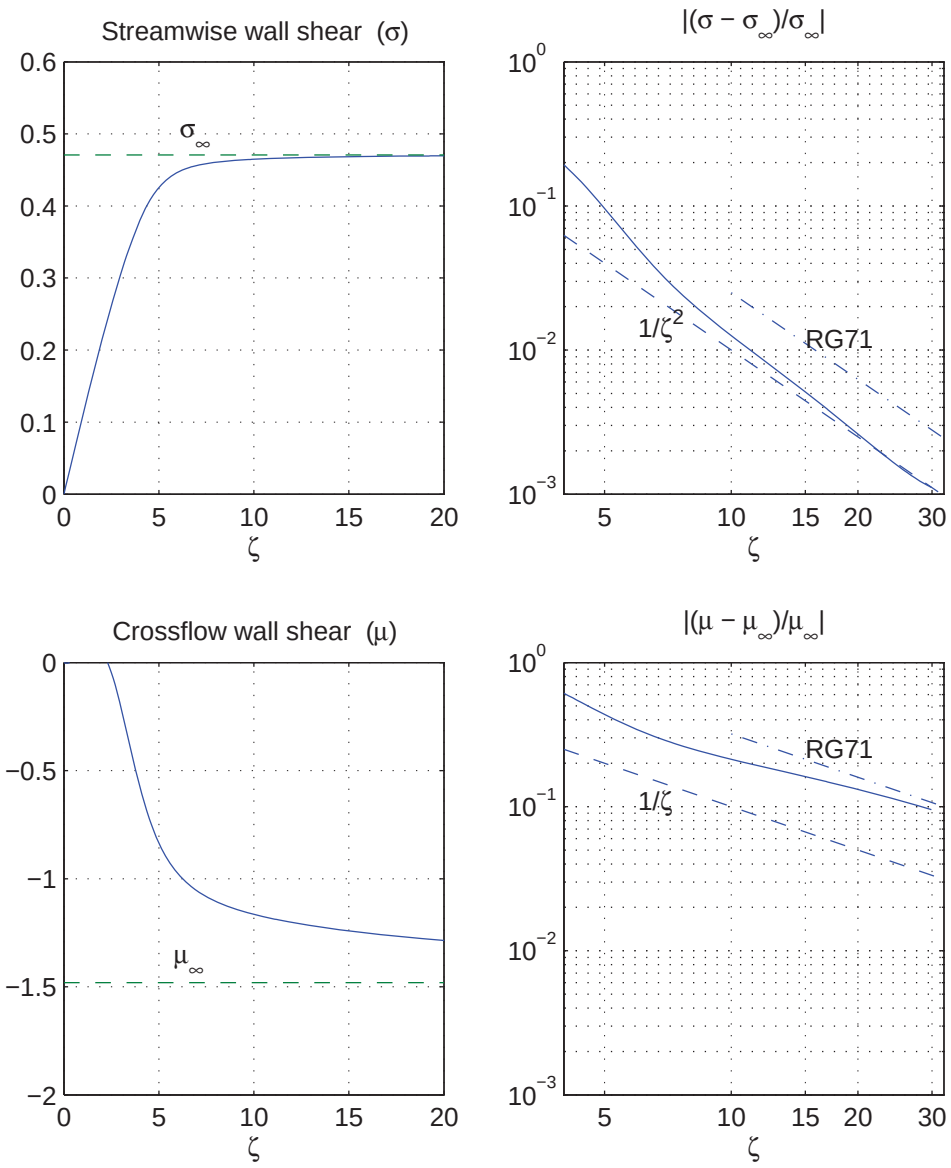

Figure 2.11: *Upper left:* The streamwise wall shear $\sigma(\zeta) = U_\eta(0,\zeta)$. *Lower left:* The crossflow wall shear $\mu(\zeta) = W_\eta(0,\zeta)$. *Upper right:* The relative difference between $\sigma(\zeta)$ and its far-field limit σ_∞, plotted on a logarithmic scale. The dot-dashed curve labelled *RG71* corresponds to the asymptotic results of Rubin and Grossman (1971). *Lower right:* The relative difference between $\mu(\zeta)$ and its far-field limit μ_∞ (dot-dashed curve indicates the results of Rubin and Grossman (1971)).

Chapter 3

Stability of laminar flow in an internal corner

3.1 Introduction

In Chapter 2 we computed the laminar flow internal to a square corner in the absence of a streamwise pressure gradient. The hydrodynamic stability of this laminar flow is the subject of the present chapter. Ideally, we would like to exhibit a critical Reynolds number Re_c such that the laminar flow is stable for $Re < Re_c$. Conversely, for $Re > Re_c$ the flow would be unstable, and in practice would be expected to transition to a turbulent state. Recall from §2.4 that its streamwise component $u \equiv U(\eta, \zeta)$ has a strongly inflectional profile along the corner bisector (see, for example, Figure 2.9). This leads us to speculate that the flow possesses one or more inviscid-type modes of instability centred on the inner corner boundary layer. In particular, we hypothesize that this flow is less stable than an equivalent two-dimensional Blasius boundary layer (for which $Re_c \approx 9 \times 10^4$).

The structure of this chapter is as follows. In §3.2 we derive the leading-order linearized governing equations for eigenmode instabilities in the laminar flow internal to a square corner. Sections 3.3 to 3.5 focus on inviscid-type modes of instability; the eigenmode governing equations are solved in the formal ('inviscid') limit $Re \to \infty$ using three different numerical schemes. Finally, §3.6 considers both viscous- and inviscid-type modes at finite Reynolds number.

3.2 Governing equations

Our stability analysis of the laminar corner flow $\mathbf{u} = (u, v, w)$ relies on the parallel-flow approximation that the boundary-layer scaling

$$O\left(x/Re_x^{1/2}\right) \equiv O\left(x^{\frac{1}{2}}\, Re^{-\frac{1}{2}}\right) \tag{3.1}$$

is essentially constant over the characteristic streamwise scale $\Delta x = O\left(Re^{-\frac{1}{2}}\right)$ of Tollmien–Schlichting instabilities. This assumption allows us to apply a streamwise-similar normal-mode analysis. That is, we 'seed' the flow with an infinitesimal wavelike perturbation of the form

$$\epsilon\widetilde{\mathbf{u}} \equiv \epsilon\widetilde{\mathbf{U}}(\eta, \zeta)\, \mathrm{e}^{\mathrm{i}\alpha R(x-ct)} \tag{3.2}$$

where $\epsilon \ll 1$ is an arbitrary small constant, α is a real-valued streamwise wavenumber, c is a complex-valued wave-speed, and R is a scale factor based on boundary-layer width and free-stream velocity. It proves convenient to define R by

$$R = \left(\frac{Re}{2}\right)^{\frac{1}{2}}, \qquad \text{ie} \qquad Re = 2R^2, \tag{3.3}$$

where the Reynolds number Re (defined in §1.3.1) is based on streamwise distance from the leading edge.

On substituting the total velocity

$$\mathbf{u}_{\text{total}} \equiv \mathbf{u} + \epsilon\widetilde{\mathbf{u}} \tag{3.4}$$

into the unsteady Navier–Stokes equations, and retaining only the $O(\epsilon)$ leading-order terms in $\widetilde{\mathbf{u}}$, we obtain the following equations:

$$\mathrm{i}\alpha U + V_\eta + W_\zeta = 0, \tag{3.5a}$$

$$\mathrm{i}\alpha(u-c)U + u_\eta V + u_\zeta W + \mathrm{i}\alpha P = \frac{1}{\sqrt{2Re}}\nabla^2 U, \tag{3.5b}$$

$$\mathrm{i}\alpha(u-c)V + P_\eta = \frac{1}{\sqrt{2Re}}\nabla^2 V, \tag{3.5c}$$

$$\mathrm{i}\alpha(u-c)W + P_\zeta = \frac{1}{\sqrt{2Re}}\nabla^2 W, \tag{3.5d}$$

$$\nabla^2 \equiv \frac{\partial^2}{\partial\eta^2} + \frac{\partial^2}{\partial\zeta^2} - \alpha^2, \tag{3.5e}$$

where we have simplified the notation by dropping the tildes and letting $u \equiv u(\eta, \zeta)$ denote the streamwise laminar flow. These governing equations are to be solved subject to the no-slip conditions

$$U = V = W = 0 \qquad \text{at} \qquad \eta = 0 \quad \text{and} \quad \zeta = 0, \tag{3.6}$$

together with bisector symmetry conditions and asymptotic far-field conditions (to be discussed in more detail later in this chapter). Two classes of correction terms are absent from the governing equations (3.5): nonlinear terms in $\widetilde{\mathbf{u}}$ of order $O(\epsilon^2)$ and higher; and advective terms of order $O(R^{-1}\epsilon)$ involving the laminar secondary velocity (v, w). (The latter terms are, however, retained by Dhanak and Duck (1997) and Parker and Balachandar (1999).) If the $O(R^{-1}\epsilon)$ viscous terms are also dropped, one obtains the 'inviscid instability' equations:

$$\mathrm{i}\alpha U + V_\eta + W_\zeta = 0, \tag{3.7a}$$

$$\mathrm{i}\alpha(u-c)U + u_\eta V + u_\zeta W + \mathrm{i}\alpha P = 0, \tag{3.7b}$$

$$\mathrm{i}\alpha(u-c)V + P_\eta = 0, \tag{3.7c}$$

$$\mathrm{i}\alpha(u-c)W + P_\zeta = 0. \tag{3.7d}$$

Since viscosity is absent in the limit $Re \to \infty$ (except through the underlying laminar flow $u(\eta, \zeta)$), the no-slip condition (3.6) on (3.5) weakens to a no-penetration condition on (3.7), ie

$$V = 0 \quad \text{at} \quad \eta = 0, \qquad W = 0 \quad \text{at} \quad \zeta = 0. \tag{3.8}$$

The inviscid equations make no explicit reference to the Reynolds number, and therefore cannot yield a critical Reynolds number. Furthermore, they are clearly singular in the special case that c is real-valued with $0 < c < 1$. Nevertheless, they are attractive for a preliminary stability analysis, since they decouple to yield a single equation involving only the perturbation pressure $P \equiv P(\eta, \zeta)$. This is the two-dimensional Rayleigh equation, a second-order partial differential equation involving the eigenvalue c:

$$(u-c)\nabla^2 P - 2(u_\eta P_\eta + u_\zeta P_\zeta) = 0. \tag{3.9}$$

It is to be solved subject to Neumann boundary conditions, ie

$$P_\eta = 0 \quad \text{at} \quad \eta = 0, \qquad P_\zeta = 0 \quad \text{at} \quad \zeta = 0. \tag{3.10}$$

Its solution is the theme of the second half of the Balachandar and Malik (1995) paper. We devote §3.3, §3.4 and §3.5 to its solution, before tackling the viscous-instability equations (3.5) in §3.6.

3.3 Method 1 (Inviscid)

3.3.1 Outline

We discretize the Rayleigh equation (3.9) in the (η, ζ) plane using a standard finite-difference (FD) scheme. The discretised system reduces to a generalised eigenvalue

problem of the form

$$\mathbf{Ap} = c\mathbf{Bp} \tag{3.11}$$

where the complex-valued vector $\mathbf{p}$ denotes mesh values of the perturbation pressure $P(\eta, \zeta)$. In principle, the eigenvalue equation (3.11) is amenable to the QZ algorithm. However, this approach would be feasible only for coarse discretisations leading to fewer than $O(10^4)$ unknowns. Instead, we use the iterative algorithm of Otto and Denier (1999) to extract only the leading eigenvalues c of (3.11). This approach, unlike the QZ algorithm, promises large efficiency gains through exploitation of the sparsity structure of the $\mathbf{A}$ and $\mathbf{B}$ matrices. Our full numerical scheme is implemented in purpose-written Fortran 90 code.

3.3.2 Details

We discretize the Rayleigh equation (3.9) and its Neumann boundary condition (3.10) over the truncated domain $\mathcal{D}$ defined by

$$\mathcal{D} = \{(\eta, \zeta) : 0 \le \eta, \zeta \le \zeta_{\max}\} \tag{3.12}$$

where $\zeta_{\max}$ is an arbitrary large constant. By assuming that the eigenfunction is symmetric with respect to the bisector, ie

$$P(\zeta, \eta) = P(\eta, \zeta), \tag{3.13}$$

we reduce the working domain $\widetilde{\mathcal{D}}$ to the sub-bisector region defined by

$$\widetilde{\mathcal{D}} = \{(\eta, \zeta) : 0 \le \eta \le \zeta \le \zeta_{\max}\}. \tag{3.14}$$

Following Balachandar and Malik (1995), we close the above system of equations by applying a Neumann boundary condition at the far-field boundary:

$$P_\zeta = 0 \quad \text{at} \quad \zeta = \zeta_{\max}. \tag{3.15}$$

The discretized system yields a total of approximately $\frac{1}{2}N^2$ unknowns, where N is the number of mesh points in each of the η and ζ coordinates. For example, a uniform grid with spacing $h = 0.1$ and boundary $\zeta_{\max} = 20$ would yield approximately $\frac{1}{2}(200^2) = 2 \times 10^4$ working variables. In practice, however, we use a three-part domain decomposition as illustrated in Figure 3.1. This decomposition applies a fine mesh to the corner region proper, a coarse mesh to the outer region, and a hybrid mesh to the blending boundary layer. The respective grid-spacing parameters are as follows:

$$\text{Inner:} \qquad h_\eta \equiv h_\zeta = h_1 \qquad \text{for} \qquad 0 < \eta, \zeta < \eta^*, \tag{3.16a}$$

$$\text{Outer:} \qquad h_\eta \equiv h_\zeta = h_2 \qquad \text{for} \qquad \eta^* < \eta, \zeta < \zeta_{\max}\,, \tag{3.16b}$$

$$\text{BL:} \qquad (h_\eta,\, h_\zeta) = (h_1, h_2) \qquad \text{for} \qquad 0 < \eta < \eta^* < \zeta < \zeta_{\max}\,, \tag{3.16c}$$

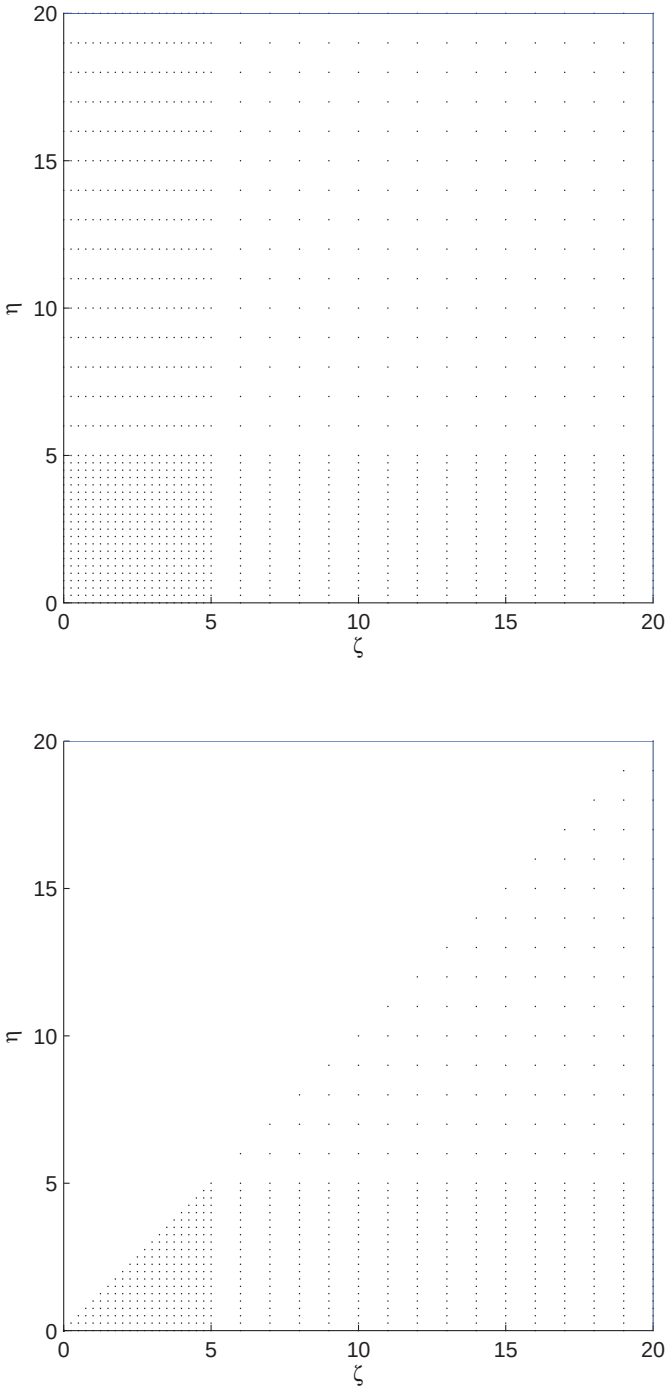

Figure 3.1: *Upper figure:* Schematic representation of the discretization (3.16) of the full computational domain $\mathcal{D}$ of spanwise size $\zeta_{\max} = 20$. The actual computational grid is approximately two to five times denser than shown here. *Lower figure:* Discretization of the reduced domain $\widetilde{\mathcal{D}}$ corresponding to the sub-diagonal domain $0 \leq \eta \leq \zeta \leq \zeta_{\max}$.

where

$$h_1 = O(10^{-1}), \tag{3.17a}$$

$$h_2 = nh_1 \qquad \text{for } n \text{ integer} \quad (1 < n \leq 6), \tag{3.17b}$$

$$\eta^* \approx 5. \tag{3.17c}$$

For example, the parameter set

$$h_1 = 0.1, \quad n = 4, \quad h_2 = 0.4, \quad \eta^* = 6.0, \quad \zeta_{\max} = 20, \quad N = 96,$$

yields approximately 4500 unknowns.

The traditional approach is to express the discretized governing equations as a generalized eigenvalue problem of the form (3.11), which is then solved using the QZ algorithm. Unfortunately, the storage cost of this scheme scales as $O(N^4)$, while the computational time required by the eigensolver scales as $O(N^6)$. Furthermore, no savings can be made by exploiting matrix sparsity, since this property is destroyed by the QZ algorithm. This situation is regrettable, since our matrices $\mathbf{A}$ and $\mathbf{B}$ are very large and very sparse. In fact, each matrix has a block-diagonal structure, namely block-tridiagonal in the case of second-order differencing (FD2) and block-pentadiagonal for a FD4 scheme (note, however, that accuracy may decrease to first-order or second-order respectively at domain boundaries). To exploit this sparsity structure, we discard the QZ algorithm in favour of the algorithm of Otto and Denier (1999). Adapted to our problem, their algorithm is as follows:

1. Choose some estimate $\widetilde{c}_0$ of the true eigenvalue c.

2. Formulate the eigenvalue problem (ie Rayleigh pressure equation plus boundary conditions) as the homogeneous matrix equation $\mathbf{Ap} = \mathbf{0}$, where $\mathbf{A}$ is a linear function of the eigenvalue estimate $\widetilde{c}$. This matrix has $O(N^4)$ entries, of which only $O(N^2)$ are non-zero. Since $\mathbf{A}$ has a block-diagonal structure, it may readily be stored as a sequence of block matrices of size $N \times N$, for a total storage cost of $O(N^3)$.

3. To ensure a non-trivial solution, the above system must be perturbed to a non-homogeneous one. To do this, first select a normalization point $\mathbf{z}_0 = (\eta_0, \zeta_0)$ and locate the corresponding row of $\mathbf{A}$. Then substitute this matrix row by the normalization equation $P(\mathbf{z}_0) = 1$, to yield

$$\widetilde{\mathbf{A}}\widetilde{\mathbf{p}} = \mathbf{e} \tag{3.18}$$

where $\mathbf{e} = (0, 0, ..., 0, 1, 0, ..., 0)$ is the corresponding unit vector.

4. Solve the resulting matrix equation, using a block-matrix algorithm to exploit the sparsity of $\mathbf{A}$. The computation time of this algorithm scales as $O(N^4)$.

5. In general, $\widetilde{\mathbf{p}}$ will not satisfy the differential equation at the normalization point $\mathbf{z}_0$. Obtain a complex-valued error statistic $\epsilon(\widetilde{c}) \equiv \epsilon_r + \mathrm{i}\epsilon_i$ by retrospectively evaluating the differential equation at $\mathbf{z}_0$.

6. Repeat steps 2–5 for the estimates $\widetilde{c}_1 = \widetilde{c}_0 + \delta$ and $\widetilde{c}_2 = \widetilde{c}_0 + \mathrm{i}\delta$, where $\delta = O(10^{-3})$ is an arbitrary real constant.

7. Hence, estimate the local gradient $\mathrm{d}\epsilon/\mathrm{d}\widetilde{c}$ of the complex-valued error statistic. Separate out its real and imaginary components, to generate a 2×2 derivative matrix $\mathbf{D}$ for ϵ.

8. Apply the gradient-descent method, inverting $\mathbf{D}$ to obtain a new estimate $\widetilde{c}_3$ of c.

9. Return to Step 2 and the above algorithm until the estimates converge *(success)* or diverge *(failure)*.

The above algorithm is not difficult to program, provided that a suitable starting estimate $\widetilde{c}_0$ can be found. To do this, we first perform a preliminary analysis using a truncated version of the above algorithm. In this mode of operation we drop the gradient descent phase; instead, we merely compute ϵ values corresponding to a large number of $\widetilde{c}$ values. Next, as shown in Figure 3.2, we produce separate contour plots of ϵ_r and ϵ_i in the complex $\widetilde{c}$-plane. Finally, we superimpose the two contour plots and identify any points of intersection between their respective zero contours. The coordinates of these points constitute starting estimates for the full algorithm.

3.3.3 Results

Our iterative finite-difference scheme yielded tantalizing but inconclusive results.

Before delving any further, it is instructive to review the results of Balachandar and Malik (1995). Like us, they chose to solve the inviscid instability equations in the hope of controlling computational costs (although they differed from us in using a QZ algorithm coupled with a spectral-based discretization of the Rayleigh equation). They reported two modes of inviscid instability active over the wavenumber range $0.1 \lesssim \alpha \lesssim 0.3$. The more vigorous mode attains its maximum growth rate of $\omega = 0.003975$ at a wavenumber of $\alpha = 0.225$, corresponding to an eigenvalue of $c = 0.48 + 0.0177\mathrm{i}$.

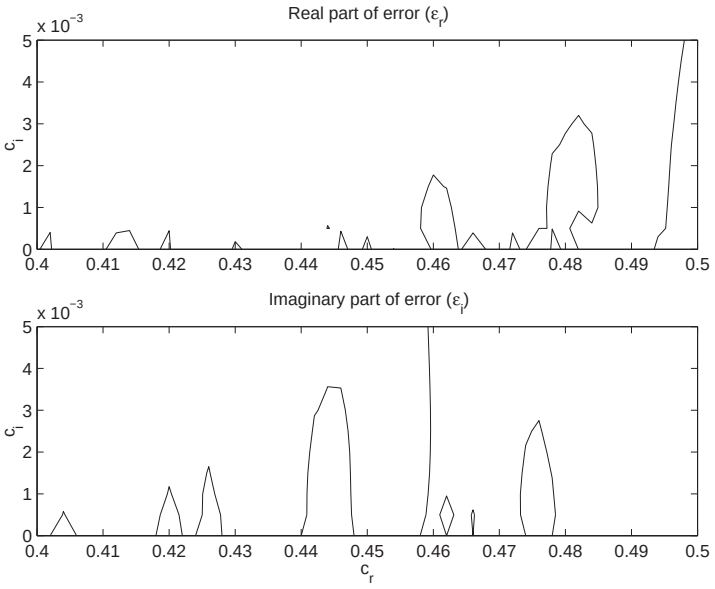

Figure 3.2: Preliminary results from Method 1 as described in §3.3.2. The analysis yields a complex-valued error statistic $\epsilon \equiv \epsilon_r + \mathrm{i}\epsilon_i$ as a function of the estimate $\widetilde{c}$ of the true eigenvalue c. The upper and lower contour figures plot ϵ_r and ϵ_i respectively in the complex $\widetilde{c}$ plane. (In the interests of clarity, we show only the zero contours.) Any point c^* of intersection between the respective zero contours suggests the presence of a genuine eigenvalue. This figure was generated using 500 iterations of the preliminary algorithm, corresponding to an equispaced mesh of 50×10 points in the $\widetilde{c}$–plane.

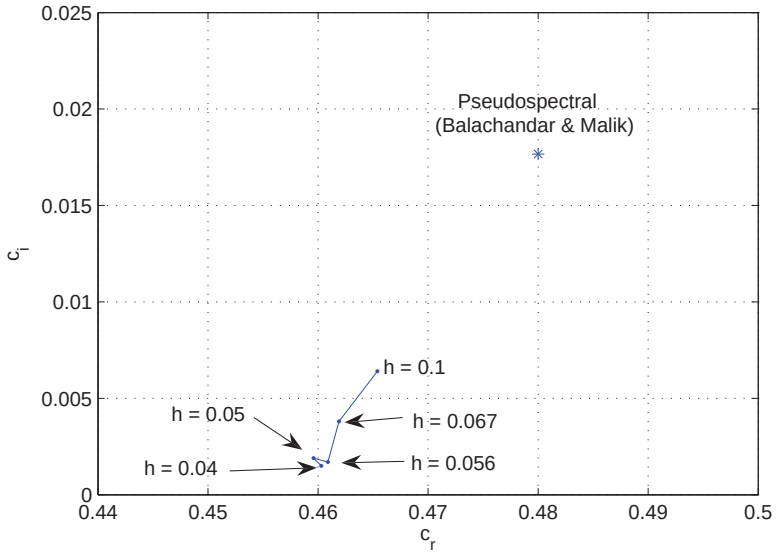

Figure 3.3: The leading eigenvalue c, as computed by Method 1 with fourth-order finite-difference discretization and plotted as a function of $h \equiv h_1$, the boundary-layer grid-spacing. Also shown is the leading eigenvalue reported by Balachandar and Malik (1995).

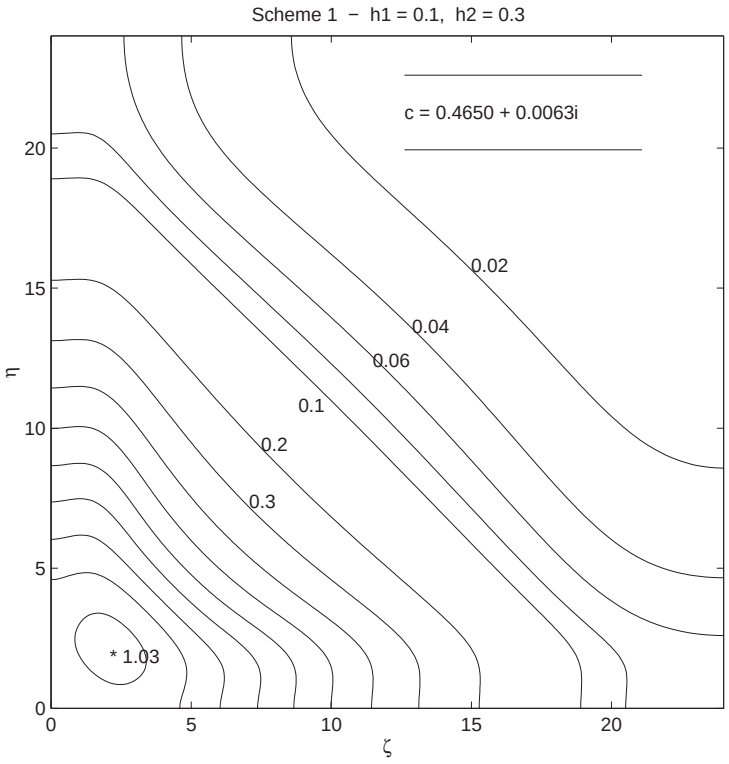

Figure 3.4: The leading eigenmode of inviscid instability, as computed by Method 1 with grid-spacing $h = 0.1$ and streamwise wavenumber $\alpha = 0.225$. Here we plot the amplitude $|P(\eta, \zeta)|$ of the perturbation pressure (the indicated maximum $|P| \approx 1.03$ is arbitrary). The corresponding eigenvalue is $c = 0.465 + 0.006\mathrm{i}$.

Our method failed to identify either of the eigenmodes reported by Balachandar and Malik (1995). Furthermore, our preliminary results were not encouraging, in the sense that they did not yield smooth, regular contour plots of the error statistic ϵ. Nevertheless, our method appeared to identify an eigenmode with an eigenvalue of $c = 0.46 + 0.002\mathrm{i}$ at $\alpha = 0.225$. Indeed, Figure 3.3 illustrates numerical convergence of this eigenvalue with respect to the parameter h_1 defined by (3.16) and (3.17). These results were generated using a FD4 discretization, and were insensitive to the artificial computational parameters h_2, η^* and $\zeta_{\max}$.

The eigenmode computed by our iterative algorithm is illustrated by Figure 3.4, which plots the magnitude $|P(\eta, \zeta)|$ of the pressure eigenfunction. This figure is qualitatively identical to Figure 8a of the Balachandar and Malik (1995) paper (notwithstanding the substantial discrepancy in reported eigenvalues). As anticipated, the instability is located squarely within the corner region proper, attaining its maximum magnitude on the bisector at $(\eta, \zeta) = (2.2, 2.2)$. It is largely unaffected by the adjacent blending boundary layer; this is to be expected, since the

laminar streamwise velocity therein asymptotes rapidly to the Blasius profile, which is inviscidly stable. As one exits the corner region, the eigenmode apparently decays at the asymptotic rate of

$$\exp[-\alpha(\eta+\zeta)] \qquad \text{for} \qquad \eta+\zeta \gg 1. \tag{3.19}$$

Unfortunately, we are unable to express full confidence in the above results. Though Figure 3.3 appears to provide compelling evidence of numerical convergence, we were unable to replicate and generalize these results. In fact, our iterative algorithm was liable to fail whenever applied to a very fine mesh ($h_1 \leq 0.05$). In any case, the pursuit of rigorous numerical convergence taxed the limits of available computing power. Eventually, we abandoned our FD-based algorithm in favour of Method 2.

3.4 Method 2 (Inviscid)

3.4.1 Outline

Method 2 follows that of Balachandar and Malik (1995). That is, the Rayleigh equation (3.9) for the perturbation pressure is discretized using a Chebyshev pseudospectral scheme, and the resulting generalised eigenvalue equation (3.11) is solved using the standard QZ algorithm. For validation purposes, we implement Method 2 in both Fortran 90 and Matlab, and experiment with several different far-field boundary conditions.

3.4.2 Details

For Method 2, we use an order-N Chebyshev pseudospectral (PS) scheme to discretize the Rayleigh equation over the domain $\mathcal{D}$ defined by (3.12). This well-known spectral scheme spans $\mathcal{D}$ with a non-uniform grid of $N{+}1 \times N{+}1$ collocation points (illustrated in Figure 3.5), and uses Lagrange interpolating polynomials of degree N to compute spatial derivatives. Consequently, the truncation error in computing any local derivative should be of order $O(\mathrm{e}^{-N})$, compared with $O(N^{-2})$ for the FD2 finite-difference scheme.

Version 1 of Method 2 was implemented in Fortran 90 code. Here, as in §3.3, we use the assumption of eigenfunction symmetry to shrink the problem to the working half-domain $\widetilde{\mathcal{D}}$ defined by (3.14), thereby reducing the number of working variables to approximately $\frac{1}{2}N^2$. The discretized system yields a generalised eigenvalue equa-

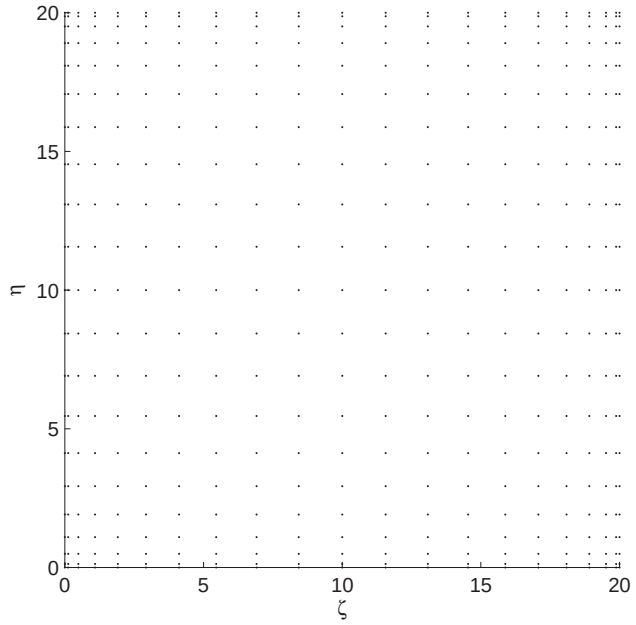

Figure 3.5: The mesh of collocation points associated with the Chebyshev pseudospectral (PS) scheme of Method 2, illustrated for the case of domain size $\zeta_{\max} = 20$ and spectral order $N = 20$.

tion of the form

$$\begin{bmatrix} A_{ii} & A_{ib} \\ A_{bi} & A_{bb} \end{bmatrix} \begin{bmatrix} \mathbf{p}_i \\ \mathbf{p}_b \end{bmatrix} = c \begin{bmatrix} B_{ii} & B_{ib} \\ 0 & 0 \end{bmatrix} \begin{bmatrix} \mathbf{p}_i \\ \mathbf{p}_b \end{bmatrix} \tag{3.20}$$

where the complex-valued vectors $\mathbf{p}_i$ and $\mathbf{p}_b$ denote interior and boundary values respectively of the eigenvector $\mathbf{p}$, and the second block row implements Neumann boundary conditions at $\eta = 0$ and $\zeta = \zeta_{\max}$. We transform (3.20) to an equivalent non-singular eigenvalue equation of the form

$$\widetilde{\mathbf{A}}\mathbf{p} = c\widetilde{\mathbf{B}}\mathbf{p} \qquad \text{where} \qquad \mathbf{p} \equiv \mathbf{p}_i \tag{3.21}$$

and the full matrices $\widetilde{\mathbf{A}}$ and $\widetilde{\mathbf{B}}$ are given by

$$\widetilde{\mathbf{A}} = A_{ii} - A_{ib}(A_{bb})^{-1}A_{bi}, \tag{3.22}$$

$$\widetilde{\mathbf{B}} = B_{ii} - B_{ib}(A_{bb})^{-1}A_{bi}. \tag{3.23}$$

The reduced eigenvalue equation (3.21) is then solved using the QZ algorithm, via a function call to the LAPACK routine `dggev`. The computational cost of this scheme nominally scales as $O(N^6)$, although in practice the observed computational time ('wall time') scaled as $O(N^k)$ where $k \approx 7.4$.

Version 2 of Method 2 was initially intended as a cross-check on Version 1. It was adapted from various Matlab codes published in Trefethen (2000), all of which

emphasize conciseness and flexibility; wherever possible, calculations are performed using whole-matrix operations, and numerical results are converted seamlessly to graphical output. A generalized eigenvalue equation is solved via a function call to `eig`, which interfaces directly with the above-mentioned Fortran routine `dggev`.

Version 2 yielded identical results to those of Version 1 in the case of Neumann far-field boundary conditions. Full agreement was obtained irrespective of whether eigenfunction symmetry was assumed, and whether the eigenvalue equation was singular or non-singular (thereby confirming that the QZ algorithm is numerically robust). Our results varied slightly, however, when the Neumann far-field boundary condition was swapped for a Robin condition of the form

$$\frac{\partial P}{\partial \zeta} = -\alpha P \qquad \text{at} \quad \zeta = \zeta_{\max} \tag{3.24}$$

or

$$\frac{\partial P}{\partial \rho} = -\alpha P \qquad \text{at} \quad \zeta = \zeta_{\max} \tag{3.25}$$

where ρ measures distance from the corner line, ie

$$\rho^2 = \eta^2 + \zeta^2. \tag{3.26}$$

The effect of this change was typically to change the third or fourth decimal place of the leading eigenvalue c_1. An examination of the structure of this eigenfunction confirmed that both forms of the Robin boundary equation are more natural than the Neumann condition. This is to be expected, since the Neumann condition attempts to confine the eigenfunction within an arbitrary finite domain.

3.4.3 Results

Figure 3.6 plots the leading eigenvalue c_1 as a function of spectral order N for the case of Neumann boundary conditions applied at $\zeta_{\max} = 20, 30$ and 40. Likewise, Figure 3.7 plots c_1 as a function of N for the case of Robin conditions at $\zeta_{\max} = 10$ and $\zeta_{\max} = 15$.

Our results are inconclusive, but suggest that the corner flow is inviscidly unstable, with a leading eigenvalue of $c_1 \approx 0.46 + 0.01\text{i}$ at $\alpha = 0.225$. (This value differs in the second decimal place from that of Balachandar and Malik (1995), namely $c_1 = 0.48 + 0.018\text{i}$ at $\alpha = 0.225$.) Unfortunately, our results for $\zeta_{\max} \geq 20$ show a wide degree of scatter, suggesting that the eigenmode cannot be adequately resolved without a prohibitively large spectral order ($N \gtrsim 100$). Reducing the domain size to $\zeta_{\max} = 10$ improves the spatial resolution and reduces the scatter of numerical results. At the same time, however, our results for $\zeta_{\max} = 10$ apparently show c_r

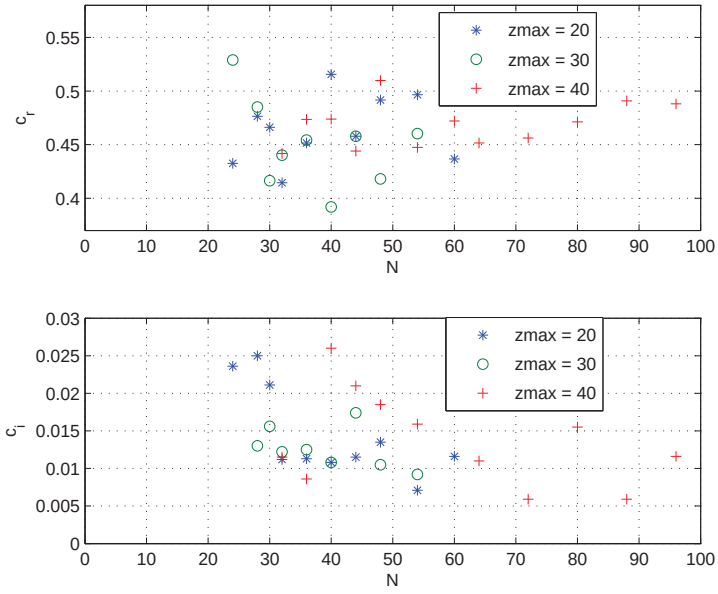

Figure 3.6: Results of Method 2 for the case of $\zeta_{\max} \geq 20$ and Neumann boundary conditions at $\zeta = \zeta_{\max}$. The upper and lower panels plot the real and imaginary parts respectively of the leading eigenvalue c_1 as a function of spectral order N and domain size $\zeta_{\max}$.

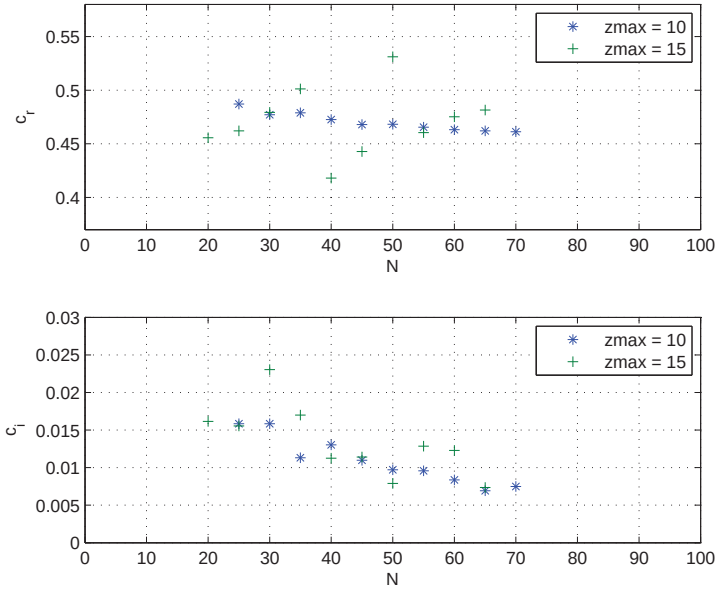

Figure 3.7: Results of Method 2 for the case of $\zeta_{\max} < 20$ and Robin boundary conditions at $\zeta = \zeta_{\max}$. As in Figure 3.6, the upper and lower panels show the real and imaginary parts respectively of the leading eigenvalue c_1.

and c_i decreasing with N — a warning that the eigenmode may be spurious. In any case, our results are at variance with those of Balachandar and Malik (1995), who report that parameter values of $N = 54$ and $\zeta_{\max} = 25$ are "adequate to provide well converged results".

3.5 Method 3 (Inviscid)

3.5.1 Outline

Our experience with Method 2 in §3.4.3 suggests that the key to numerical convergence lies in improving spatial resolution of the corner boundary layer. To this end, Method 3 introduces a coordinate mapping of the form

$$(\eta, \zeta) \;\Rightarrow\; (\widetilde{\eta}, \widetilde{\zeta}) \tag{3.27}$$

whose effect is to increase the proportion of collocation points falling within the boundary layer. In all other respects, however, Method 3 follows Version 2 of Method 2. That is, the transformed domain in the $(\widetilde{\eta}, \widetilde{\zeta})$ plane is discretized using a Chebyshev pseudospectral (PS) scheme; Robin conditions are applied at the far-field boundary; the discretized system is solved via the QZ algorithm; and the entire numerical scheme is implemented in Matlab code.

3.5.2 Details

Prior to applying the Chebyshev PS discretization, we 'expand' the boundary layers using the following coordinate mapping:

$$\widetilde{\eta}/\zeta_{\max} \;=\; f(\eta/\zeta_{\max}), \tag{3.28a}$$
$$\widetilde{\zeta}/\zeta_{\max} \;=\; f(\zeta/\zeta_{\max}), \tag{3.28b}$$

where

$$f(s;\, \sigma) \;=\; \frac{\log[1 + (\sigma - 1)s]}{\log \sigma} \tag{3.29}$$

and $\sigma > 1$ is an arbitrary constant. The mapping function f has the property that

$$0 \le s \le f(s) \le 1 \qquad \text{with equality iff} \quad s = 0 \quad \text{or} \quad s = 1. \tag{3.30}$$

The metric of this mapping is

$$\mathrm{d}\widetilde{\eta}/\mathrm{d}\eta \;=\; \mu(\eta/\zeta_{\max}), \tag{3.31a}$$
$$\mathrm{d}\widetilde{\zeta}/\mathrm{d}\zeta \;=\; \mu(\zeta/\zeta_{\max}), \tag{3.31b}$$

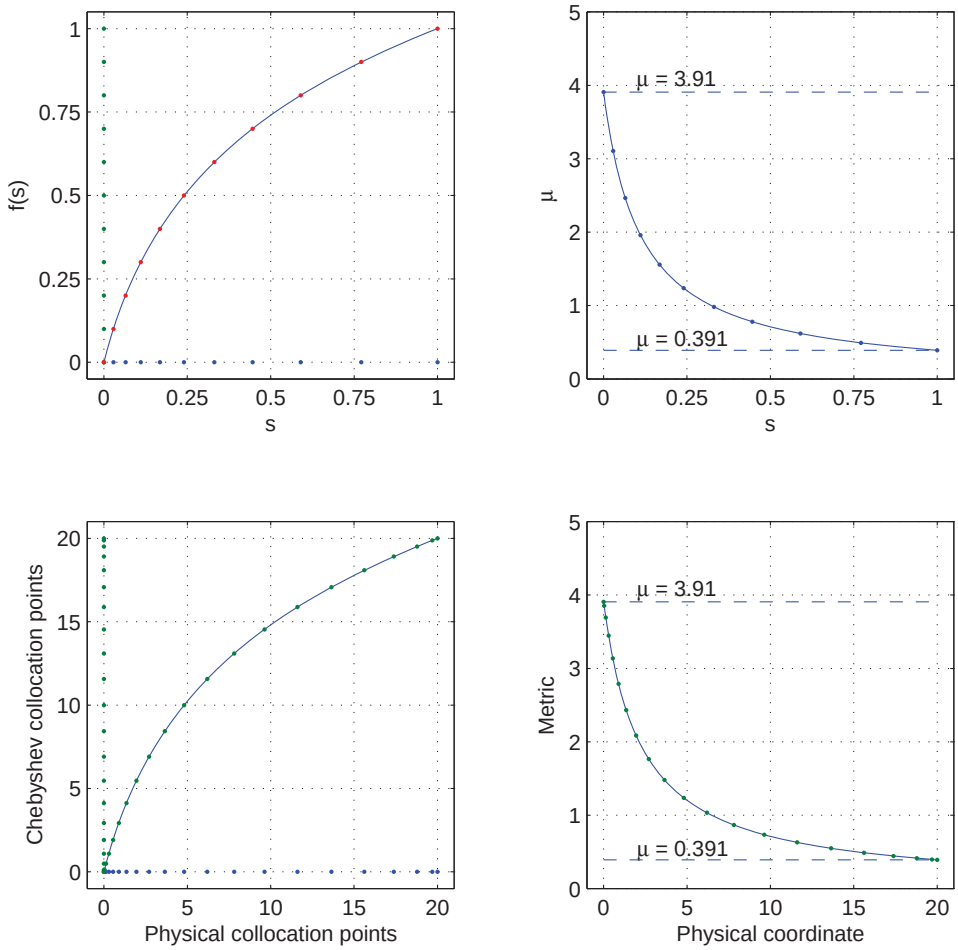

Figure 3.8: *Upper left:* The mapping function $f(s;\sigma)$ defined by (3.29) for the case $\sigma = 10$. Left-clustered points in physical space (indicated by dot-markers on the horizontal axis) are mapped by f to equispaced points in computational space (dot-markers on vertical axis). *Upper right:* The metric $\mu(s) \equiv f'(s)$ of this map. *Lower left:* Schematic representation of the spatial discretization for Method 3 (§3.5.2). The dot-markers on the vertical axis correspond to Chebyshev PS collocation points of polynomial order $N = 20$ for parameter values of $\sigma = 10$ and $\zeta_{\max} = 20$. *Lower right:* The metric $\mathrm{d}\widetilde{\eta}/\mathrm{d}\eta$ and $\mathrm{d}\widetilde{\zeta}/\mathrm{d}\zeta$ of the coordinate map shown at lower-left.

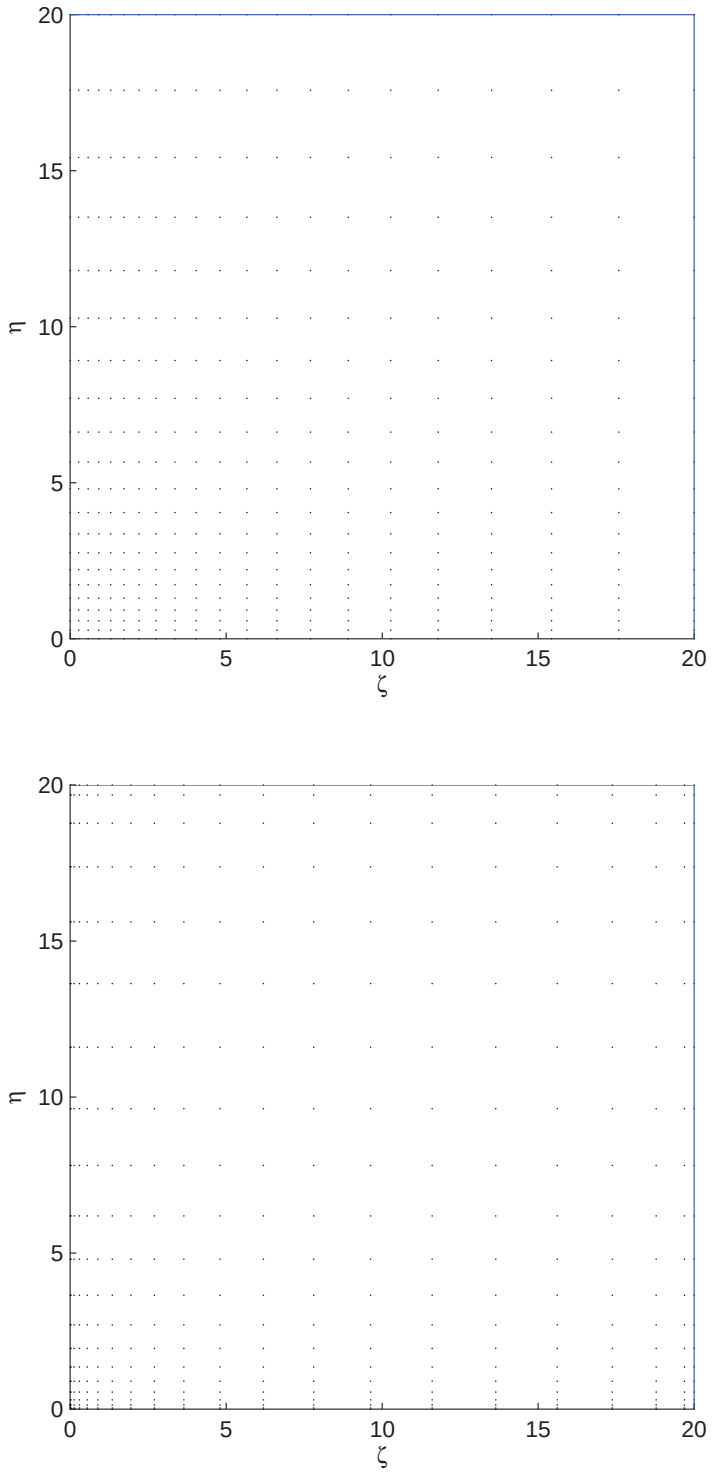

Figure 3.9: *Upper figure:* Equispaced grid based on the mapping function shown in Figure 3.8 for the parameters $\sigma = 10$, $\zeta_{\max} = 20$ and $N = 20$. *Lower figure:* Chebyshev pseudospectral grid corresponding to the same parameter set.

where

$$\mu(s) \equiv f'(s) \tag{3.32}$$

is a decreasing function of s with the property that

$$\frac{\mu(0)}{\mu(1)} = \sigma, \tag{3.33}$$

indicating that σ can be interpreted as the *stretch ratio* of the mapping. This property is illustrated in Figures 3.8 and 3.9 for a stretch ratio of $\sigma = 10$, in conjunction with a Chebyshev pseudospectral scheme of order $N = 20$ for $\zeta_{\max} = 20$. Since $f(0.25) \approx 0.5$ in this case, it follows that approximately half of the 1D collocation points fall within the boundary layer:

$$\zeta_i < 5, \quad \widetilde{\zeta}_i \lesssim 10 \qquad \text{for} \qquad i \lesssim N/2, \quad \sigma = 10, \quad \zeta_{\max} = 20.$$

Consequently, approximately one-quarter (ie $\frac{1}{2} \times \frac{1}{2}$) of the 2D collocation points fall within the inner corner region:

$$\eta_i < 5 \quad \text{and} \quad \zeta_j < 5 \qquad \text{for} \qquad i, j \lesssim N/2, \quad \sigma = 10, \quad \zeta_{\max} = 20.$$

3.5.3 Results

Figure 3.10 plots the leading eigenvalue c_1 as computed by Method 3 with the following parameter values:

$$\zeta_{\max} = 10, \quad \sigma = 10, \quad 20 \leq N \leq 70, \tag{3.34a}$$

$$\zeta_{\max} = 15, \quad \sigma = 12, \quad 20 \leq N \leq 70, \tag{3.34b}$$

$$\zeta_{\max} = 20, \quad \sigma = 15, \quad 20 \leq N \leq 80. \tag{3.34c}$$

The results for the cases $\zeta_{\max} = 10$ and $\zeta_{\max} = 15$ show poor convergence with respect to spectral order N. The results for $\zeta_{\max} = 20$ are more consistent; however, the downward trend in c_i indicates that the eigenmode may be spurious. Qualitatively similar results were obtained when the stretch parameter σ was varied.

Once again, we are compelled to report inconclusive results and insufficient computing power. It is therefore time to attempt the full viscous instability equations. In theory this represents an even more ambitious undertaking, since it involves up to four flow variables, as opposed to the single flow variable P of the Rayleigh equation. Unlike the Rayleigh equation, however, the viscous equations are amenable to the Arnoldi algorithm for efficient extraction of the leading eigenvalues. Consequently, the four-equation viscous system may prove more tractable than its inviscid counterpart.

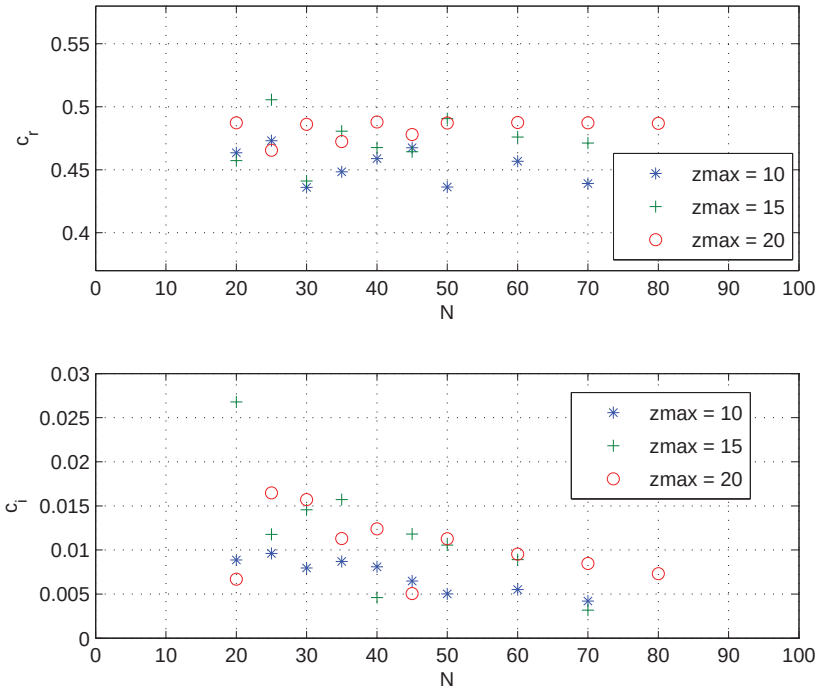

Figure 3.10: Results of Method 3, plotting the real and imaginary parts of c_1 as a function of spectral order N and domain size $\zeta_{\max}$.

3.6 Method 4 (Viscous)

3.6.1 Outline

Method 4 increases the numerical efficiency of Methods 2 and 3 by using the Arnoldi algorithm to extract only the leading eigenvalues. Furthermore, the viscous stability equations (3.5) are used in place of the inviscid (Rayleigh) equation. The reason for this is that the Arnoldi algorithm is not directly applicable to a generalised eigenvalue problem (GEVP) of the form

$$\mathbf{A}\mathbf{q} = c\,\mathbf{B}\mathbf{q} \tag{3.35}$$

where the matrices $\mathbf{A}$ and $\mathbf{B}$ are not symmetric (or Hermitian). In principle, one could invert the $\mathbf{B}$ matrix generated by the Rayleigh equation, and proceed to apply the Arnoldi algorithm to the resulting standard eigenvalue problem of the form

$$\widetilde{\mathbf{A}}\mathbf{p} = c\,\mathbf{p}. \tag{3.36}$$

In practice, however, it is more efficient to work with the viscous equations, which yield a diagonal $\mathbf{B}$ matrix. Each component of the full eigenfunction Q defined by

$$Q(\eta, \zeta) \equiv (U, V, W, P) \tag{3.37}$$

is discretized using either the standard pseudospectral (PS) scheme of Method 2 (§3.4) or the modified PS scheme of Method 3 (§3.5). In either case, one must perform some pre-processing as follows. The pressure and boundary values are eliminated to yield a non-singular standard eigenvalue problem of the form

$$\widetilde{\mathbf{A}}\mathbf{u} = \mathrm{i}\alpha c\,\mathbf{u} \tag{3.38}$$

where $\mathbf{u}$ denotes non-boundary values of the reduced eigenfunction

$$\mathbf{U}(\eta,\zeta) \equiv (U,V,W). \tag{3.39}$$

Unfortunately, this transformation step (which also destroys matrix sparsity) is even more expensive than the Arnoldi algorithm itself. Nevertheless, the net effect is to reduce the computational cost by an order of magnitude relative to the equivalent QZ algorithm.

Method 4 provides good resolution of the leading eigenvalues for a spectral order of either $N \approx 50$ or $N \approx 35$ (depending on whether the spectral discretization is standard or modified using coordinate mapping). Given that the computation cost scales as $O(N^6)$ in both cases, a reduction in N from 50 to 35 provides an efficiency dividend of approximately one order of magnitude. To put these figures into perspective, resolution of a single eigenvalue is feasible on a desktop computer at a spectral order of $N \lesssim 60$; at $N = 50$ it becomes feasible to conduct a limited parametric study, including estimation of the stability threshold of the inviscid mode; and at $N = 40$, a thorough study of the viscous modes becomes feasible.

3.6.2 Details

Our method is very similar to that of Parker and Balachandar (1999). The composite eigenfunction Q is defined by (3.37) and governed by the viscous stability equations (3.5). As in Methods 1 to 3, we reduce computational costs eightfold by exploiting the symmetry of Q with respect to the corner bisector:

$$U(\zeta,\eta) = \pm U(\eta,\zeta), \tag{3.40a}$$
$$P(\zeta,\eta) = \pm P(\eta,\zeta), \tag{3.40b}$$
$$V(\zeta,\eta) = \pm W(\eta,\zeta), \tag{3.40c}$$

where the plus and minus signs correspond respectively to symmetry and antisymmetry of the mode with respect to the corner bisector. Positive symmetry is almost invariably invoked in practice, since the inviscid mode occurs only under this symmetry configuration; furthermore, antisymmetric viscous modes are invariably found

to be more stable (and hence less important) than their symmetric counterparts. We have also performed some computations without symmetry assumptions, the results of which demonstrated to our satisfaction the non-existence of fully asymmetric modes.

The viscous stability equations must be solved subject to the no-slip boundary conditions

$$U = V = W = 0 \qquad \text{at} \qquad \eta = 0. \tag{3.41}$$

Unfortunately there is no natural boundary condition for the perturbation pressure P. This situation clearly differs from that of the inviscid Rayleigh equation, where a Neumann condition on P ensures zero normal flow through the corner wall. Noting, however, the role of pressure in maintaining a divergence-free flow, we use the continuity equation to derive an implicit pressure boundary condition as follows. Evaluated in the limit $\eta \to 0$, the continuity equation specifies quadratic decay of the normal velocity in the vicinity of the wall:

$$V_\eta = 0 \qquad \text{at} \qquad \eta = 0. \tag{3.42}$$

The viscous stability equations must be solved subject to far-field boundary conditions at the artificial domain limit $\zeta = \zeta_{\max}$. These conditions may be of Neumann, Robin or spanwise-periodic type:

$$\text{Neumann:} \qquad \partial Q/\partial\zeta = 0 \qquad \text{at} \qquad \zeta = \zeta_{\max}\,, \tag{3.43a}$$

$$\text{Robin:} \qquad \partial Q/\partial\zeta = -\alpha Q \qquad \text{at} \qquad \zeta = \zeta_{\max}\,, \tag{3.43b}$$

$$\text{Periodic:} \qquad \partial Q/\partial\zeta = \mathrm{i}\beta Q \qquad \text{at} \qquad \zeta = \zeta_{\max}\,, \tag{3.43c}$$

where β is a real-valued parameter. Either Neumann and Robin conditions may be employed in the case of the inviscid mode, which is localised within the corner region and decays to zero in the spanwise direction (albeit slowly). For the viscous modes, which do not decay significantly in the spanwise direction, it is advisable to apply the periodic condition (also known as the Sommerfeld radiation condition). The parameter β in (3.43c), in conjunction with the streamwise wavenumber α, determines the spatial orientation of the disturbance wave. Thus, $\beta = 0$ corresponds to a standing wave propagating parallel to the corner line, whereas $\beta < 0$ and $\beta > 0$ correspond respectively to oblique waves directed towards and away from the corner. A compelling visual illustration of this phenomenon appears in Figures 16 and 19 of the Parker and Balachandar (1999) paper.

The viscous-stability governing equations (3.5), together with the above symmetry and boundary conditions, are discretized in the (η, ζ) domain as in Method 2

or Method 3. In either case one obtains the GEVP (3.35); it may be conveniently expressed in the block-matrix form

$$\begin{bmatrix} \mathbf{A}_{11} & \mathbf{A}_{12} \\ \mathbf{A}_{21} & \mathbf{0} \end{bmatrix} \begin{bmatrix} \mathbf{u} \\ \mathbf{p} \end{bmatrix} = \mathrm{i}\alpha c \begin{bmatrix} \mathbf{I} & \mathbf{0} \\ \mathbf{0} & \mathbf{0} \end{bmatrix} \begin{bmatrix} \mathbf{u} \\ \mathbf{p} \end{bmatrix} \tag{3.44}$$

where the eigenvector $\mathbf{u}$ represents a discretization of $\mathbf{U}(\eta, \zeta)$. Prior to enforcement of bisector symmetry, the left-hand matrix in (3.44) is of approximate dimension $4N^2$ and contains $O(N^3)$ non-zero elements; we generate it efficiently in Matlab using a sequence of sparse-matrix operations. In the second step of the algorithm, we drop the zero-valued wall velocities and 'fold in' all Q entries corresponding to $\zeta = \zeta_{\max}$ (temporarily retaining the non-zero wall values of P) to yield a modified GEVP of the form

$$\begin{bmatrix} \widetilde{\mathbf{A}}_{11} & \widetilde{\mathbf{A}}_{12} \\ \widetilde{\mathbf{A}}_{21} & \mathbf{0} \end{bmatrix} \begin{bmatrix} \widetilde{\mathbf{u}} \\ \widetilde{\mathbf{p}} \end{bmatrix} = \mathrm{i}\alpha c \begin{bmatrix} \mathbf{I} & \mathbf{0} \\ \mathbf{0} & \mathbf{0} \end{bmatrix} \begin{bmatrix} \widetilde{\mathbf{u}} \\ \widetilde{\mathbf{p}} \end{bmatrix}. \tag{3.45}$$

Enforcement of symmetry constitutes the third step, while the fourth step is the most expensive in terms of computational cost. Following the example of Parker and Balachandar (1999), we pre-multiply the second block-matrix row in (3.45) by the first:

$$\left(\widetilde{\mathbf{A}}_{21}\widetilde{\mathbf{A}}_{11}\right)\widetilde{\mathbf{u}} + \left(\widetilde{\mathbf{A}}_{21}\widetilde{\mathbf{A}}_{12}\right)\widetilde{\mathbf{p}} = \mathbf{0}. \tag{3.46}$$

It now follows that

$$\widetilde{\mathbf{p}} = -\left[\left(\widetilde{\mathbf{A}}_{21}\widetilde{\mathbf{A}}_{12}\right)^{-1}\widetilde{\mathbf{A}}_{21}\widetilde{\mathbf{A}}_{11}\right]\widetilde{\mathbf{u}} \tag{3.47}$$

whence

$$\widetilde{\mathbf{A}}\widetilde{\mathbf{u}} = \mathrm{i}\alpha c\,\widetilde{\mathbf{u}} \tag{3.48}$$

where

$$\widetilde{\mathbf{A}} = \left[\mathbf{I} - \widetilde{\mathbf{A}}_{12}(\widetilde{\mathbf{A}}_{21}\widetilde{\mathbf{A}}_{12})^{-1}\widetilde{\mathbf{A}}_{21}\right]\widetilde{\mathbf{A}}_{11}. \tag{3.49}$$

The fifth and final step is to invoke the Arnoldi eigensolver via the Matlab routine `eigs` (which in turn invokes the LAPACK Arnoldi eigensolver). In order to avoid spurious eigenvalues, one must supply (via the `opts.p` flag in `eigs`) a rough estimate of the leading eigenvalue(s); the effect of this is to activate the shift-and-invert algorithm prior to the Arnoldi algorithm proper. One may also specify the number of Lanczos working vectors for the Arnoldi algorithm; we find that fifty Lanczos vectors ensures numerical convergence of the leading eigenvalues.

Since $\widetilde{\mathbf{A}}$ is a full matrix, its storage requirements scale as $O(N^4)$; it occupies approximately 50 megabytes of memory at $N = 35$ and 200 MB at $N = 50$. Parker and Balachandar devised a vectorization strategy whereby the complete matrix is not

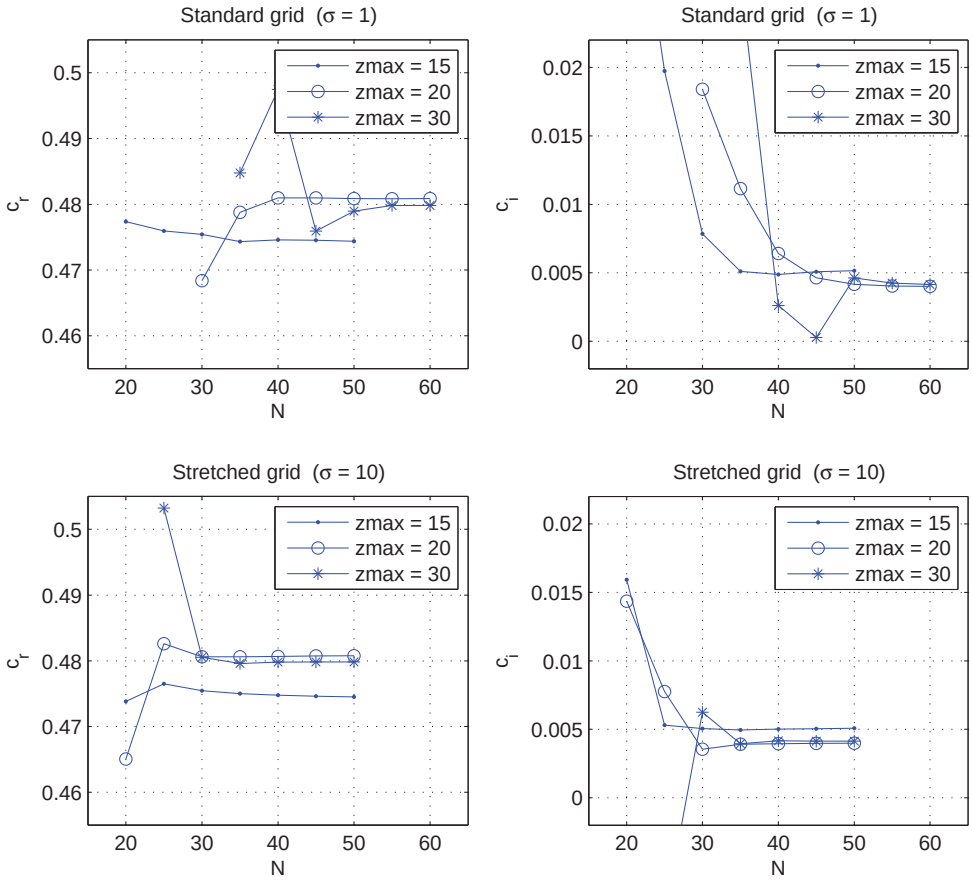

Figure 3.11: *Top:* Numerical convergence of the inviscid eigenvalue $c_0 \equiv c_\mathrm{r} + \mathrm{i}c_\mathrm{i}$ for Method 4 as a function of spectral order N and domain size ζ_max at $\sigma = 1$ (ie without coordinate mapping). The upper-left and upper-right panels correspond respectively to c_r and c_i for parameter values of $Re = 10^5$ and $\alpha = 0.2$. *Bottom:* As above, but using coordinate mapping with stretch parameter $\sigma = 10$.

stored in memory at any one time; instead, all computations are based on eigenvectors and one-dimensional matrix operators, whose size scales as $O(N^2)$. No further details are supplied, however, and it is not entirely clear how this strategy guaranteed a divergence-free flow in the absence of explicit values for the perturbation pressure.

3.6.3 Results: Inviscid mode

The inviscid mode occurs only under positive spatial symmetry, and is found to be unique up to streamwise wavenumber α. Thus, the inviscid eigenvalue

$$c_0 \equiv c_\mathrm{r} + \mathrm{i}c_\mathrm{i} \tag{3.50}$$

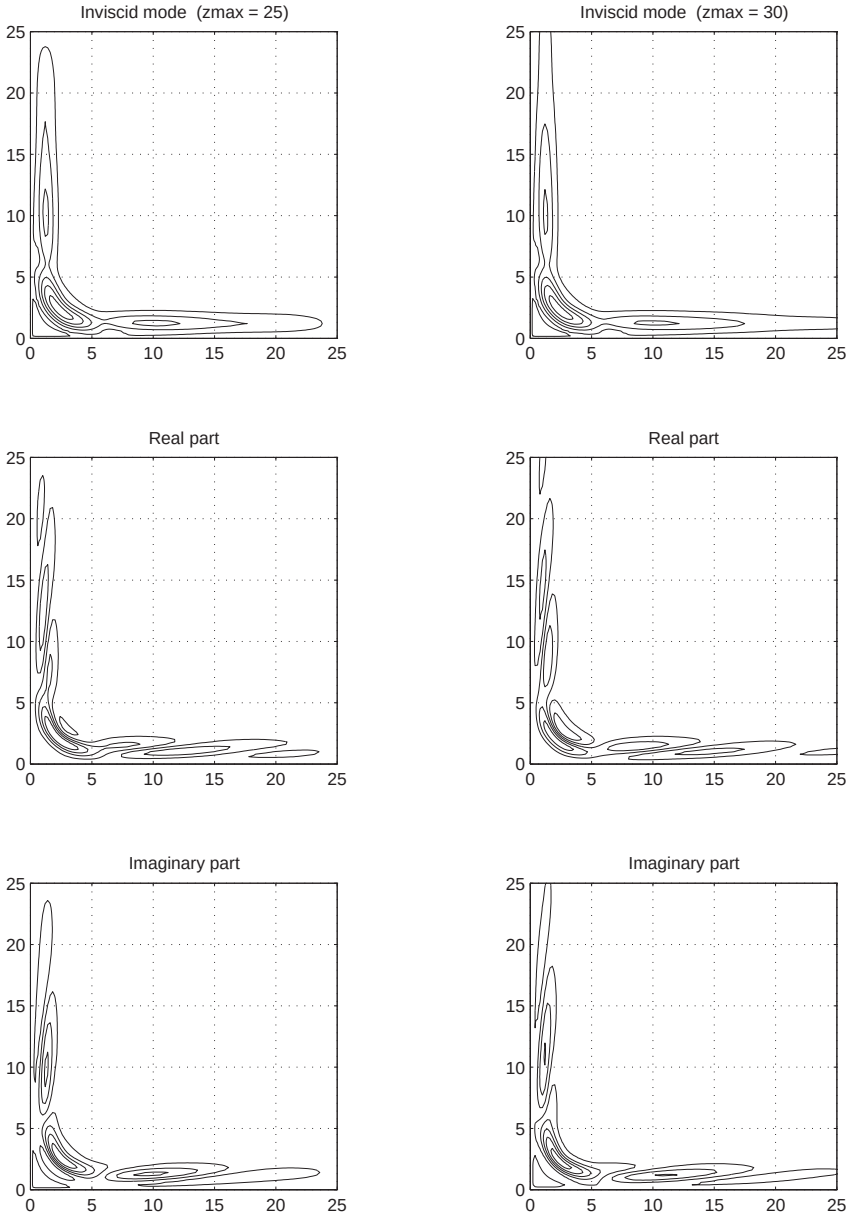

Figure 3.12: Contour plots of streamwise velocity $U(\eta, \zeta)$ for the inviscid mode, computed using domain sizes of $\zeta_{\max} = 25$ *(left)* and $\zeta_{\max} = 30$ *(right)* for parameter values of $Re = 10^5$ and $\alpha = 0.2$. The upper, middle and lower figures correspond respectively to the amplitude $|U|$, real part $U_{\rm r}$ and imaginary part $U_{\rm i}$. The eigenmode is normalized so that $|U| \leq 1$ everywhere, and the contour spacing is 0.2 throughout. The contour levels for $|U|$ *(top)* are 0.1, 0.3, 0.5, 0.7 and 0.9. Heavy and light contours for $U_{\rm r}$ and $U_{\rm i}$ *(middle and bottom)* correspond respectively to positive and negative values.

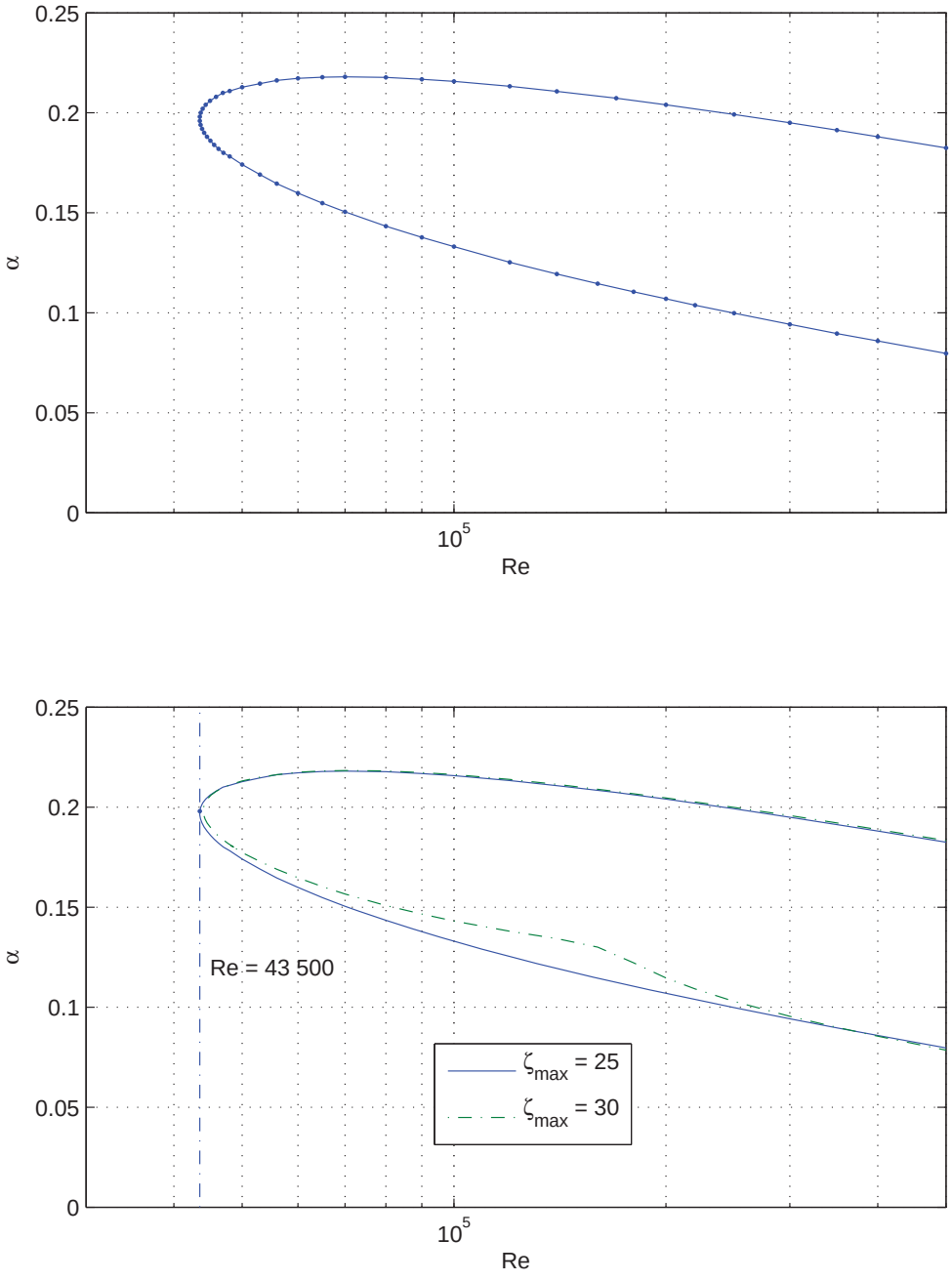

Figure 3.13: *Upper figure:* Neutral-stability curve in (Re, α) space for the inviscid mode (computed using a domain size of $\zeta_{\max} = 25$), with data points indicated by dot markers. The horizontal scale is logarithmic, running from $Re = 30\ 000$ to $Re = 500\ 000$. The critical point is found to be $(Re, \alpha) = (43\ 500, 0.198)$. *Lower figure:* Inviscid neutral-stability curves computed using $\zeta_{\max} = 25$ (solid) and $\zeta_{\max} = 30$ (dashed), with data points omitted for clarity.

is fully defined by the two-dimensional parameter space (α, Re).

Our numerical data for the inviscid mode exhibits very satisfactory convergence. The effect of switching between Robin and Neumann domain boundary conditions was typically to alter the fourth or fifth decimal of c_0. The influences of domain size $\zeta_{\max}$, spectral order N and stretch factor σ are illustrated in Figure 3.11 for the case of the inviscid mode with wavenumber $\alpha = 0.2$ and Reynolds number $Re = 10^5$. Three-decimal convergence of c_0 is attained at $N = 45$ for $\sigma = 1$ (ie in the absence of coordinate mapping), or at $N = 30$ for $\sigma = 10$, based on a domain size $\zeta_{\max}$ of 20–25. Four-decimal accuracy, required for accurate evaluation of stability thresholds, is typically attained at an approximate spectral order of

$$N \;=\; [10 \log_{10}(Re)] - N_0 \tag{3.51}$$

with $N_0 \approx 10$ for parameter values of $\sigma = 10$ and $20 \leq \zeta_{\max} \leq 25$. As α is decreased below ≈ 0.15, however, the convergence rates in N and $\zeta_{\max}$ decrease. This is to be expected, since the spanwise decay of the eigenmode is governed by α as follows:

$$O(\mathrm{e}^{-\alpha\zeta}) \qquad \text{for} \qquad \zeta \gg 1. \tag{3.52}$$

The cross-sectional structure of the inviscid mode is illustrated by Figure 3.12, which plots the magnitude $|U|$ and phase $(U_\mathrm{r}, U_\mathrm{i})$ of the streamwise perturbation velocity in the (η, ζ) plane. As expected, the instability is strongest within the corner boundary layer, which is characterised by a strongly inflectional profile for the streamwise component of the laminar flow. However, the inviscid mode also has a highly non-trivial structure within the blending boundary layer, comprising a regular sequence of interlaced vortices. Interestingly, these vortex structures are not visible in the blending-layer envelope function $|U|$, which decays monotonically as a function of spanwise distance from the corner line.

We are now in a position to estimate a critical Reynolds number for this laminar flow. Figure 3.13 plots the neutral-stability curve in (Re, α) space based on domain sizes of $\zeta_{\max} = 25$ and $\zeta_{\max} = 30$. The corresponding critical values are

$$Re_c = 4.35 \times 10^4 \quad \text{at} \quad \alpha_c = 0.197 \qquad (\zeta_{\max} = 25), \tag{3.53a}$$

$$Re_c = 4.40 \times 10^4 \quad \text{at} \quad \alpha_c = 0.198 \qquad (\zeta_{\max} = 30). \tag{3.53b}$$

A stability threshold of $Re_c = 44\ 000$ strongly suggests that the flow is inviscidly unstable, being approximately half that of 2D Blasius flow (which is known to be inviscidly stable).

Our findings are strikingly different from those of Parker and Balachandar (1999), who reported that the inviscid mode is stable "below a Reynolds number of about 5×

10^5." This anomalous result may indicate problems with the authors' vectorization strategy outlined above in §3.6.2, as Galionis and Hall (2005) suggest in §3.5 of their paper:

> The reason for this discrepancy might be that ... a Poisson equation for pressure was solved for the calculation of each new vector-entry to the Arnoldi matrix, for which boundary conditions had to be imposed on the walls. Since it is in this region that the inviscid mode lies, it becomes evident that the related eigenvalue can be very sensitive to the boundary conditions and inaccurate results are obtained if improper boundary conditions are imposed.

They describe their own approach as follows:

> In the present work the use of a fully staggered grid allowed us not to set any boundary conditions for the pressure disturbance and its values were obtained exclusively from the numerical solution.

Thus, both Parker and Balachandar (1999) and Galionis and Hall (2005) differ from us in their treatment of pressure boundary conditions. Galionis and Hall (2005) find that the inviscid mode becomes unstable somewhere in the range $100K < Re < 150K$, but did not conduct an exhaustive study of its properties:

> The inviscid modes [sic] have not been treated to a large extent, since preliminary results indicated that their [sic] growth rate was not as high as one of the most unstable of the viscous modes.

The neutral curves in Figure 3.13 feature downward-sloping upper and lower branches for $Re \gtrsim 10^5$. No significant convergence or divergence of the branches is evident for $Re \leq 5 \times 10^5$. The results for $\zeta_{\max} = 25$ and $\zeta_{\max} = 30$ show excellent agreement except in the lower-middle section of the curve, where domain convergence becomes problematic. Somewhat surprisingly, the neutral curve for the lower $\zeta_{\max}$ value is noticeably more regular, and hence is probably more accurate. In any case, the two curves re-converge at $Re \approx 2.5 \times 10^5$.

3.6.4 Results: Viscous modes

The viscous modes are non-unique, and may have either positive or negative symmetry across the corner bisector. However, our discussion will be limited to symmetric modes, since they are invariably less stable (and hence more interesting) than their antisymmetric counterparts.

For any given parameter value (Re, α, β), our eigensolver returns the inviscid mode (henceforth labelled by $j = 0$) plus a sequence of pseudo-discrete viscous

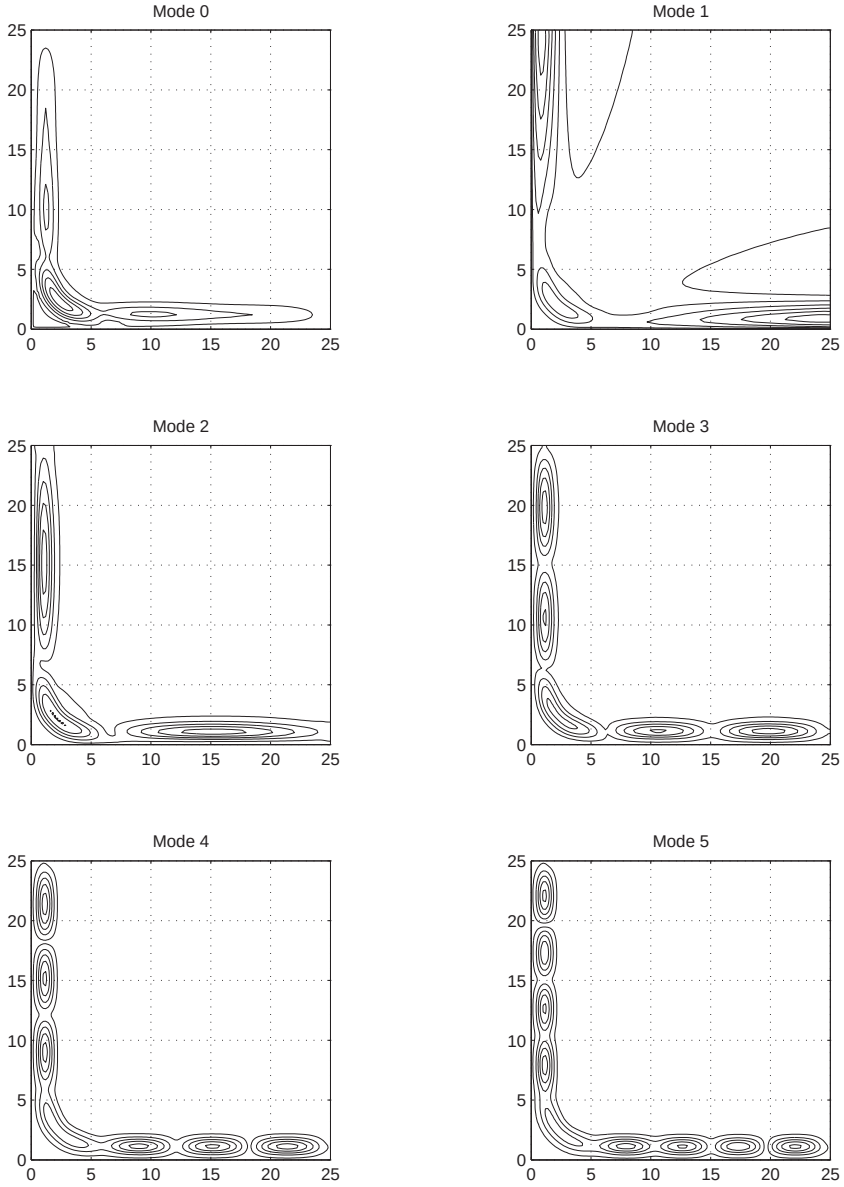

Figure 3.14: The inviscid mode ($j = 0$) and leading viscous modes ($j = 1, ..., 5$) plotted in the (η, ζ) plane. (Owing to space constraints, we display only the magnitude $|U_j|$ of the streamwise velocity for each mode.) Parameter values throughout are $\zeta_{\max} = 25$, $Re = 10^5$, $\alpha = 0.2$ and $\beta = 0$.

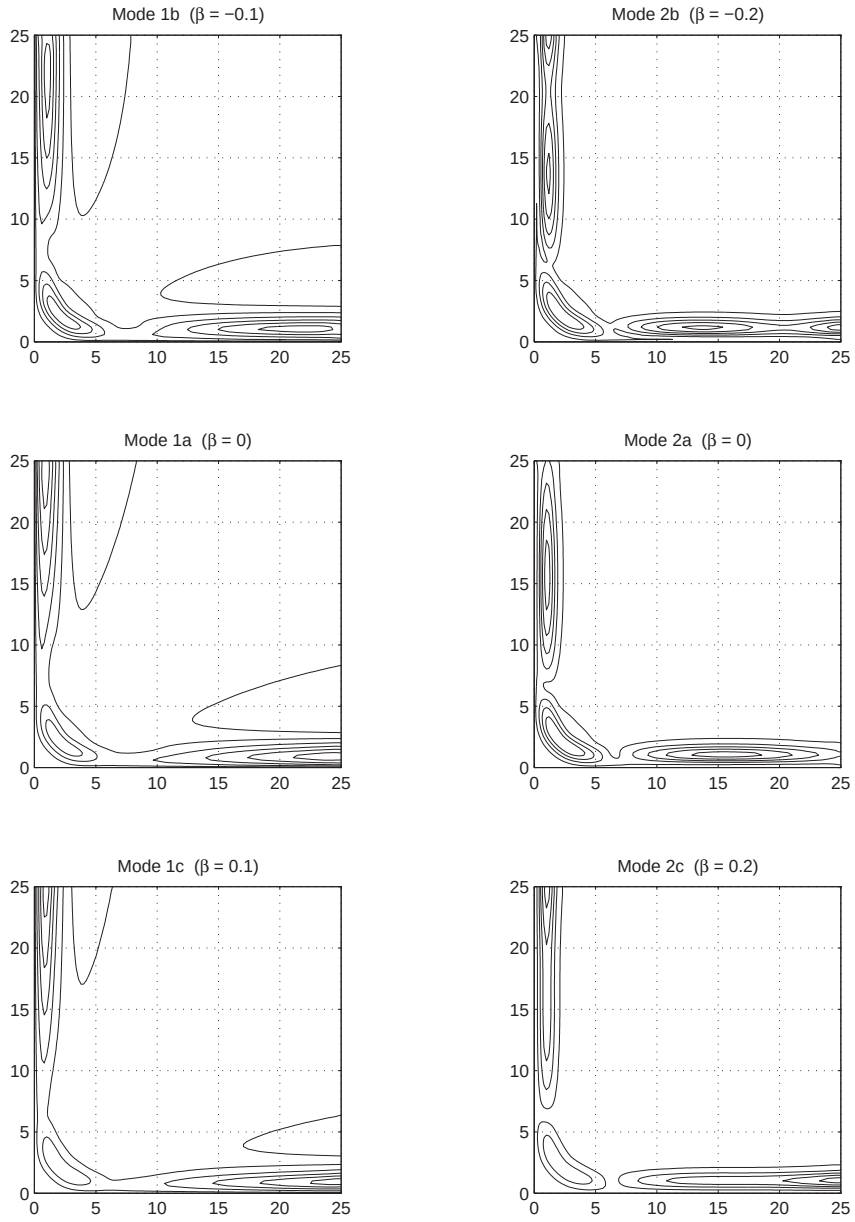

Figure 3.15: *Left:* Viscous Mode 1, computed for spanwise wavenumbers of $\beta = -0.1$ *(top left)*, $\beta = 0$ *(middle left)*, and $\beta = +0.1$ *(bottom left)*. *Right:* Mode 2 for $\beta = -0.2$ *(top right)*, $\beta = 0$ *(middle right)*, and $\beta = +0.2$ *(bottom right)*. Parameter values throughout are $Re = 10^5$, $\alpha = 0.2$ and $\zeta_{\max} = 25$.

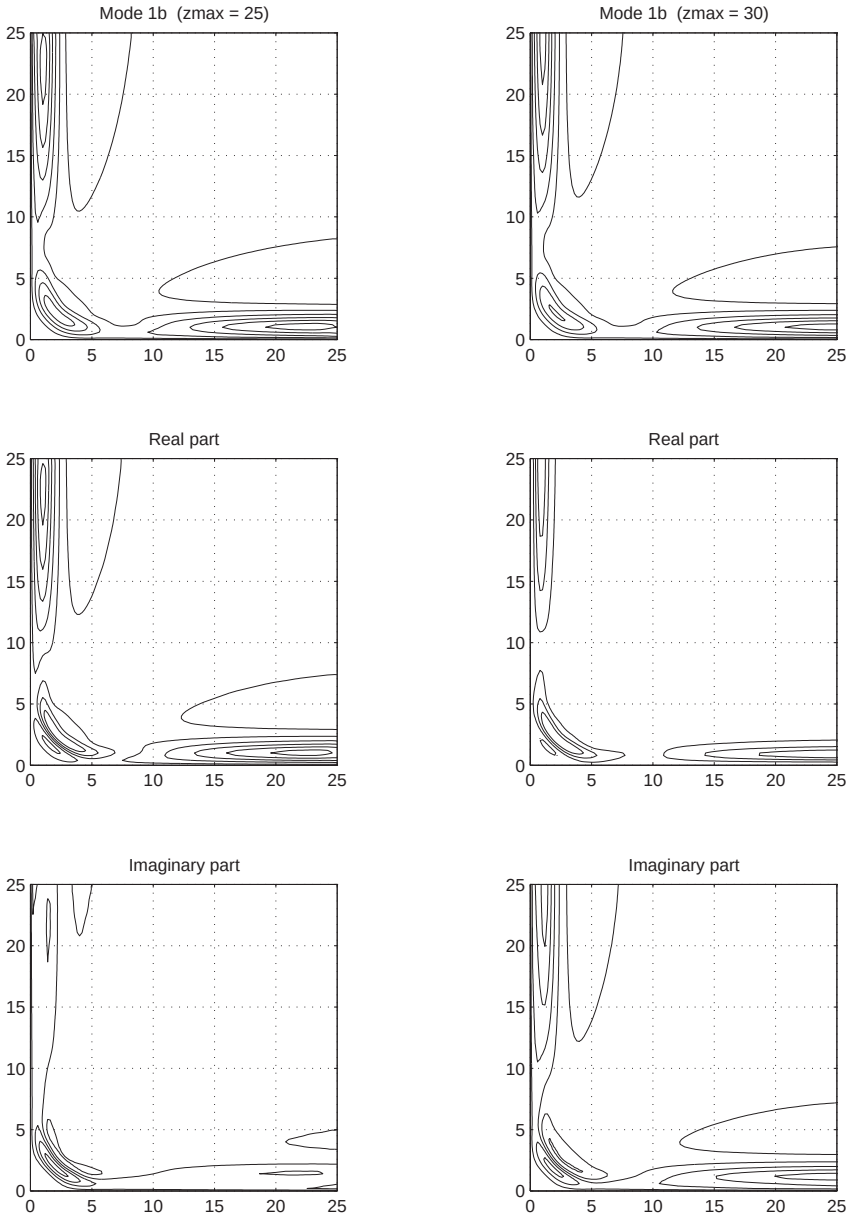

Figure 3.16: Mode 1, computed with domain sizes of $\zeta_{\max} = 25$ *(left)* and $\zeta_{\max} = 30$ *(right)*. The upper, middle and lower figures in each case correspond to $|U|$, $U_{\rm r}$ and $U_{\rm i}$ respectively. Parameter values throughout are $\beta = -0.08$, $Re = 10^5$ and $\alpha = 0.2$.

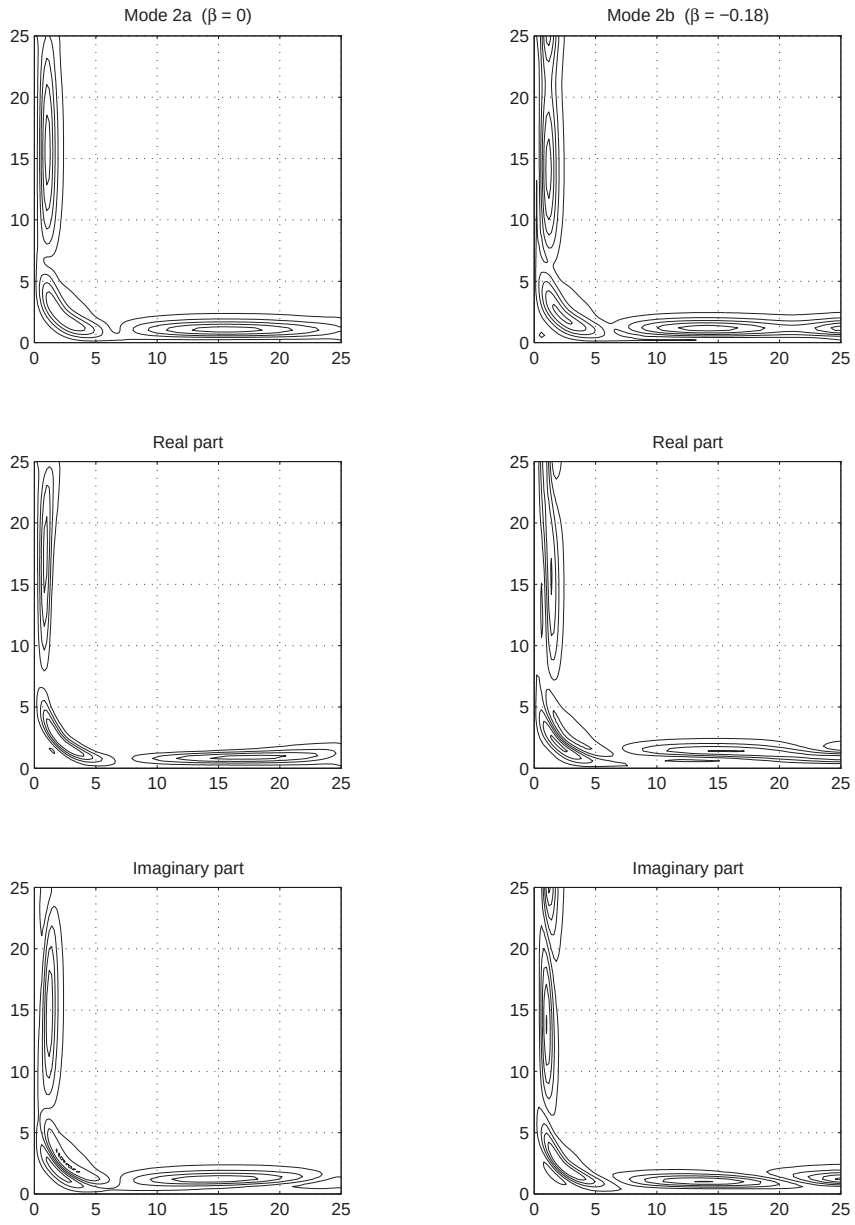

Figure 3.17: Mode 2, computed for $\beta = 0$ *(left)* and $\beta = -0.18$ *(right)*; upper, middle and lower figures correspond to $|U|$, $U_{\rm r}$ and $U_{\rm i}$ respectively. Parameter values throughout are $\zeta_{\max} = 25$, $Re = 10^5$ and $\alpha = 0.2$.

Mode	$\zeta_{\max}$	$Re_c \times 10^3$	α_c	β_c
0 (inviscid)	25	43.5	0.197	0
	30	44.0	0.198	0
	35	$\approx 500.$	0.20	0
1a (streamwise)	25	127.5	0.244	0
	30	115.5	0.246	0
	35	115.	0.244	0
1b (oblique)	25	94.5	0.245	-0.090
	30	90.5	0.248	-0.075
	35	86.	0.237	-0.110
1c (oblique)	35	215.	0.230	+0.13
2a (streamwise)	25	295.	0.16	0
	30	260.	0.18	0
2b (oblique)	25	65.5	0.172	-0.19
	30	76.5	0.198	-0.16
	35	106.	0.21	-0.20
2c (oblique)	35	Stable for all Re		+0.24

Table 3.1: The critical point $(Re, \alpha, \beta)_c$ for the inviscid mode and the two leading viscous modes. Results listed for $\zeta_{\max} = 35$ are those reported by Parker and Balachandar (1999).

modes ($j = 1, 2, \ldots$). Figure 3.14 presents a typical set of results from a single program run, plotting the streamwise magnitude $|U_j|$ for $j \leq 5$. Figure 3.15 plots $|U_1|$ and $|U_2|$ for three distinct values of the propagation wavenumber β. The real and imaginary parts of U_1 and U_2 are plotted in Figures 3.16 and 3.17 respectively. In addition, Figure 3.16 shows that the viscous eigenfunctions are domain-dependent (the left- and right-hand panels correspond to $\zeta_{\max} = 25$ and $\zeta_{\max} = 30$ respectively), while Figure 3.17 reveals a subtle β-dependence in eigenmode structure. The leading eigenvalues $\{c_j\}$ are plotted in Figures 3.18 and 3.19 as functions of β for selected $\zeta_{\max}$ values. Figure 3.20 plots the spanwise wavenumber β_j^* corresponding to the stability minimum. Table 3.1 lists the critical Reynolds number $(Re, \alpha, \beta; j)_c$ for modes $j = 1$ and $j = 2$ (obtained by a rigorous procedure of numerical optimization over (Re, α, β) space). Table 3.2 summarizes the stability minima $\{\beta_{cj}\}$ and maxima $\{\beta_j^*\}$ for $j = 1, 2$ and 3. (The non-negative transverse wavenumbers $\{\gamma_j\}$ shown in this table will be defined below.) Table 3.3 lists the unstable range of streamwise wavenumber α for $j = 0, 1, 2$ for the two cases $Re = 10^5$ and $Re = 2 \times 10^5$. Figure 3.21 presents neutral-stability curves in (Re, α) space for $j = 1$ and $j = 2$ at selected β values. Figures 3.22 and 3.23 present composite neutral curves for

Mode	$\zeta_{\max}$	β_c	β^*	$\widetilde{\gamma}$	γ_c	γ^*
1	25	-0.09	+0.15	0.09	0.09	0.11
	30	-0.075	+0.14	0.07	0.07	0.08
	35	-0.11	+0.13	0.11	0.12	0.14
2	25	-0.19	+0.27	0.175	0.26	0.29
	30	-0.16	+0.21	0.14	0.18	0.20
	35	-0.20	+0.24	0.225	0.31	0.35
3	25	-0.27	+0.4	0.35	0.59	0.78
	30	-0.26	+0.37	0.27	0.45	0.57
	35	-0.28	+0.38	0.34	0.58	0.72

Table 3.2: The stability minimum $\beta_c < 0$ and stability maximum $\beta^* > 0$ for each of the three leading viscous modes. Results for $\zeta_{\max} = 35$ are those of Parker and Balachandar (1999). For Modes 1 and 2, β_c values are optimized over α, whereas results for Mode 3 and for β^* are approximate and generally refer to $\alpha = 0.2$. For comparison, the table also provides approximate data $(\widetilde{\gamma}, \gamma_c, \gamma^*)$ on the spanwise length scales of the blending-layer vortex structures in each mode. In particular, the non-negative wavenumber $\widetilde{\gamma}$ corresponds to the spanwise wavelength measured in the (η, ζ) plane, whereas γ_c and γ^* are measured transverse to the directions (α, β_c) and (α, β^*) of wave propagation.

$j = 0, 1, 2$ with respect to $(\alpha,\, c_{\rm r}, \omega)$, where ω is the temporal frequency defined by

$$\omega \;=\; \alpha c_{\rm r}. \tag{3.54}$$

Finally, Figure 3.24 plots the growth rate

$$\kappa \;=\; \alpha c_{\rm i} \tag{3.55}$$

at near-optimal values of α for $j = 0, 1, 2$.

The discrete viscous modes described above are, in fact, illusory. A hint of this appears in Figures 3.18 to 3.20, which show that the viscous eigenvalues converge incompletely as a function of $\zeta_{\max}$ (notwithstanding rapid convergence in spectral order N, comparable to that of the inviscid eigenvalue c_0). Indeed, the eigenmode plots of Figures 3.14 to 3.17 are domain-dependent. For example, Figure 3.14 depicts Mode 1 as possessing approximately one half-vortex within the indicated blending layer, defined for present purposes in domain-dependent terms by

$$\zeta^* < \zeta < \zeta_{\max} \tag{3.56}$$

where the empirical constant

$$\zeta^* \approx 7 \tag{3.57}$$

Mode	$\zeta_{\max}$	β	$Re = 10^5$		$Re = 2 \times 10^5$	
			α_1	α_2	α_1	α_2
0 (inviscid)	25	0	0.133	0.216	0.107	0.204
	30	0	0.143	0.216	0.115	0.205
	35	0	stable		stable	
1a (streamwise)	25	0	stable		0.185	0.277
	30	0	stable		0.179	0.283
	35	0	stable		0.172	0.28
1b (oblique)	25	-0.090	0.224	0.261	0.149	0.286
	30	-0.075	0.222	0.271	0.160	0.288
	35	-0.110	0.185	0.278	0.138	0.288
2b (oblique)	25	-0.19	0.104	0.241	0.073	0.256
	30	-0.16	0.130	0.246	0.084	0.266
	35	-0.20	stable		0.125	0.252

Table 3.3: The range $\alpha_1 < \alpha < \alpha_2$ of unstable wavenumbers of each of the leading eigenmodes, shown for the two cases $Re = 10^5$ and $Re = 2 \times 10^5$. Results listed for $\zeta_{\max} = 35$ are those of Parker and Balachandar (1999), and are accurate to within $\Delta\alpha = 0.005$.

denotes the effective size of the inner corner region (which interrupts the spanwise periodicity of the viscous modes). The higher modes in Figure 3.14 apparently possess $j-1$ vortices ($j \geq 2$) within the truncated blending layer defined by (3.56). Equivalently, Mode 1 corresponds to approximately one-quarter of a spanwise wavelength, and higher modes to $\frac{1}{2}(j-1)$ of wavelengths[1]. This phenomenon is induced by the periodic domain boundary condition (3.43c), ie

$$\partial Q/\partial\zeta \;=\; \mathrm{i}\beta Q \qquad \text{at} \qquad \zeta = \zeta_{\max}\,, \tag{3.58}$$

whose secondary effect is to enforce

$$\partial|Q|/\partial\zeta \;=\; 0 \qquad \text{at} \qquad \zeta = \zeta_{\max}. \tag{3.59}$$

Thus, the viscous modes are not truly discrete; rather, they are defined by the continuous four-dimensional parameter space $(Re, \alpha, \beta, \gamma)$, where γ is a non-negative transverse wavenumber describing the spanwise length scale of the mode. The role of the domain parameter $\zeta_{\max}$ is now clear: it effectively collapses the continuous spectrum $\gamma \in \mathbf{R}^+$ down to a discrete pseudo-spectrum $\{\,\gamma_j\,\}$. For our results with

[1]Slightly different results are reported by Parker and Balachandar (1999) for the viscous modes with $\zeta_{\max} = 35$. In this case, Mode j corresponds to approximately j vortices or $j/2$ spanwise wavelengths for all $j > 0$.

$\beta = 0$, this is given by

$$\gamma \approx \tfrac{1}{2}\pi/(\zeta_{\max} - \zeta^*) \qquad \text{for} \quad j = 1, \tag{3.60a}$$

$$\gamma \approx (j-1)\pi/(\zeta_{\max} - \zeta^*) \qquad \text{for} \quad j = 2, 3, \ldots . \tag{3.60b}$$

For oblique modes, the formulae (3.60) define the *apparent* transverse length scale $\{\widetilde{\gamma}_j\}$ as viewed in the (η, ζ) plane, rather than the physical spectrum $\{\gamma_j\}$ measured transverse to the direction (α, β) of wave propagation. In general, therefore,

$$\widetilde{\gamma} \leq \gamma \qquad \text{with equality iff} \quad \beta = 0. \tag{3.61}$$

More precisely, since the propagation angle θ relative to the corner line is given by

$$\tan\theta \;=\; \beta/\alpha, \tag{3.62}$$

it follows that

$$\gamma/\widetilde{\gamma} \;=\; \sec\theta \;=\; \sqrt{1 + (\beta/\alpha)^2} \tag{3.63}$$

where $\widetilde{\gamma}$ is specified by (3.60).

Ideally, $\zeta_{\max}$ should be treated as a surrogate for the physical parameter γ. In practice, however, it would be impractical[2] to conduct a thorough survey of the four-dimensional parameter space $(Re, \alpha, \beta, \zeta_{\max})$. It is also difficult to ensure true independence between the two parameters β and γ, which interact through the domain boundary condition. In any case, this boundary condition inevitably introduces some local distortion into the eigenmode, especially in the case of strongly-oblique modes (which deviate significantly from standing-wave configurations). We will therefore continue to treat the viscous modes as quasi-discrete; where possible, however, we present results for at least two different $\zeta_{\max}$ values. Discrepancies in data based on $\zeta_{\max}$ are thus natural and inevitable, since they correspond to slightly different physical modes. This will be most noticeable for data on stability limits, since the critical Reynolds number is an extremely sensitive function of the eigenvalue.

Having clarified the nature of the viscous modes, we now examine their stability characteristics. In the special case of streamwise modes (ie for $\beta = 0$, as in Figure 3.14), the stability of the modes matches their order of appearance. Thus, Mode 0 (inviscid) is the least stable, followed respectively by Mode 1 ($Re_c = 115K$), then Mode 2 ($Re_c = 260K$), and so on. Hereafter, therefore, we focus almost exclusively on the oblique viscous modes. These are highly sensitive to the spanwise

[2] Apart from the issue of computational cost, we are effectively limited to $\zeta_{\max} \leq 30$ by the accuracy of the laminar-flow data available to us. For this reason Tables 3.1, 3.2 and 3.3 draw on published data of Parker and Balachandar (1999) for the case of $\zeta_{\max} = 35$.

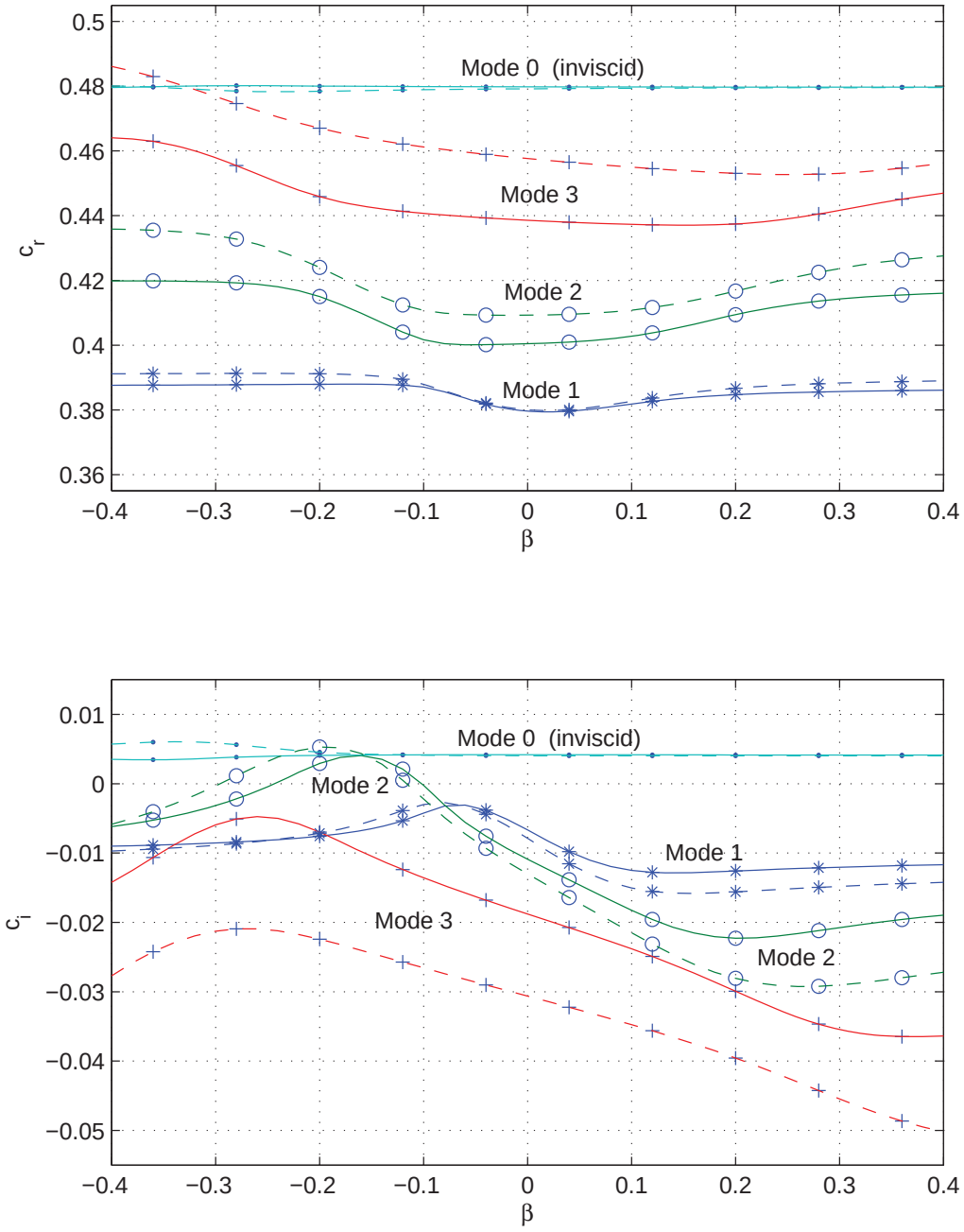

Figure 3.18: The eigenvalues $\{ c_j \}$ of Mode j for $j = 0, 1, 2, 3$ (indicated by dots, asterisks, circles and crosses respectively), plotted as functions of spanwise wavenumber β. Solid and dashed curves correspond to $\zeta_{\max}$ values of 30 and 25 respectively. Each curve interpolates raw data spaced at intervals of $\Delta\beta = 0.02$. Parameter values throughout are $Re = 10^5$ and $\alpha = 0.2$.

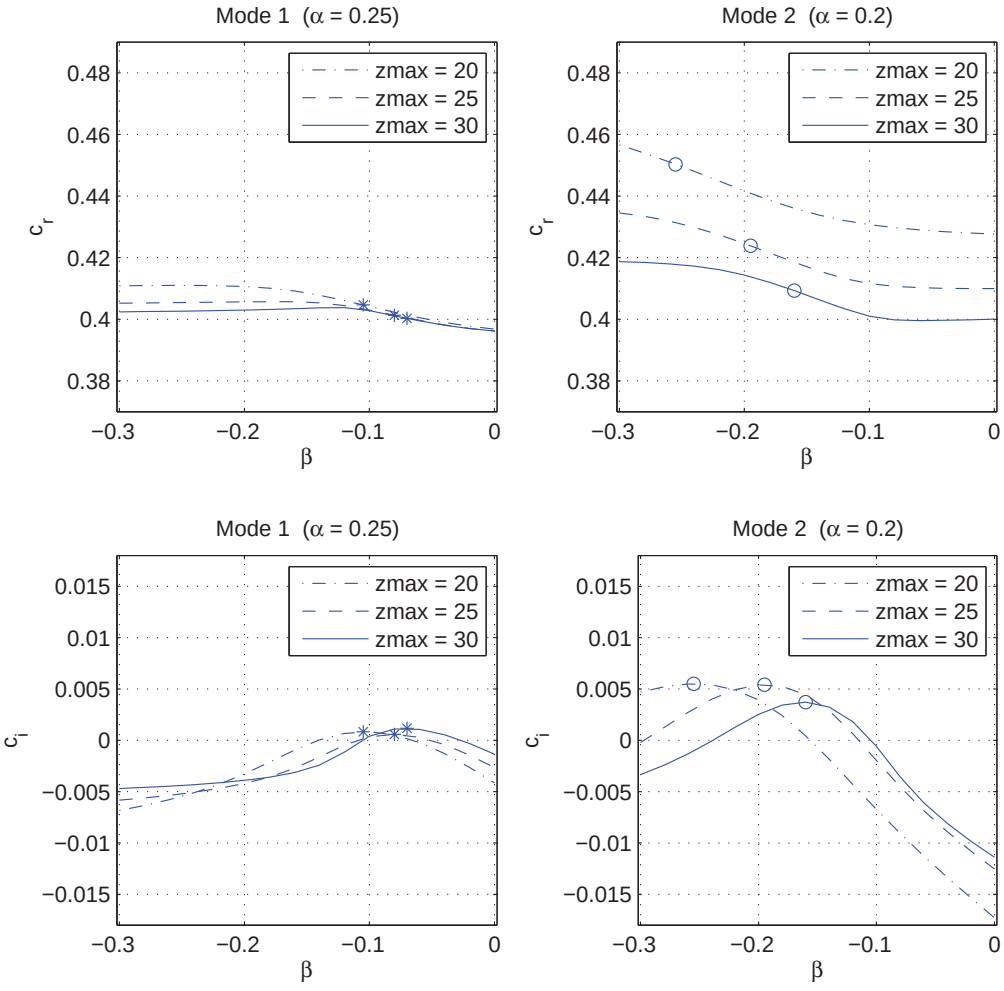

Figure 3.19: *Upper-left and lower-left:* The eigenvalue c_1 of Mode 1b, plotted as a function of $\beta \leq 0$ for parameter values of $Re = 10^5$, $\alpha = 0.25$, and $\zeta_{\max} = 20$, 25 and 30. The asterisks indicate the critical wavenumber β_c for each $\zeta_{\max}$ value (estimated to within $\Delta\beta = 0.005$ using cubic-spline interpolation of raw data for $\Delta\beta = 0.02$). *Upper-right and lower-right:* The eigenvalue c_2 of Mode 2b for $Re = 10^5$, $\alpha = 0.2$ and $\zeta_{\max} = \{20, 25, 30\}$, with β_c indicated by circle markers.

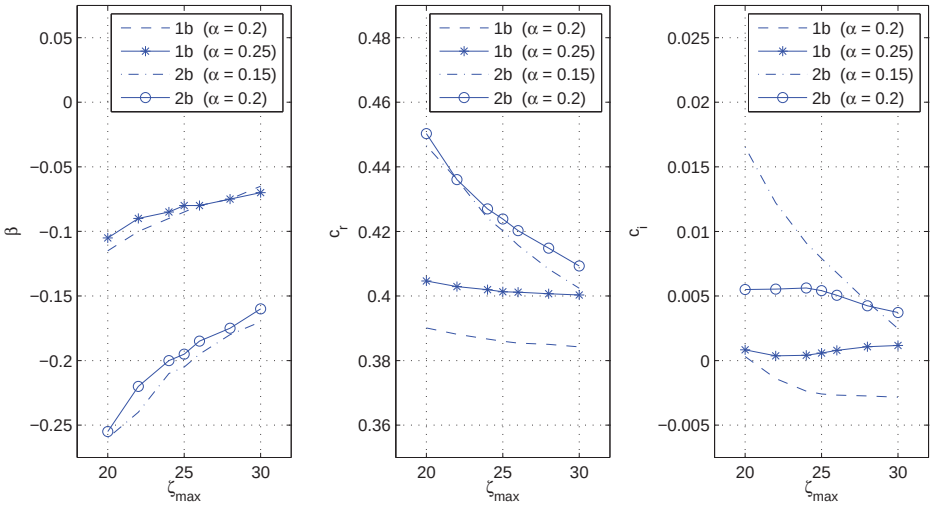

Figure 3.20: *Left:* The critical spanwise wavenumber β_{cj} for $j = 1$ and $j = 2$, plotted as a function of α and $\zeta_{\max}$ for $Re = 10^5$. The asterisk ($j = 1$) and circle ($j = 2$) markers correspond to $\zeta_{\max}$ values of 20, 22, 24, 25, 26, 28 and 30. *Centre and right:* The eigenvalues c_1 and c_2 corresponding to the wavenumbers $\beta = \beta_{cj}$ shown at left.

wavenumber β; in general, a given mode is much more stable as an outgoing disturbance ($\beta > 0$) than as an incoming ($\beta < 0$) or streamwise ($\beta = 0$) disturbance. Over the range of β values indicated in Figures 3.18 to 3.19, the imaginary part $c_{\rm i}$ of a viscous eigenvalue satisfies the inequalities

$$c_{\rm i}(\beta) < c_{\rm i}(0) < c_{\rm i}(-\beta) \qquad \text{for} \qquad 0 < \beta < 0.4, \tag{3.64a}$$

$$\partial c_{\rm i}/\partial\beta < 0 \qquad \text{for} \qquad \beta_c < \beta < \beta^*, \tag{3.64b}$$

where

$$\epsilon_j = O(10^{-1}) \qquad \text{is a positive constant.} \tag{3.65}$$

The critical wavenumber β_c is negative, satisfying

$$\beta_c \approx -\frac{j}{12} \qquad \text{for} \quad \zeta_{\max} = 30, \quad j = 1, 2, 3, \tag{3.66}$$

whereas the stability maximum $\beta^* > 0$ is positive and slightly larger in magnitude:

$$\beta^* = (1 + \epsilon)|\beta_c|. \tag{3.67}$$

The three cases $\beta = 0$, $\beta < 0$ and $\beta > 0$ will henceforth be denoted by the labels a, b and c respectively. The real parts of the three leading viscous eigenvalues satisfy the inequality

$$c_{r1} < c_{r2} < c_{r3} < c_{r0}. \tag{3.68}$$

In general, Mode 1b is found to be most active at relatively high α values ($0.2 \lesssim \alpha \lesssim 0.28$), whereas Mode 2b is most active for $0.15 \lesssim \alpha \lesssim 0.2$ (see Table 3.3 and Figure 3.22). However, Mode 2b is active over a much wider α range than either Mode 0 or Mode 1b.

The above results are in qualitative agreement with those of Parker and Balachandar (1999), but show significant quantitative disagreement. For example, their values for $|\beta_c|$ and β^* at $j = 1, 2, 3$ are uniformly larger than ours. This is not surprising, however, since their eigenmodes have uniformly smaller spanwise length scales (recall that their results show j vortices for $\zeta^* < \zeta < \zeta_{\max} = 35$, whereas our results show $max\{j-1, \frac{1}{2}\}$ vortices for $\zeta_{\max} = 25, 30$). We believe, therefore, that these numerical discrepancies have a sound physical basis. Further support for our hypothesis is provided by the pooled data of Table 3.2 (which reveals a strong correlation between γ, $|\beta_c|$ and β^* across all $\zeta_{\max}$ values) and Figure 3.20 (which indicates that $|\beta_c|$ is a decreasing function of $\zeta_{\max}$ for $20 \leq \zeta_{\max} \leq 30$ and $j = 1, 2$). The latter may at first appear contradictory to the above hypothesis (given our suggestion that $|\beta_c|$ *increases* between $\zeta_{\max} = 30$ and 35), but is fully consistent with the observed trends in β and γ.

The most striking point of difference between our results and those of Parker and Balachandar (1999) relates to the leading mode of instability. Parker and Balachandar (1999) identify the leading instability as Mode 1b, for which they report a critical Reynolds number of

$$Re_c = 86\ 000 \qquad \text{at} \qquad j = 1, \quad \alpha = 0.237, \quad \beta = -0.11 \quad (\zeta_{\max} = 35), \tag{3.69}$$

compared with $Re_c = 106K$ for Mode 2b and $Re_c \approx 500K$ for Mode 0. However, our results favour Mode 0 and Mode 2b, as the following data indicates:

$$j = 0: \quad Re_c = 43\ 500 \quad \text{at} \quad \alpha = 0.197, \quad \beta = 0 \qquad (\zeta_{\max} = 25), \tag{3.70a}$$

$$j = 1: \quad Re_c = 90\ 500 \quad \text{at} \quad \alpha = 0.248, \quad \beta = -0.075 \quad (\zeta_{\max} = 30), \tag{3.70b}$$

$$j = 2: \quad Re_c = 65\ 500 \quad \text{at} \quad \alpha = 0.172, \quad \beta = -0.19 \qquad (\zeta_{\max} = 25). \tag{3.70c}$$

In fact, the true limit for Mode 2b may be well below the nominal value of $Re_c = 65\ 500$, since Figures 3.18 and 3.19 represent c_{i2} as a decreasing function of $\zeta_{\max}$ over the indicated range ($20 \leq \zeta_{\max} \leq 30$). Incidentally, the opposite trend is observed for Mode 3b in Figure 3.18. Intriguingly, there is a strong physical resemblance between Mode 2b at $20 \leq \zeta_{\max} < 25$, Mode 3b at $\zeta_{\max} = 30$, and Mode 0 (inviscid; $\zeta_{\max}$ arbitrary). In particular, their respective vortex structures exhibit similar spanwise length scales and off-square orientations. This in turn leads us to speculate that the true viscous-stability threshold may actually coincide with the inviscid limit $Re_c = 43\ 500$.

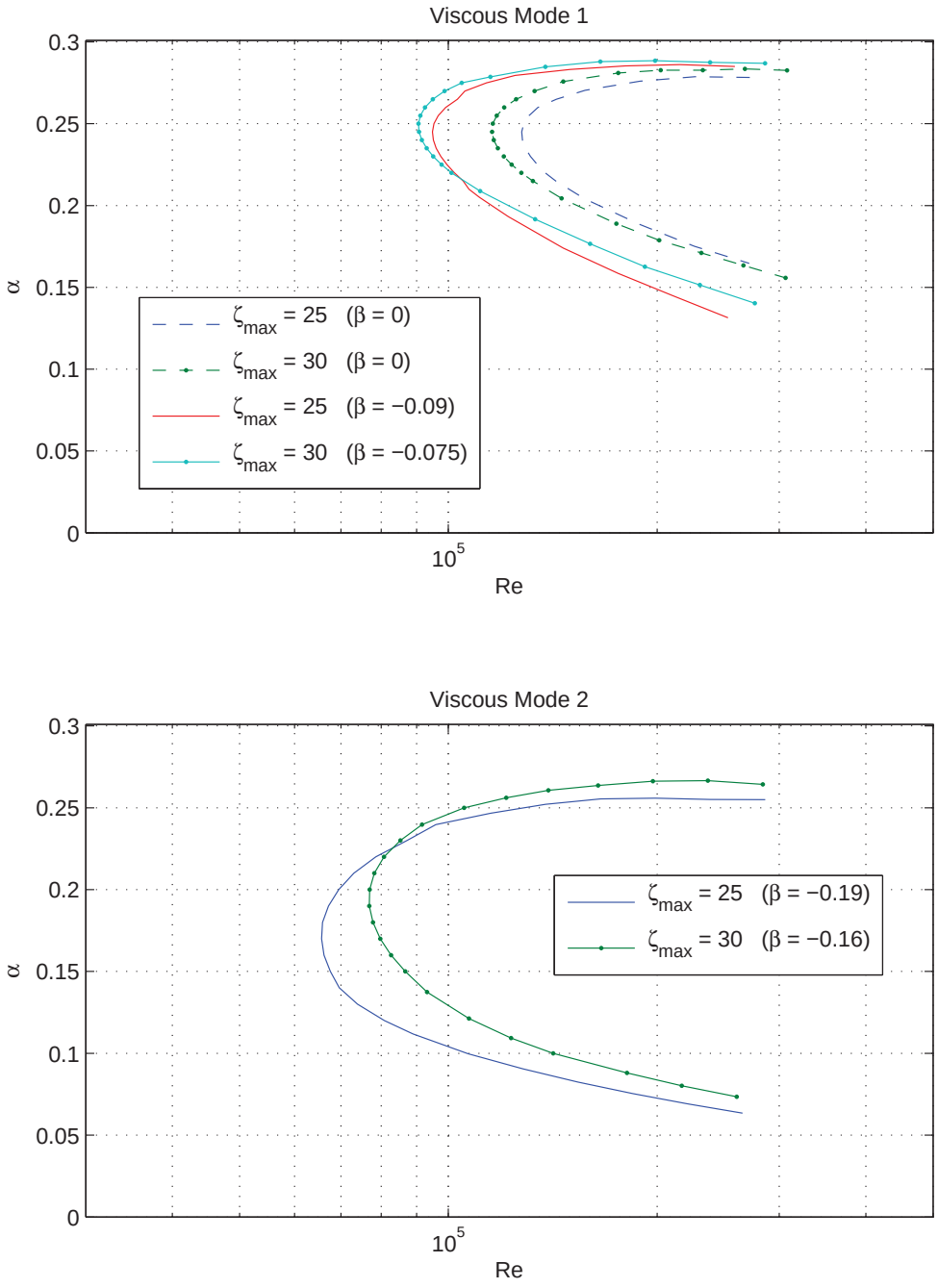

Figure 3.21: *Upper figure:* Neutral-stability curves for Mode 1a (dashed curves, $\beta = 0$) and Mode 1b (solid curves, with $\beta = \beta_c < 0$ as indicated). Dot-markers indicate raw data for $\zeta_{\max} = 30$; curves without data markers correspond to $\zeta_{\max} = 25$. *Lower figure:* Neutral-stability curves for Mode 2b at $\beta = \beta_c$ with $\zeta_{\max} = 30$ (with dot-marked data) and $\zeta_{\max} = 25$ (unmarked curve).

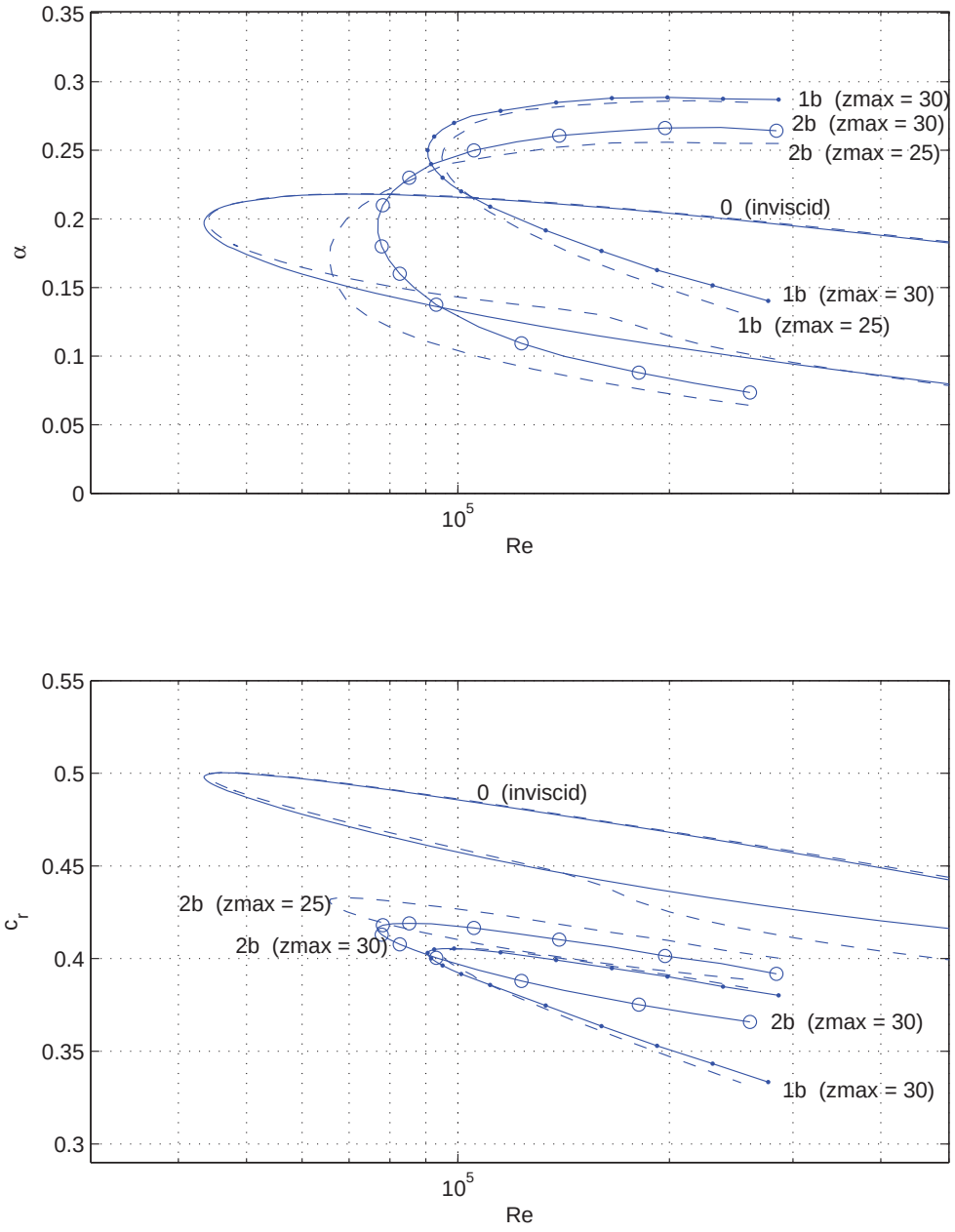

Figure 3.22: *Upper figure:* Montage of the neutral-stability curves for Mode 0 (solid curve for $\zeta_{\max} = 25$; dashed for $\zeta_{\max} = 30$), Mode 1b (dashed for $\zeta_{\max} = 25$; solid with dot-markers for $\zeta_{\max} = 30$), and Mode 2b (dashed for $\zeta_{\max} = 25$; solid with circle markers for $\zeta_{\max} = 30$). Some data markers have been omitted in the interests of clarity. *Lower figure:* The corresponding neutral-stability curves in $(Re, c_{\rm r})$ space, where $c_{\rm r}$ denotes the real part of the eigenvalue c.

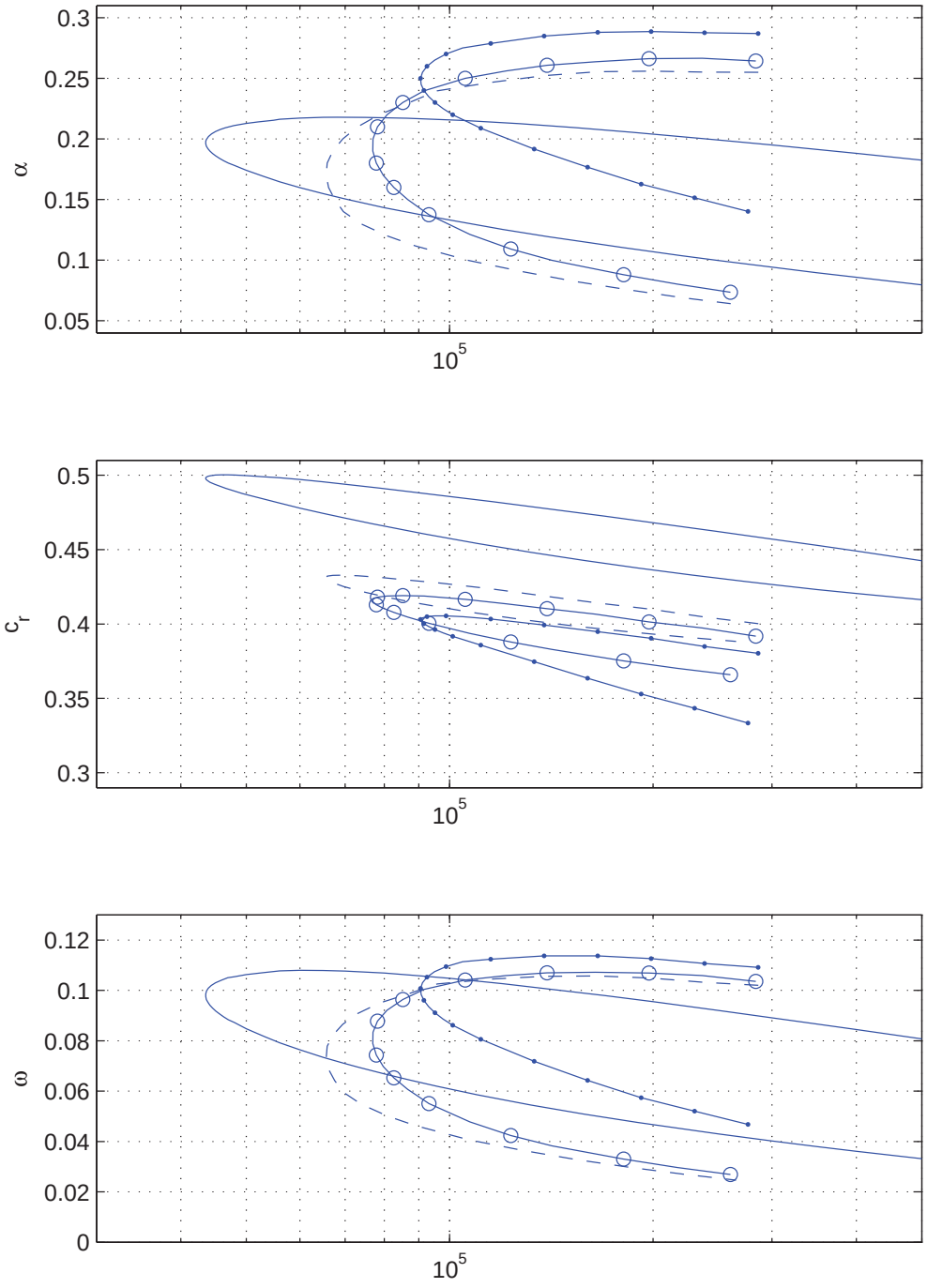

Figure 3.23: Neutral curves for Mode 0 ($\zeta_{\max} = 25$, solid), Mode 1b ($\zeta_{\max} = 30$, dot-marked) and Mode 2b (dashed for $\zeta_{\max} = 25$, circle-marked for $\zeta_{\max} = 30$), plotted as a function of wavenumber α *(top)*, eigenvalue c_{r} *(middle)*, and temporal frequency $\omega = \alpha c_r$ *(bottom)*.

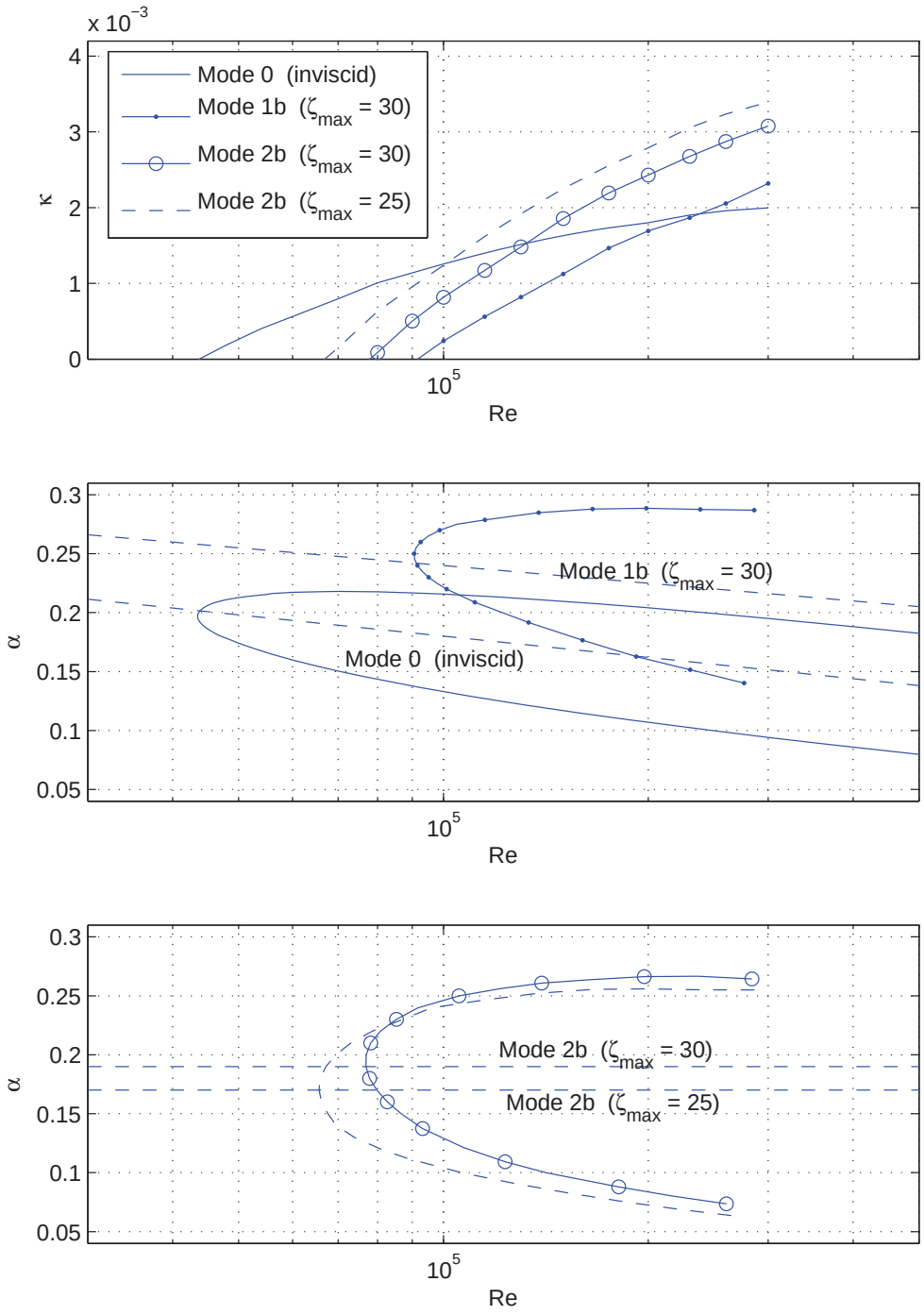

Figure 3.24: *Top:* Growth rates $\kappa \equiv \kappa_j(Re)$ for Mode 0, Mode 1b ($\beta = \beta_c$, $\zeta_{\max} = 30$) and Mode 2b ($\beta = \beta_c$, $\zeta_{\max} = 25, 30$) at the streamwise wavenumbers $\alpha \equiv \alpha(Re)$ indicated by the dashed lines *(middle and bottom* with the corresponding neutral curves indicated for comparison).

Since the viscous modes are highly sensitive to the direction (α, β) of propagation, it is natural to ask how β affects their physical structures. For $\beta \neq 0$ one observes a slight interlacing of the spanwise vortices (compare, for example, the left- and right-hand panels of Figure 3.17). A more striking spanwise effect is evident in Figure 3.15 between modes 1a, 1b and 1c (left-hand panels) and between 2a, 2b and 2c (right-hand panels). As β becomes more negative, the innermost blending-layer vortex becomes more vigorous relative to adjacent vortices; conversely, as β becomes more positive, the inner vortex weakens and the dominant eigenmode activity shifts away from the corner line. (We have confirmed this trend over a wide range of β values.) In other words, the b-type modes ($\beta < 0$) are more strongly influenced by the inner corner region than their c-type counterparts ($\beta > 0$), and more closely resemble the inviscid mode in structure. This appears to explain the instability of the b-type viscous modes relative to the c modes. It also lends support to the above conjecture that the viscous stability limit coincides with that of the inviscid mode.

A final piece of evidence is provided by the eigenmode growth rates in Figure 3.24, which plots instability growth rates for Modes 0, 1b and 2b. For the given (near-optimal) parameter values, the inviscid mode is found to be dominant for $Re \lesssim 10^5$, whereas Mode 2b dominates at higher Reynolds numbers. We therefore hypothesize that the instability mechanism will in practice be a combination of inviscid and viscous effects.

3.7 Summary

This chapter reports on four different numerical methods for the solution of an elliptic eigenvalue equation. Methods 1, 2 and 3, detailed in §§3.3–3.5, focussed exclusively on the inviscid mode of instability (governed by the Rayleigh equation, with Re formally infinite), whereas Method 4 in §3.6 examined all modes simultaneously at finite Re values. Each method succeeded in identifying a (unique) inviscid mode. Method 4 established that this mode is indeed dominant and is characterised by a critical Reynolds number of $Re_c = 44K$, ie approximately half that of 2D Blasius flow. Using Method 4, we have also amassed a wealth of numerical data on the viscous modes, the results of which suggest that both inviscid and viscous modes play a role in destabilizing the laminar flow.

Some further remarks are in order regarding Methods 1–3 (which effectively constituted pilot studies for the full analysis of Method 4). Although Methods 1–3 each yielded tentative identification of the inviscid mode, we were unable in each instance to demonstrate satisfactory numerical convergence within the limits of available

computing power. This came as a considerable disappointment to us, since we had expected efficiency dividends from these pilot studies. In retrospect, our inviscid-mode focus proved counter-productive. Method 1 exploited matrix sparsity, thereby permitting $N \times N$ grid discretizations as dense as $N = 200$; however, its utility was effectively limited to finite-difference methods. (The singular nature of the Rayleigh equation may also have contributed to this poor numerical performance.) In contrast, Method 2 provided spectral accuracy in the spatial domain, but offered little scope for efficiency gains beyond those of the standard QZ eigensolver. Method 3 provided improved spatial resolution over Method 2; its results were promising but still inadequate. Nevertheless, this hard-won experience led directly to the successful Method 4. Method 4 also owes a great deal to Parker and Balachandar (1999), although it is more efficient than their numerical method by an order of magnitude.

Although our findings are similar to those of Parker and Balachandar (1999), they differ in two major respects. Firstly, we find that the flow is inviscidly unstable, whereas Parker and Balachandar (1999) find that the inviscid mode is active only at $Re \gtrsim 500K$ (versus $Re \gtrsim 86K$ for the viscous modes). Secondly, while our viscous data agrees qualitatively with theirs, we suggest that our data is more comprehensive and yields a lower stability limit for the viscous modes. Similar remarks may be made regarding the recent work of Galionis and Hall (2005), who reported a critical Reynolds number of $100K < Re_c < 150K$ for the inviscid mode.

Chapter 4

The laminar flow external to a corner

4.1 Introduction

In this chapter we consider the laminar flow external to a streamwise square corner. It is qualitatively similar to the internal corner flow of Chapter 2 except that the cross-sectional domain is three-quarter infinite rather than one-quarter infinite. To the best of our knowledge, this particular laminar flow has not been the subject of any previous theoretical or experimental studies, even though it is readily amenable to the analytic and numerical tools discussed in Chapter 2. Instead, we compare our results with published experimental data on low-speed turbulent corner flows.

4.2 Analysis

The external square corner is formed by the intersection of two quarter-infinite walls as follows:

$$\text{Horizontal wall:} \qquad y = 0, \quad z \geq 0, \tag{4.1a}$$

$$\text{Vertical wall:} \qquad z = 0, \quad y \leq 0. \tag{4.1b}$$

Thus, the flow occupies the three-quarter infinite domain $\mathcal{D}$ defined by

$$\mathcal{D} = \{(y,z) : y,z \in \mathbf{R};\ \text{but if } z > 0,\ \text{then } y \geq 0\}, \tag{4.2}$$

as illustrated in Figure 4.1a. The corner line is coincident with the x-axis and parallel to the primary or streamwise flow U, which has unit free-stream velocity $U = 1$. As in Chapter 2, we assume symmetry of the flow with respect to the corner

bisector:

$$U(y,z) = U(-z,-y) \qquad \text{and} \qquad V(y,z) = -W(-z,-y), \tag{4.3}$$

and in particular that

$$W = -V \quad \text{along the bisector} \quad z = -y \quad \text{for} \quad y > 0. \tag{4.4}$$

Since we anticipate Blasius-type wall boundary layers of non-dimensional thickness $O(Re^{-\frac{1}{2}})$, we adopt without modification the similarity variables of Chapter 2, ie

$$\eta = \frac{Re^{\frac{1}{2}}y}{\sqrt{2x}} \qquad \text{and} \qquad \zeta = \frac{Re^{\frac{1}{2}}z}{\sqrt{2x}}, \tag{4.5}$$

on the understanding that η and ζ are no longer restricted to non-negative values. Our working domain $\widetilde{\mathcal{D}}$ constitutes the upper half-region, ie

$$\widetilde{\mathcal{D}} = \{(\eta,\zeta) : \ \eta \geq 0, \, \zeta \geq -\eta \}, \tag{4.6}$$

which we truncate for computational purposes to the trapezoidal sub-domain

$$\widetilde{\mathcal{D}} = \{(\eta,\zeta) : \ 0 \leq \eta \leq \zeta_{\max}, \ -\eta \leq \zeta \leq \zeta_{\max} \}, \tag{4.7}$$

as illustrated in Figure 4.1b.

The external-corner flow is subject to the same governing equations and physical boundary conditions as listed in §2.2 for the internal corner. The asymptotic analysis of §2.3.1 also carries over save for a reversal of the crossflow W, as we now demonstrate. Equation (2.23) shows that to leading order, the blending boundary layer comprises a Blasius profile (U_0, V_0) with superimposed crossflow. Consequently, on exiting the blending layer one obtains

$$V(\eta,\zeta) = \beta + o(1) \qquad \text{for} \qquad \eta,\zeta \gg 1, \tag{4.8}$$

where $\beta = 1.2168$ is the Blasius constant. The inviscid outer-region flow takes the form

$$(U,\Omega,\theta)_{\text{outer}} = (1,0,0) + \text{exp. small terms}, \tag{4.9a}$$

$$(W - \mathrm{i}V)_{\text{outer}} = \sum_{n=0}^{\infty} c_n(\zeta + \mathrm{i}\eta)^{-n}, \tag{4.9b}$$

where the complex coefficients $\{c_n\}$ are independent of the spatial coordinates. Comparison of (4.9) with (4.8) yields

$$\mathrm{Im}[c_0] = -\mathrm{i}\beta. \tag{4.10}$$

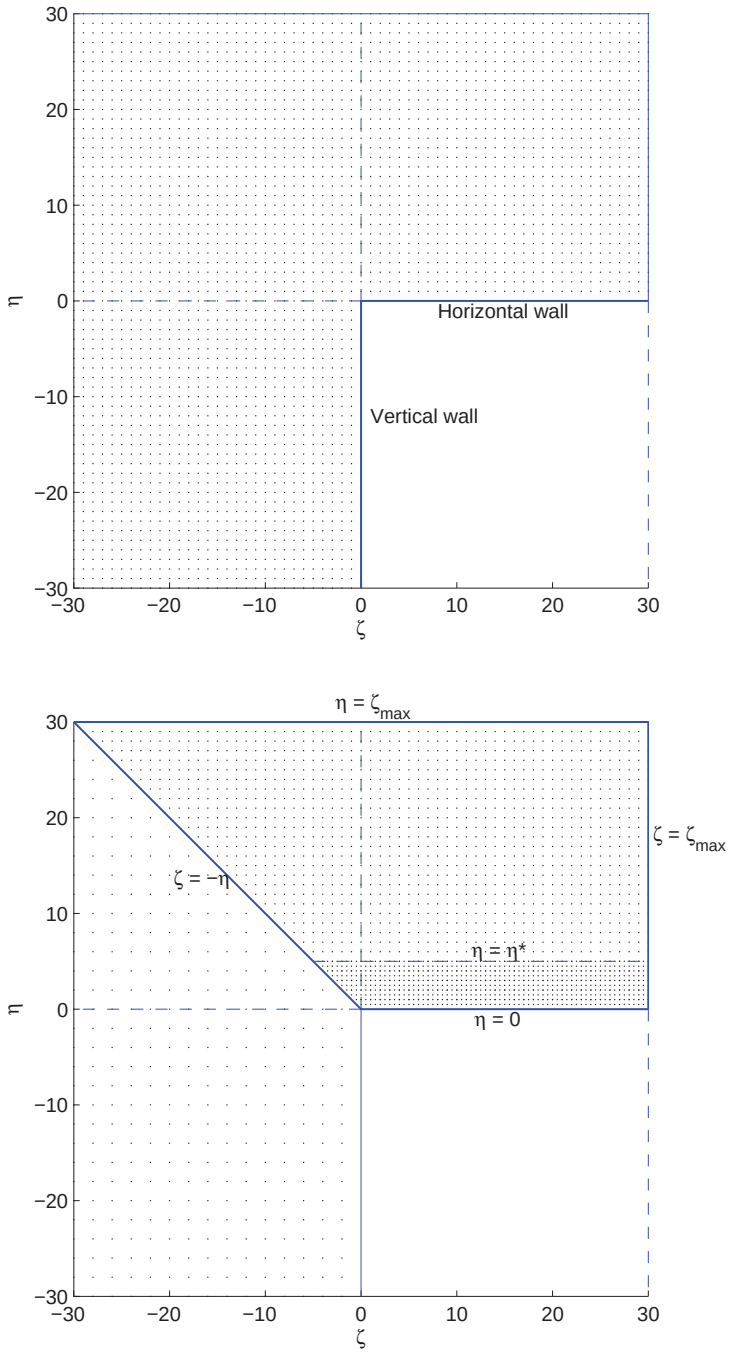

Figure 4.1: *Upper figure:* Cross-sectional flow domain $\mathcal{D}$ for the laminar flow external to a corner. The corner is formed by two quarter-infinite walls located respectively at $\eta = 0$ (for $\zeta > 0$) and $\zeta = 0$ (for $\eta < 0$). The streamwise velocity U is directed into the page. *Lower figure:* The trapezoidal computational domain $\widetilde{\mathcal{D}}$ obtained by truncating $\mathcal{D}$ to a spanwise size $\zeta_{\max} = 30$ while assuming symmetry of the flow with respect to the corner bisector $\zeta = -\eta$. The blending boundary layer is approximated by the highlighted sub-domain $0 < \eta < \eta^*$ where $\eta^* \approx 5$.

Next, comparison of (4.9) and (4.10) with the bisector-symmetry condition (4.4) yields

$$\mathrm{Re}[c_0] \;=\; -\beta, \qquad c_0 \;=\; -(1{+}\mathrm{i})\beta, \tag{4.11}$$

and

$$(V, W, \phi, \psi)_{\mathrm{outer}} \;=\; (\beta,\, -\beta,\, \eta{-}\beta,\, \zeta{+}\beta) \;+\; O(\rho^{-1}), \tag{4.12}$$

where ρ denotes distance from the corner line, ie

$$\rho^2 \;=\; \eta^2 + \zeta^2. \tag{4.13}$$

This result scales the leading-order crossflow component W_0, which takes the form

$$W_0(\eta) \;=\; -\beta g(\eta), \tag{4.14}$$

where the crossflow shape function g is defined in §2.3.1.2. This component constitutes an outflow in the lower half of the blending layer (ie $W_0(\eta) > 0$ for $\eta \lesssim 2$) and an inflow elsewhere ($W_0(\eta) < 0$ for $\eta \gtrsim 2$).

4.3 Numerical method

Our numerical method for solving the governing equations follows that of §2.3.6 for the internal corner. Numerical convergence was found to be somewhat faster than for the internal-corner case, requiring approximately one hundred thousand iterations of the solution algorithm. However, just as for the internal corner, strict domain convergence was precluded by our use of leading-order far-field boundary conditions, ie

$$(U, V, W) \;=\; (U_0, V_0, W_0) \qquad \text{at} \qquad \eta = \zeta_{\max} \quad \text{and} \quad \zeta = \zeta_{\max}. \tag{4.15}$$

The numerical results presented in §4.4 were derived using grid-steps of $h_1 = 0.05$ and $h_2 = 0.25$ in the boundary layer and outer regions respectively. The computational domain $\widetilde{\mathcal{D}}$ was of size $\zeta_{\max} = 58$, the maximum permitted by the restriction (2.75) on numerical stability of the solution algorithm[1].

4.4 Results

Our results for the laminar flow external to a corner are shown in Figures 4.2 to 4.6. Figure 4.2 focusses on the inner corner region, plotting the streamwise velocity U and secondary velocity (V, W) out to a distance of $|\zeta| = 6$ from the corner line.

[1]The value $\zeta_{\max} = 60$ used for the internal corner proved non-viable for external corner.

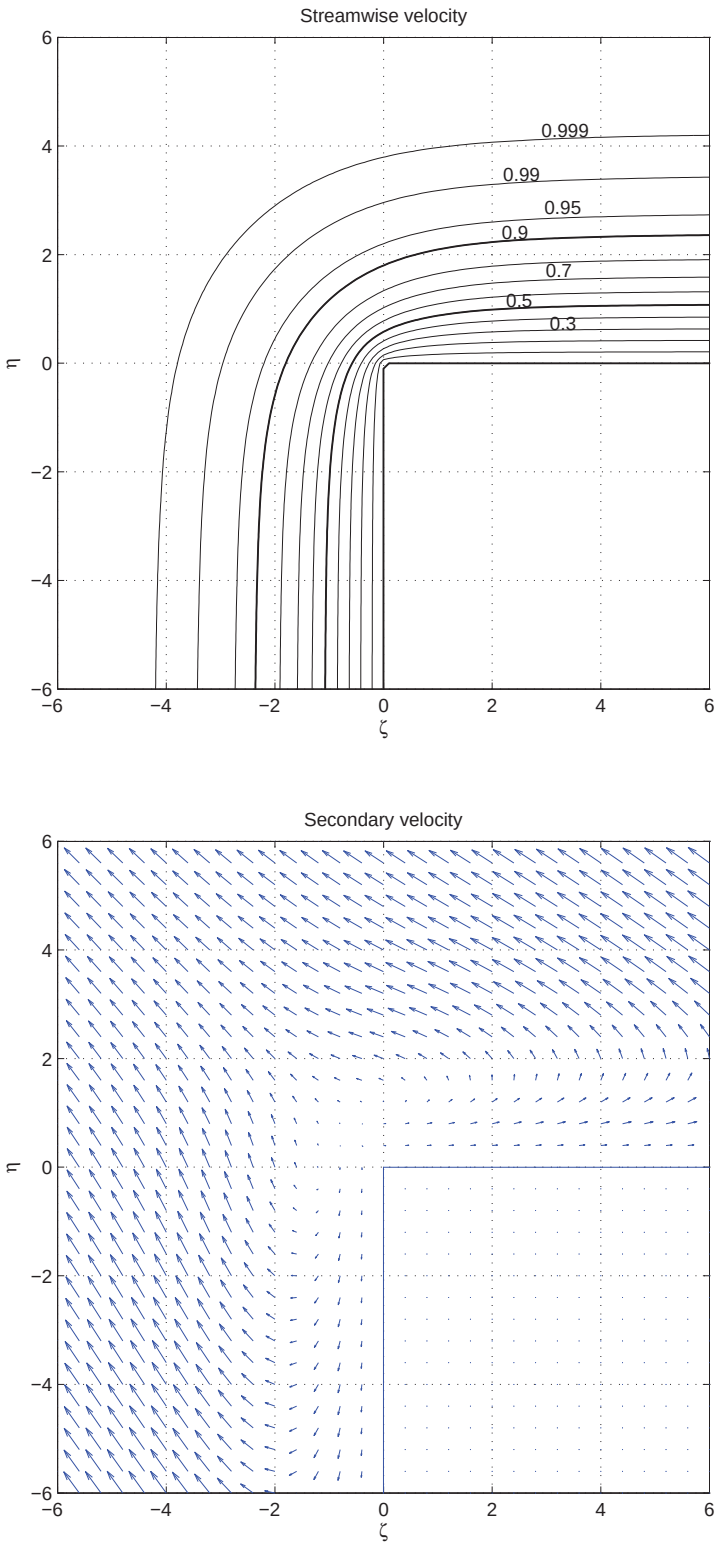

Figure 4.2: Streamwise velocity U *(upper figure)* and secondary velocity (V, W) *(lower figure)*, plotted for $\{(\eta, \zeta) : -6 \leq \eta, \zeta \leq 6\}$.

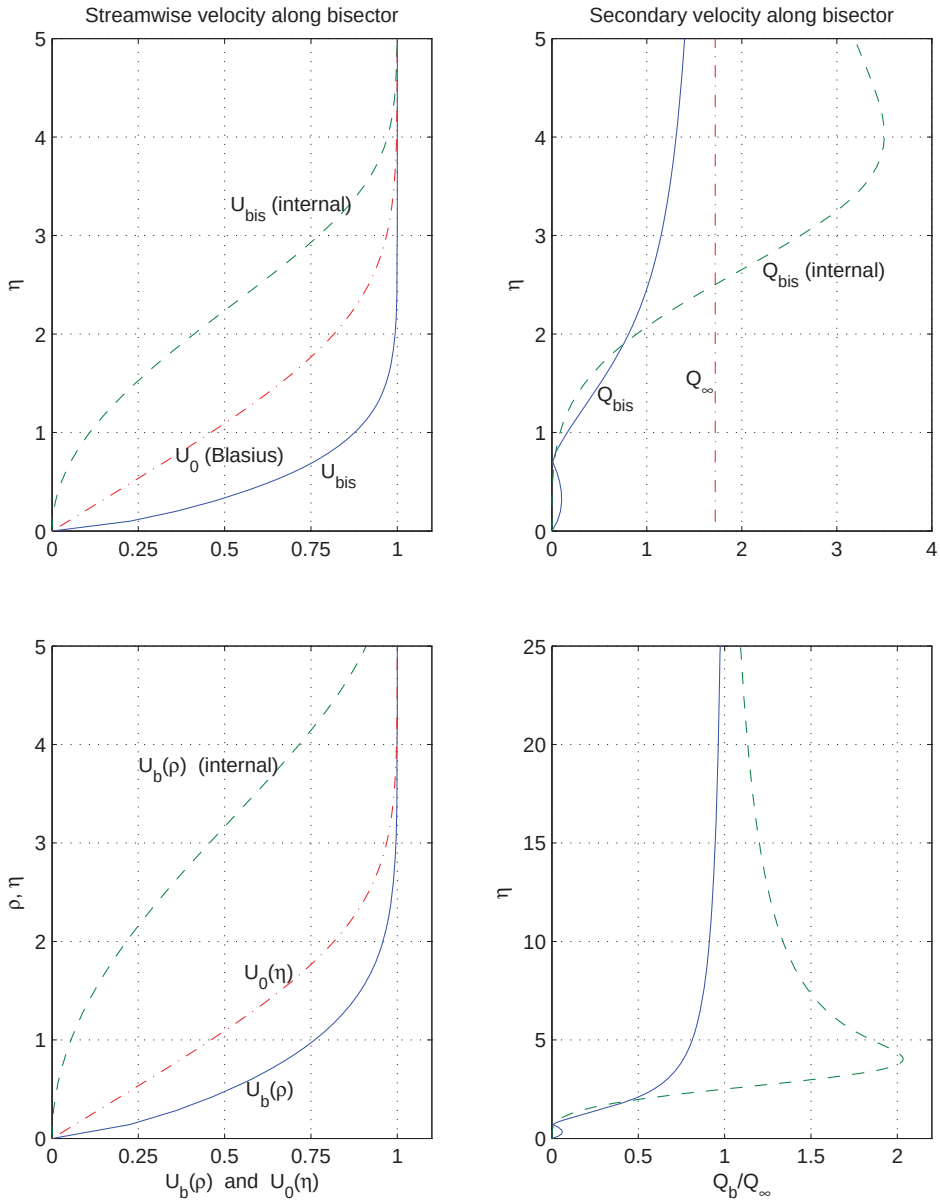

Figure 4.3: Bisector velocity profiles for the external corner *(solid curves)* and internal corner *(dashed curves)* as follows. *Upper left:* Streamwise velocity $U_{\rm bis}(\eta)$; the Blasius profile $U_0(\eta)$ *(dot-dashed)* is shown for comparison. *Upper right:* Magnitude $Q_{\rm bis}$ of the secondary velocity. *Lower left:* Rescaled streamwise velocity $U_{\rm bis}(\rho)$ plotted as a function of distance $\rho \equiv \sqrt{2}\eta$ from the corner line. *Lower right:* Rescaled secondary velocity $r(\eta) \equiv Q_{\rm bis}/Q_\infty$ with $Q_\infty = \sqrt{2}\beta \approx 1.721$, plotted for $0 \le \eta \le 25$.

Figure 4.3 plots the bisector profiles $U_{\rm bis}(\eta)$ and $Q_{\rm bis}(\eta)$ of the streamwise velocity U and secondary velocity $Q = \sqrt{V^2 + W^2}$ respectively. Figures 4.4 and 4.5 plot U and Q out to $|\zeta| = 15$ in order to highlight the algebraic spanwise development of the blending boundary layer. Finally, Figure 4.6 plots Q out to $|\zeta| = 40$ to illustrate the difficulty of accurately capturing the $O(\rho^{-1})$ outer-region variation of the secondary flow (note that the $Q = 1.7$ and $Q = 1.75$ contours extend almost to the computational far-field boundary $max\{\eta, \zeta\} = \zeta_{\rm max}$).

In some respects, the external-corner flow is qualitatively identical to the internal flow discussed at length in Chapter 2, especially with respect to their respective asymptotic properties. Both flows exhibit slow algebraic variation of the secondary flow in the blending layer and outer region, coupled with fast $O(\zeta_{\rm max}^{-2})$ algebraic variation of (U, V) within the blending layer. In the far-field limit $\zeta \to \infty$, both flows feature a reversed profile for the crossflow $W_0(\eta)$; this is evident in Figures 4.4–4.6 in the form of strongly inflectional profiles for the boundary-layer secondary velocity $Q_0(\eta; \zeta)$ for any given $\zeta > 0$. Both flows exhibit very low secondary velocities within the inner core region, with $Q(\rho)/Q_\infty \lesssim 0.1$ for $\rho \lesssim 1.5$ for the external corner. Unlike the internal case, however, the external secondary flow possesses a stagnation point (see Figures 4.2b and 4.3):

$$V_{\rm bis}(\eta) < 0 \quad \text{for} \quad 0 < \eta \lesssim 0.72 \qquad \text{and} \qquad V_{\rm bis}(\eta) > 0 \quad \text{for} \quad \eta > 0.72. \tag{4.16}$$

The surrounding secondary flow traces out a heart-shaped trajectory as it is deflected around the core region and back towards the corner bisector.

In other respects, the external-corner flow represents the inverse of the internal corner. Whereas for the internal flow the bisector secondary velocity $Q_{\rm bis}$ strongly overshoots its limiting value Q_∞, its external counterpart undershoots its limit ($Q_{\rm bis} < Q_\infty$). Whereas $Q_{\rm int}$ attains its global maximum on the bisector (namely $Q_{\rm max} = 2.1\, Q_\infty$ at $\eta = 4.0$), $Q_{\rm ext}$ attains its (relatively weak) maximum at a location far from the corner line:

$$Q_{\rm max} \approx 1.79 \equiv 1.04\, Q_\infty \qquad \text{at} \qquad (\eta, \zeta) \approx (4.6,\, 9.6). \tag{4.17}$$

The most important qualitative difference between the two flows relates to streamwise velocity. In a nutshell, $U_{\rm int}$ is strongly inflectional whereas $U_{\rm ext}$ is monotonic. Thus, the local effect of the square corner is to *expand* the *internal* boundary layer and *constrict* the *external* boundary layer. This effect, though intuitively predictable, appears to be substantially more pronounced one would anticipate on purely geometric grounds (see, for example, the lower-left panel of Figure 4.3, where we plot $Q_{\rm int}$ and $Q_{\rm ext}$ as functions of distance ρ from the corner line). This in turn indicates that the core-region flow in both configurations is strongly nonlinear.

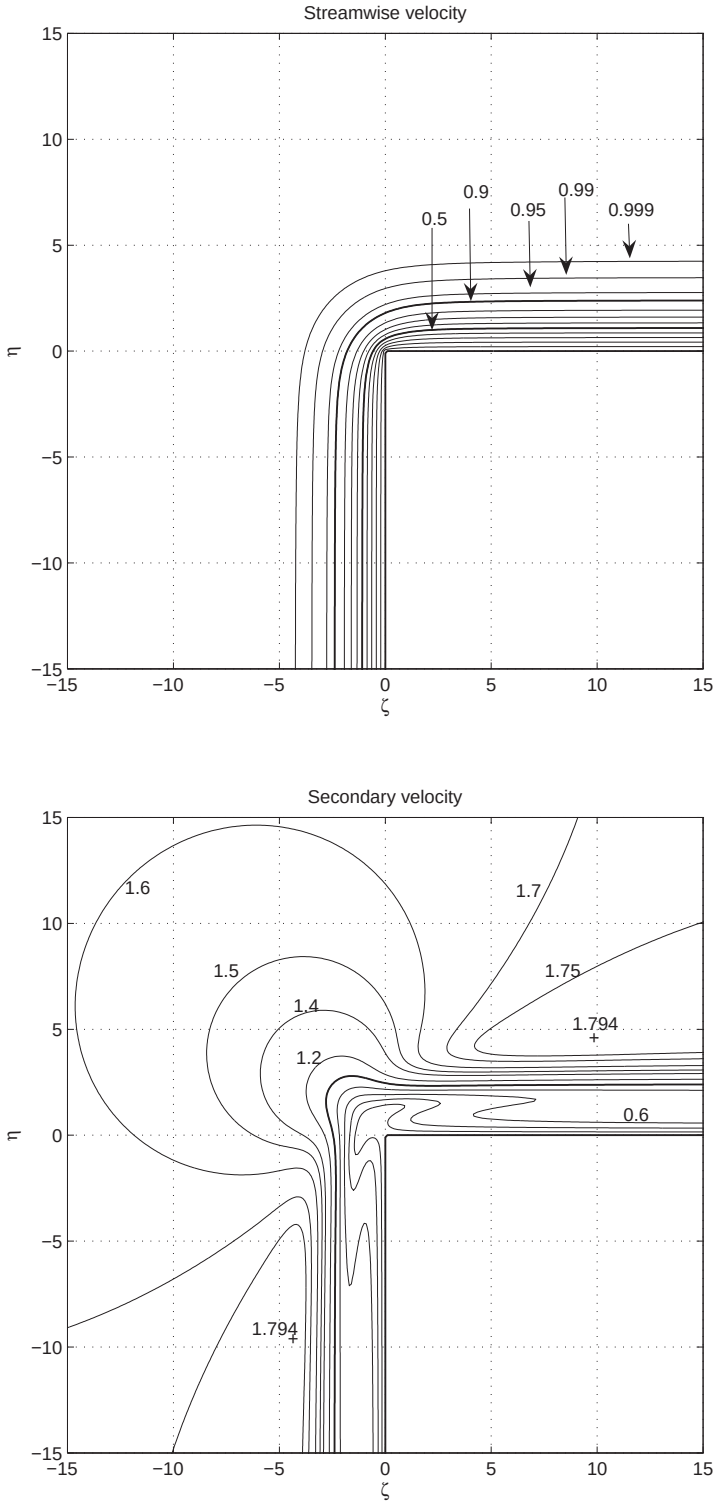

Figure 4.4: Streamwise velocity U and magnitude $Q = \sqrt{V^2 + W^2}$ of secondary velocity, plotted for $\{(\eta, \zeta) : -15 \leq \eta, \zeta \leq 15\}$ with contour spacing $\Delta U = 0.1$ and $\Delta Q = 0.2$ (except where indicated otherwise). The contours corresponding to $U = 0.5$, $U = 0.9$ and $Q = 1$ are highlighted.

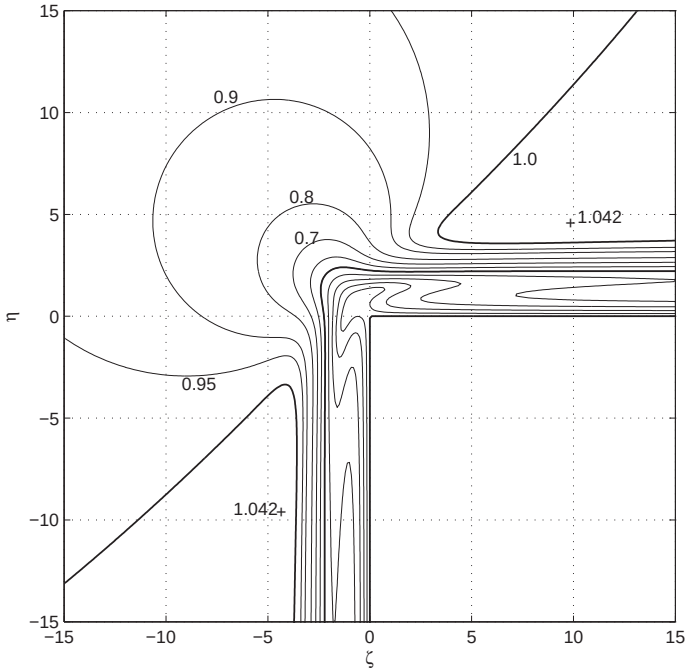

Figure 4.5: Rescaled secondary velocity $r = Q/Q_\infty$ for $\{(\eta, \zeta) : -15 \leq \eta, \zeta \leq 15\}$ with contour spacing $\Delta r = 0.1$ (augmented by the $r = 0.95$ contour). The highlighted contours correspond to $r = 0.5$ and $r = 1$.

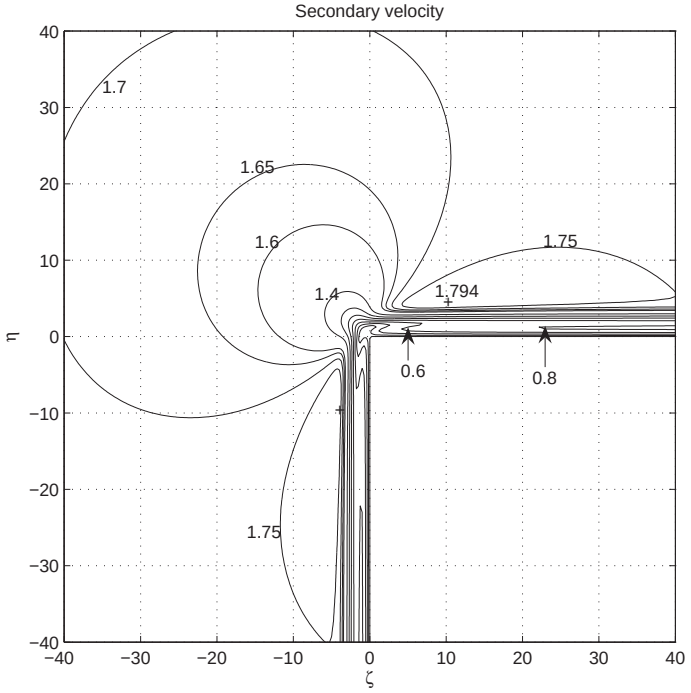

Figure 4.6: Secondary velocity Q for $\{(\eta, \zeta) : -40 \leq \eta, \zeta \leq 40\}$.

Furthermore, we find marked differences between the laminar corner flow computed here and the experimentally measured configurations of turbulent corner flow. Recall from §1.3.5 that Moinuddin *et al.* (2001, 2004) have reported a 'bulging' of the corner-line boundary layer in the low-speed turbulent regime. The origin of this bulging effect was initially unclear; since, however, it is entirely absent from the laminar flow, we concur with their conclusion that it constitutes a strictly turbulent phenomenon. This hypothesis is also consistent with the observation that the turbulent corner boundary layer is several times thicker than its laminar counterpart depicted in Figures 4.2 to 4.4.

Chapter 5

Corner flows: Conclusions and recommendations

5.1 Conclusions

The corner-flow research plan outlined in §1.3.8 listed the following four objectives:

1. To conduct a thorough study of zero pressure gradient (ZPG) laminar flow internal to a square corner.

2. To pioneer the study of laminar flows external to a corner.

3. To conduct a systematic analysis of oblique and/or pressure-driven corner flows.

4. To compare a variety of numerical methods applicable to 3D laminar flows and eigenmode instabilities.

The first of these objectives has largely been fulfilled; our findings on this front were detailed in Chapters 2 and 3, and are summarized in §§5.1.1 and 5.1.2 below. The second objective was partially realised in Chapter 4, whose findings are summarized in §5.1.3 below. (An eigenmode stability analysis has also been attempted for this external flow; publishable data, however, has proved elusive at the time of writing.) Little progress has been made on the third objective, owing largely to lengthy lead times on the first two objectives. However, some progress has been registered on the final objective, notably in Chapter 3 where we compard several eigensolvers for elliptic problems on unbounded domains.

5.1.1 Laminar flow internal to a square corner

In Chapter 2 we presented a detailed analysis of Blasius-type (ZPG) laminar flow in a streamwise corner. Even though this problem has previously been tackled by a number of authors over a period of several decades, we believe our numerical results make a useful contribution to the field of laminar corner flows. Throughout, we have highlighted the difficulty of accurately representing the algebraic variation of the flow as a function of distance ζ or ρ from the corner line. In particular, we have shown that (a) results published prior to 1971 were invariably either incorrect or incomplete; (b) only Rubin and Grossman (1971) employed a completely rigorous process of asymptotic matching (albeit lacking a rational procedure for determining the first-order constant κ); and (c) all post-1971 authors (ourselves included) employed reduced versions of the Rubin and Grossman (1971) analysis.

We find good qualitative agreement between all post-1970 results, including our own. We estimate that our data for the streamwise velocity $U(\eta, \zeta) \equiv U_0(\eta)+O(\zeta^{-2})$ is accurate to three figures — a satisfactory level of accuracy for the ensuing stability analysis of Chapter 3. However, we also find significant differences between published numerical data for the secondary velocity (V, W), which decays at the slow asymptotic rate of $O(\zeta^{-1},\, \rho^{-1})$. Amongst published data, the least accurate results appear to be those of Ghia (1975). This lack of accuracy may be attributable to the author's novel numerical method (ie domain mapping rather than domain truncation); on the other hand, it may merely indicate incomplete numerical convergence, and Ghia's method may in fact be accurate and highly efficient.

Our literature review also extends to a survey of numerical methods. Our own method, involving finite-differencing over a large but finite domain, was expected to deliver reasonable accuracy at modest cost. In reality, however, it presented us with three simultaneous difficulties: weak domain convergence; slow numerical convergence; and strict limits on the stability of the iterative solution algorithm. We ameliorated the latter two problems using a novel domain decomposition. Although we were unable to achieve rigorous domain convergence, we believe that our numerical data accurately describes all salient features of the laminar flow. For future work on corner flows, however, we recommend the exclusive use of spectral or pseudospectral numerical methods, following the examples of Parker and Balachandar (1999) and Galionis and Hall (2005).

5.1.2 Stability of laminar flow internal to a corner

In Chapter 3 we presented a two-part study of the hydrodynamic stability of ZPG laminar corner flow to eigenmode instabilities. The first part of our study, comprising

§§3.3 to 3.5, is restricted to eigenmodes of inviscid character, and does not yield any estimates of critical Reynolds number Re_c. The second part, comprising §3.6, encompasses both viscous and inviscid corner modes at finite Reynolds number. The inviscid analysis was intended as a pilot study on efficiency grounds (since it requires only a single working flow variable, compared with up to four flow variables for the viscous analysis).

The 'inviscid' method yielded inconclusive results, notwithstanding the expenditure of large quantities of human and computer time. Three numerical methods were attempted: finite differencing coupled with the iterative eigensolver of Otto and Denier (1999); pseudospectral discretization with the QZ eigensolver, following Balachandar and Malik (1995); and an improved pseudospectral/QZ eigensolver. Although we did find evidence of the inviscid corner mode reported by Balachandar and Malik (1995), we were unable to achieve satisfactory numerical convergence of the corresponding eigenvalue (even when attempting to duplicate the published numerical method and parameter values).

Our 'viscous' method follows Parker and Balachandar (1999) by combining pseudospectral discretization with an Arnoldi eigensolver; our novel coordinate-mapping technique, however, provides an additional efficiency gain of one order of magnitude. We have thereby confirmed the existence of a (unique) inviscid corner mode and of a broad spectrum of viscous modes of Tollmien–Schlichting type. We report that the leading mode of instability is indeed of inviscid type (as hypothesized by Zamir (1981)), with a stability threshold of $Re_c = 44\ 000$. This result is in striking disagreement with those of both Parker and Balachandar (1999) and Galionis and Hall (2005), who find the leading mode to be of viscous type ($Re_c \approx 10^5$). We suggest that this discrepancy is attributable to weaknesses in their respective numerical methods (in particular, the treatment of the crucial pressure boundary conditions). Furthermore, we suggest that their respective 'viscous' analyses fall short of identifying the most unstable spanwise wavenumber, leading to slightly elevated estimates of the viscous stability threshold Re_{cv}. Although we have declined to offer a precise estimate of Re_{cv}, we show that it is significantly lower than the 2D limit $Re_c = 91\ 000$, and may in fact coincide with the 'inviscid' threshold of $Re_c = 44\ 000$.

5.1.3 Laminar flow external to a square corner

In Chapter 4 we presented original research on the laminar flow external to a streamwise square corner. We report that the internal and external corner flows are qualitatively similar in some respects and very different in other respects. In particular,

both flows exhibit algebraic characteristics in the blending boundary layer, coupled with strongly nonlinear boundary-layer interaction within the inner corner region. On the other hand, the streamwise velocity profile is uniformly non-inflectional in the external case, whereas in the internal case the bisector profile $U_{\rm bis}(\eta,\eta)$ is strongly inflectional; the latter, we suspect, is responsible for the inviscid-type instability mode identified in Chapter 3. Similarly, we find that the bisector secondary velocity $Q_{\rm bis}$ is monotonic in the external case but strongly non-monotonic in the internal case. Some of the above flow characteristics might have been anticipated intuitively on geometric grounds; nevertheless, we argue that they are in fact quite striking, and reflect the strongly nonlinear and three-dimensional nature of the interaction between the two wall boundary layers of each flow. In the external case, this interaction gives rise to a well-defined secondary-flow vortex in the inner corner region. We argue that this vortex is a strictly laminar phenomenon, bearing only a superficial resemblance to the turbulent external boundary-layer vortex structures observed by Moinuddin *et al.* (2001, 2004).

Since this laminar flow is non-inflectional, we conjecture that it is more stable than the corresponding flow internal to a corner. We have attempted to test this hypothesis by adapting the stability analysis of §3.6 to the present case of external flow. Unfortunately, at the time of writing we have been unable to demonstrate numerical convergence or to reach any conclusions of a qualitative nature. The difficulty would, however, appear to be connected to our reformulation of the generic instability equations (3.5) in cylindrical coordinates (ρ,θ), and our subsequent discretization of the (ρ,θ) domain using a Chebyshev pseudospectral scheme. The poor performance of this scheme may be due to interpolation of the laminar-flow data computed using the low-order finite-difference scheme of §4.3. It would clearly be desirable, therefore, to re-compute the laminar flow using a spectral scheme in cylindrical coordinates. This project would be well worthwhile since, if successful, it could be readily adapted to the case of arbitrary corner angle $0 < \Phi < 2\pi$.

5.2 Recommendations for further research

We close this section with three recommendations for future work on laminar corner flows.

Our first recommendation is to round off the above study of Blasius-type corner flow. In particular, we recommend pseudospectral implementations of the methods of Rubin and Grossman (1971), Ghia (1975) and Dhanak and Duck (1997), with a view to identifying the most accurate and efficient method for computing the

laminar flow. The study should also consider whether these methods are suitable for more general corner flows, as discussed in Recommendations 2 and 3 below[1].

Secondly, we recommend a thorough numerical study of Falkner–Skan corner flows, for which analytic results are readily available in the literature. In particular, we recommend that stability analyses be performed for laminar corner flows driven by weakly to moderately favourable streamwise pressure gradients, given that the experimental review of Zamir (1981) strongly suggests that this class of laminar corner flows is of the greatest practical significance. For the Falkner–Skan model, this regime corresponds to $0 < n \lesssim 0.1$ (say), where n is defined by (1.26). This study should encompass laminar flows of both Blasius and non-Blasius type, since it remains unclear at this stage which type is more likely to occur in practice. The study might also seek a universal criterion for the stability of laminar corner flows. For example, it may be possible to show that the stability of any laminar corner flow can be reliably estimated from the local boundary-layer Reynolds number $Re_\delta(x)$ at any given streamwise location x, irrespective of the precise experimental conditions. This would be a valuable finding, since $Re_\delta(x)$ can be estimated *a priori* for a given streamwise velocity $U_\infty(x)$ or pressure $P_\infty(x)$.

Thirdly, we recommend that the study of pressure-driven laminar corner flows be extended from the Falkner–Skan model to more realistic models, such that the incident streamwise flow $U_\infty(x)$ is smooth and bounded throughout any finite domain, including across the leading edge at $x = 0$. We realize that this represents an ambitious undertaking, for at least two reasons. Firstly, it implies a partial breakdown of the property of streamwise similarity encapsulated in the Falkner–Skan model. Secondly, a streamwise marching algorithm may prove non-viable, given that Duck *et al.* (1999) and Duck and Owen (2004) encountered a confounding streamwise eigenmode in non-similar corner flows[2]. It nevertheless appears feasible, at a minimum, to compute accurate flow profiles in the asymptotic far-field limit ($\zeta \to \infty$) and thereby estimate the boundary-layer Reynolds number Re_δ at any streamwise location. Ideally, this data would in turn furnish boundary conditions for a fully three-dimensional analysis of the flow.

Last but not least, we recommend that further wind-tunnel experiments be con-

[1]Note that Ghia's method is not immediately applicable to general Falkner–Skan corner flows, whose secondary velocity is theoretically unbounded in the asymptotic limit $\rho \to \infty$. However, Ghia's mapping technique may still be applicable (and efficient) if implemented in *conjunction* with domain truncation rather than as an alternative to it.

[2]Although this mode appears to be unstable only for Blasius-type flows, its numerical effects are also apparent for non-Blasius flows under unfavourable or weakly favourable streamwise pressure gradients.

ducted on internal and external corner flows in the laminar and transitional regimes. We are well aware of the practical difficulties of producing clean, low-speed laminar flows, and of conducting instrumental measurements within boundary layers of millimetre- to centimetre-scale thickness. Nevertheless, it should at least be feasible to build on the findings of Zamir (1981) for laminar and transitional corner flows under weakly-favourable pressure gradients. At a minimum, it should prove possible to estimate the laminar-stability threshold Re_c as a function of streamwise pressure gradient or local boundary-layer thickness $Re_\delta(x)$. Finally, it should also be possible to determine the qualitative nature of the laminar flow (ie Blasius-type or non-Blasius), either by direct measurement of the velocity vector or by comparing theoretical and experimental values of the viscous skin friction. Such data would not only be of considerable practical value, but would also prove extremely useful as a benchmark for future work on three-dimensional boundary layers.